technische universität
dortmund

Dissertation

Control of Orbital Angular Momentum of Exciton Polariton Condensates

submitted in partial fulfillment of the
requirements for the degree of

Dr. rer. nat.

to the Institute of Physics of the
TU Dortmund University, Germany

by

Bernd Berger

Dortmund, February 2021

Accepted by the Faculty of Physics of the TU Dortmund University, Germany.

Day of the oral examination: 9th April 2021

Examination board:

Jun.-Prof. Dr. Marc Aßmann
Prof. Dr. Mirko Cinchetti
Prof. Dr. Götz S. Uhrig
Dr. Bärbel Siegmann

Contents

Summary

The goal of this work is to investigate the use of exciton polariton vortices for all optical information processing. To achieve this goal, we develop a novel technique based on sorting orbital angular momentum states of light, which allows for detecting and temporally tracing vortices in a light beam. We successfully implement and benchmark this technique and apply it to demonstrate the spontaneous formation of exciton polariton vortices inside all optically excited annular trapping potentials in a GaAs based microcavity. Subsequently we investigate the temporal dynamics of this formation process, which is strongly dependent on excitation power. Our experimental results show the simultaneous and statistically independent formation of vortex modes with topological charges $m = -1$ and $m = +1$. We gain further insight into the temporal dynamics of all arising modes by theoretically modeling our experimental results. Furthermore, in some cases vortices show spin-orbit coupling between their orbital angular momentum and their spin, which corresponds to the circular polarizations σ^+ and σ^-. In the final stage of our experiments, we experimentally verify the theoretical prediction that the topological charge of exciton polariton vortices may be flipped by perturbing them with a pulsed laser. Thereby we demonstrate the potential use of exciton polariton vortices as all-optical information storage.

Zusammenfassung

Das Ziel dieser Arbeit ist die Untersuchung von potenziellen Anwendungen von Vortizes in einem Exziton-Polariton System für die optische Informationsverarbeitung. Um diese Vortizes zu untersuchen, entwickeln wir eine neuartige Spektroskopiemethode, welche auf einer optischen Transformation zur Sortierung von Drehimpulszuständen des Lichts basiert und uns die Detektion und zeitliche Beobachtung von Vortizes in einem Lichtstrahl ermöglicht. Wir implementieren diese Technik und wenden sie erfolgreich an, um die spontane Bildung von Exziton-Polariton-Vortizes innerhalb einer rein optisch erzeugten Ringfalle in einer GaAs basierten Mikrokavität nachzuweisen. Anschließend untersuchen wir die zeitliche Dynamik dieses Bildungsprozesses, welcher sich stark mit der Anregungsleistung ändert. Unsere experimentellen Ergebnisse zeigen die gleichzeitige und statistisch unabhängige Bildung von Vortizes mit den topologischen Ladungen $m = -1$ und $m = +1$. Durch theoretische Modellierung des Exziton-Polariton Systems gewinnen wir tiefergehende Erkenntnisse über die zeitliche Dynamik aller auftretenden Moden. Weiterhin zeigen die untersuchten Vortizes in einigen Fällen eine Spin-Bahn-Kopplung zwischen ihrem Drehimpuls und ihrem Spin, welcher den zirkularen Polarisationen σ^+ und σ^- entspricht. Im letzten Schritt unserer Experimente verifizieren wir die theoretische Vorhersage, dass der Drehsinn von Vortizes durch gezielte optische Manipulation mit zusätzlichen Laserpulsen umgeschaltet werden kann. Damit zeigen wir den potenziellen Nutzen von Exziton-Polariton-Vortizes als rein optische Informationsspeicher auf.

Chapter 1

Introduction

Light has always been used as a tool for communication. One of the Seven Wonders of the Ancient World represents a good example for the historical usage of light: The lighthouse of Alexandria. It was build in the 3rd century BC to mark the port entrance of the nowadays Egyptian city Alexandria. The light emitted by a fire on its top served the purpose to safely guide the ships at night [1]. The technological advance and deepened understanding of the nature of light gained through extensive research enables much more sophisticated ways of communication with light compared to the ancient times. State of the art telecommunication technology relies on light signals guided by glass fibers and allows for data transfer with high speed and bandwidth. However, the devices connected with each other by this communication channel are based on electronic data processing. Thereby the light signals always are converted to electronic currents, which travel per se slower than the speed of light. This limits the speed of data processing and routing of data in networks. To put it the other way around: Devices directly processing light signals might operate faster and allow for higher data rates. Given the increasingly networked world with continuously rising data volumes, the development of such devices is a desirable goal. This thesis represents a small contribution towards developing such devices, which process information all optically.

A potential system enabling all optical information processing consists of exciton polaritons in a planar microcavity. A lot of non-linear phenomena have been studied on this system. To mention only a few: Optical bistability [2], superfluid polariton propagation [3] and polariton condensation [4] have been shown. Based on these phenomena many applications for optical data processing have been demonstrated, for example transistor operation of polaritons [5–7] and polariton spin switches [8]. Also the formation of quantized vortices in exciton polariton condensates has been observed [9]. The subject of this thesis is to study these exciton polariton vortices in further detail. To do so, we pursue a novel approach for the detection of vortices. Since the light emitted by exciton polariton vortices carries orbital angular momentum (OAM), we implement a tailored spectroscopy method based on OAM sorting, which allows the efficient detection of vortices. In a first step we implement this method and benchmark

its use regarding the detection of sample signals carrying OAM. The further road map using this method consists of specifically exciting exciton polariton vortices, investigating the dynamics of their formation process and finally manipulating the vortices. Gaining control over exciton polariton vortices might pave the way towards potential applications in all optical information processing.
In chapter 2 the theoretical basics of excitons, microcavities, exciton polaritons, condensation of exciton polaritons, formation of polariton vortices and OAM are presented. We also sum up the OAM sorting method, which we use in our experiment for detecting vortices. In chapter 3 we describe its practical implementation in detail and sketch the full experimental setup for measuring exciton polariton vortices. The results of the measurements are discussed in chapter 4 and put into the greater context of optical information processing in chapter 5.

Chapter 2

Theoretical basics

Excitons are quasiparticles in semiconductors, which arise when electrons excited into the conduction band form bound states with the remaining holes in the valence band. The excitation of an exciton may be triggered by the absorption of a photon of a light beam. When excitons are strongly coupled to a light field (for example in a microcavity), the energy is exchanged rapidly between excitons and photons so that new eigenmodes in this system arise, the so called exciton polaritons. Exciton polaritons thereby are quasiparticles with mass, showing several non-linear interactions, which include, but are not limited to, exciton polariton condensation [4]. In section 2.1 the fundamentals of exciton polaritons in microcavities and the condensation of exciton polaritons are presented, following Refs. [10, 11]. An advantageous feature of exciton polaritons is their direct optical accessibility, since the polaritons emit photons during decay. The emitted light may be imaged and detected easily using an optical setup. Due to Coulomb interaction, the exciton polaritons interact with each other and all other charged carriers, which renders it possible to shape and control exciton polaritons by optically imprinting potentials with spatially shaped laser beams. In section 2.2 we show the fundamental principle how to shape a light beam by spatially modulating its phase structure.

Given all the features of the polariton system, it is not surprising that many studies of exciton polaritons have been performed. Here, our particular interest goes to exciton polariton vortices [9, 12–17], which we introduce in section 2.3. Exciton polariton vortices are quantized excitations associated with a circular motion of exciton polaritons. We want to specifically excite such vortices in exciton polariton condensates to study their potential applications in all-optical information processing. To achieve this goal, we follow the theoretical concept of Ma et al. [18–20], which suggests vortex formation inside an all optically excited ringlike trap.

Once vortices form inside a ringlike trap, their detection is also a crucial point. Here, we exploit the correspondence of the polaritons inside the microcavity and photons emitted by the microcavity. The phase structure of the exciton polariton vortices inside the microcavity translates into the phase gradient of the light beam emitted by the sample. This light beam thereby carries OAM, as we will discuss in section 2.4.

The OAM is a fundamental degree of freedom of light fields. The availability of an infinite set of orthogonal OAM modes potentially allows one to increase the number of channels for information transfer while having only one light beam. To separate and simultaneously detect these channels of different OAM states, the OAM sorting method was developed by Berkhout et al. [21]. Our basic idea is to utilize this method to detect exciton polariton vortices. The working principle of OAM sorting is explained in section 2.5. In subsection 2.5.1 we also provide a Matlab implementation of a simple beam propagation simulation, which we use to reproduce the OAM sorting process theoretically.

2.1 Exciton polaritons in microcavities

First, this chapter presents the properties of bare excitons in bulk semiconductor material. The optical properties of excitons change when they are confined in quantum wells, which are potential wells formed by thin layers of semiconductor material that allow only few discrete energy states of excitons along the direction of confinement. Such quantum wells may be placed in microcavity structures, which are optical resonators that microscopically confine a light wave while also amplifying its amplitude locally. When the excitons inside the quantum wells strongly interact with the resonant light field mode of a microcavity, the so called exciton polaritons may arise as new eigenmodes of this system. We derive their energy dispersion and discuss their optical properties. Finally, we discuss the condensation of exciton polaritons, which is of high relevance for this thesis, as we use this mechanism to excite exciton polaritons inside the microcavity.

2.1.1 Excitons in semiconductors

The states of electrons in a semiconductor are determined by band structures. For optical processes only the bands nearby the energy gap of the semiconductor are important. Thus, we consider a simplified picture of a low energy valence band and a high energy conduction band, both separated by an energy gap. When an electron in the valence band is excited into the conduction band, a hole remains in the valence band. This hole can be treated as a $+e$ charged quasiparticle, where e is the elemental charge of an electron. Due to Coulomb interaction the electrons in the conduction band and holes in the valence band may form bound states. We call these states excitons. Fig. 2.1 exemplarily illustrates the band structure of a semiconductor near the band gap, including the dispersions of electrons and holes. The corresponding equations are 2.1 and 2.2, in which we assume a parabolic shape for the bands, which is the usual approximation for small wave vectors k [22].

$$E_{\mathrm{C}} = E_{\mathrm{V}}(0) + E_{\mathrm{g}} + \frac{\hbar^2 k^2}{2m_{\mathrm{e}}} \tag{2.1}$$

$$E_{\mathrm{V}} = E_{\mathrm{V}}(0) + \frac{\hbar^2 k^2}{2m_{\mathrm{h}}} \tag{2.2}$$

Here, E_{V} and E_{C} are the energies of valence band and conduction band, E_{g} is the energy gap. The effective masses m_{e} and m_{h} are given by the curvature $-(\partial^2 E/\partial p^2)^{-1}$ with $p = \hbar k$. While the effective mass of an electron is positive, the effective mass of a hole is negative. This results in separate dispersions with opposite curvatures, as Fig. 2.1 illustrates. For materials with zinc blende structure, such as GaAs, the dispersion of holes in the valence band splits into light holes and heavy holes. In bulk material heavy and light holes have the same maximum energy E_{V}, while in quantum wells the light hole dispersion is shifted slightly below the band edge due to strain [23]. Due to spin-obit interaction also split-off holes with a dispersion energetically far below E_{V} form (not shown in Fig. 2.1). In optical processes mainly the heavy holes are involved, since allowed optical transitions involving heavy holes are about three times as probable as those involving light holes [23].

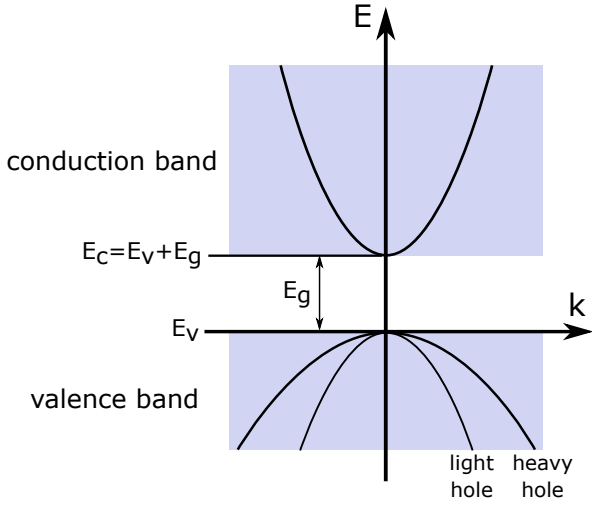

Figure 2.1: Illustration of electron and hole dispersions in a bulk semiconductor, separated by a band gap. Electrons are excited and populate the conduction band. In the valence band positively charged holes remain, when electrons are excited. In a quantum well structure the heavy and light hole dispersions are split and the light hole dispersion is shifted slightly below E_{V} due to strain [23]. Adapted from Ref. [24].

Due to Coulomb attraction a negatively charged electron and positively charged hole may form a transient binding state, which can be treated as a dedicated quasiparticle, the so called exciton. The Coulomb force binding the electron and hole may be

screened, resulting in varying binding energies and physical exciton sizes for materials with different dielectric constants. In materials with a small dielectric constant the Coulomb force is hardly screened and strongly localized excitons with high binding energies may arise, the so called Frenkel excitons. Typically Frenkel excitons occur in organic molecular crystals and exhibit binding energies of 100-300 meV [22, 23]. In contrast to this, in materials with a large dielectric constant such as the inorganic semiconductor gallium arsenide (GaAs), the Coulomb force is screened more significantly. In this case strongly delocalized excitons with typical binding energies on the order of 10 meV arise, the so called Wannier-Mott excitons [25]. Typical lifetimes of Wannier-Mott excitons in bulk GaAs are on the order of nanoseconds [26]. In contrast to the Frenkel excitons, the Wannier-Mott excitons extend over several unit cells of the lattice and may not be bound to individual molecules. In the following we only discuss Wannier-Mott excitons, as the Frenkel excitons may not exist in the GaAs based semiconductor sample we investigate in this thesis.
Since the binding state of a heavy hole and a lighter electron highly resembles the hydrogen atom, the theoretical treatment is very similar and allows one to use the same quantum numbers n,l,m,s. We separate the center of mass motion, which shows the dispersion relation $E = \frac{\hbar^2}{2M}K^2$ with $M = m_\mathrm{e} + m_\mathrm{h}$ and the momentum of the center of mass motion $\hbar K$. The wave vector is $K = k_\mathrm{e} + k_\mathrm{h}$ with $k_\mathrm{e} < 0$ and $k_\mathrm{h} > 0$. We obtain a hydrogen-like structure for the energy levels, which scale with the main quantum number n as follows:

$$E_\mathrm{X}^n = -\frac{m_\mathrm{r}^*}{m_0\epsilon_r^2} \cdot \underbrace{\frac{m_0 e^4}{2(4\pi\epsilon_0\hbar)^2}}_{=:E_\mathrm{Ryd}} \cdot \frac{1}{n^2}, \quad (n \geq 1) \tag{2.3}$$

Hereby m_r^* is the reduced effective mass with $m_\mathrm{r}^{*-1} = m_\mathrm{e}^{*-1} + m_\mathrm{h}^{*-1}$, m_0 is the electron mass and ϵ_r is the dielectric constant. The first factor $(m_\mathrm{r}^*/m_0)\epsilon_r^{-2} \approx 10^{-3}$ accounts for the different masses of the involved particles and the Coulomb screening. The second factor equals the atomic Rydberg energy $E_\mathrm{Ryd} = 13.605693\,\mathrm{eV}$ [27], as known for the hydrogen atom. In bulk GaAs the exciton binding energy amounts to 4.1 meV [23], which is three orders of magnitude lower than the binding energy of the electron in the hydrogen atom. This small binding energy implies that in GaAs excitons may only exist at low temperatures, otherwise they would be thermally dissociated. To illustrate this, we think of a free particle in an ideal gas model [28]. The kinetic energy of such a particle with three degrees of freedom reads as

$$E = \frac{3}{2}k_\mathrm{B}T, \tag{2.4}$$

with the Boltzmann constant $k_\mathrm{B} = 8.617333 \cdot 10^{-5}\,\mathrm{eV/K}$ [29] and the temperature T. By comparing this value to the exciton binding energy we may roughly estimate the maximum temperature at which excitons may exist in bulk GaAs to 32 K.
The energy dispersion of the excitons is illustrated in Fig. 2.2 and reads as follows:

$$E = E_\mathrm{g} + E_\mathrm{X}^n + \frac{\hbar^2}{2M}K^2 \tag{2.5}$$

Above the band gap a continuum of unbound electron hole states, which do not form excitons, exists. Although the excitons exhibit a parabolic dispersion, only the excitons with $K \approx 0$ participate in optical absorption processes, since the wave vector of photons at energies near the energy of the band gap is negligibly small compared to the reciprocal lattice vector [22]. Furthermore the oscillator strength of the optically allowed exciton transitions decreases with n^{-3}, through which typically only the $n = 1$ excitons are observable when additional inhomogenities exist [24]. Taking the selection rules for optical transitions into account, we assume mainly 1s-hh excitons to contribute to the optical processes investigated in this thesis.

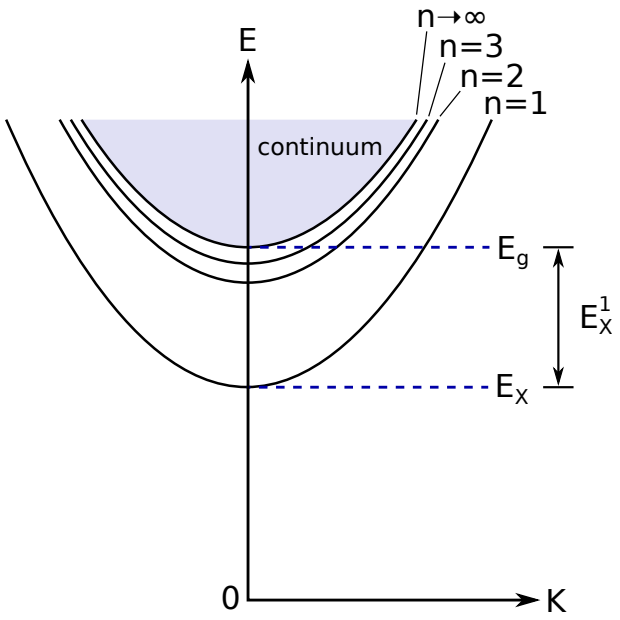

Figure 2.2: Illustration of the exciton dispersion for different main quantum numbers n. The wave vector K refers to the center of mass motion of the bound electron and hole. Adapted from Ref. [24].

As mentioned before, the Wannier-Mott excitons are strongly delocalized. The radius of the excitons can be calculated in analogy to the hydrogen atom according to

$$r_{\mathrm{X}}^{n} = n^2 \frac{m_0}{m_r^*} \epsilon_r a_{\mathrm{B}} \ , \tag{2.6}$$

with the Bohr radius $a_{\mathrm{B}} = 52.917721\,\mathrm{pm}$ of the hydrogen atom [30]. In GaAs the exciton radius amounts to $a_{\mathrm{X}} = r_{\mathrm{X}}^{1} = 14.6\,\mathrm{nm}$ [24], which exceeds the lattice constant of 0.565 nm in GaAs [31] vastly. This demonstrates the strong delocalization of the excitons. Finally, it should be noted that excitons can be considered as bosons with integer spin, even though they are formed by fermionic particles with half-integer spin.

This is a very good approximation as long as the excitons are spatially separated from each other much farther than their radius.

Quantum well excitons

We now consider excitons inside quantum wells. A quantum well consists of a thin semiconductor layer with a thickness comparable to the exciton radius enclosed between other layers of semiconductor material with a larger band gap. This confinement leads to a quantized center of mass movement with only few allowed states perpendicular to the layer plane. When just one such state is possible, the excitons can only move in one plane inside the quantum layer and become two-dimensional quasiparticles. Most strikingly the rotational symmetry is broken and the three dimensional momentum is not a good quantum number any more. As a consequence the momentum only needs to be conserved in the two-dimensional plane when excitons are excited by resonant optical pulses. Excitons inside the quantum well optically couple to light of equal wave vector $k_{||}$ in plane and arbitrary wave vectors $k_{\perp}$ perpendicular to the plane.
The two-dimensional layer structure also modifies the semiconductor band structure and changes the selection rules for optical transitions. Confining the excitons in a two-dimensional planar structure reduces the Coulomb screening, which increases the binding energy and reduces the exciton radius. The oscillator strength simultaneously increases, but effectively the total coupling of photons to the excitons is smaller compared to bulk material because of the minor layer thickness of the quantum wells. The coupling strength between photons and quantum well excitons may be strongly increased by embedding the quantum wells in an optical microcavity, which we discuss in the next section.

2.1.2 Structure and properties of optical microcavities

An optical microcavity is a resonator, which microscopically confines a light field on typical length scales of few hundred nanometers to several micrometers. Various designs based on different materials exist. The design of the sample we investigate in this thesis consists of several spatially extended but very thin semiconductor layers, which are stacked on top of each other. An elementary sketch of the layer structure and the electrical field component of the resonant light field mode is shown in Fig. 2.3. The microcavity consists of two distributed Bragg reflectors (DBRs) enclosing the cavity layer with an optical thickness of $\lambda_C/2$, whereby λ_C is the design wavelength of the microcavity. The quantum wells are embedded in the cavity layer at the antinodes of the locally amplified light field. The DBRs are made up of alternating layers of semiconductor material with different refractive indices, but identical optical thickness of $\lambda_C/4$. When a light beam incides onto the DBR, this periodic alignment induces multiple splitting of the beam into reflected and transmitted parts at all layer boundaries. The resulting partial beams interfere destructively in transmission direction and constructively in the direction of reflection. Hence, the DBR very efficiently reflects light, whereas the reflection coefficient is at the maximum for perpendicularly incident

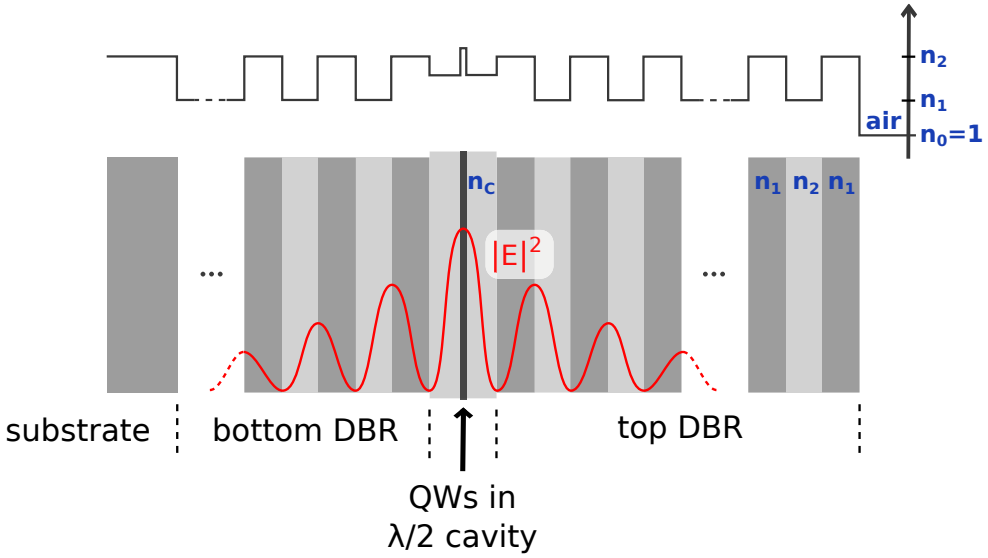

Figure 2.3: Sketch of a microcavity including an exemplary illustration of the electrical field distribution of the confined light field. The layers consist of material with different refractive indices n_1, n_2 and n_c. The quantum wells are positioned by design in the central antinode of the light field confined in the cavity. Adapted from Ref. [10].

light beams with a wavelength of λ_C. However, also light beams with different wavelengths near λ_C or with slightly tilted angles of incidence still are reflected efficiently. The reflectivity spectrum of a DBR thereby exhibits a wide wavelength range with high reflectance, the so called stop band. This stop band also shows up in the reflectivity spectrum of the full microcavity, as exemplarily illustrated in Fig. 2.4. In addition to the stop band resulting from the DBRs, the reflectance drops to almost zero at the resonant wavelength of the cavity λ_C. The effective length of the cavity is

$$\begin{aligned} L_{\text{eff}} &= L_{\text{C}} + L_{\text{DBR}}, \\ L_{\text{C}} &= \frac{n}{2} \cdot \frac{\lambda_C}{n_{\text{c}}} \text{ with } n \in \mathbb{N}, \\ L_{\text{DBR}} &\approx \frac{\lambda_C}{2n_{\text{c}}} \frac{n_1 n_2}{|n_1 - n_2|} \ . \end{aligned} \tag{2.7}$$

Hereby, n_1, n_2 and n_c are the refractive indices corresponding to the materials used for the individual layers, as depicted in Fig. 2.3. The contribution L_{C} equals the optical thickness of the cavity layer while L_{DBR} accounts for the penetration of the light field into the DBRs. The light transmission rises strongly at λ_C and can be calculated as

$$T = \frac{(1-R_1)(1-R_2)}{\left(1-\sqrt{R_1 R_2}\right)^2 + 4\sqrt{R_1 R_2}\sin^2(\phi/2)} \ , \tag{2.8}$$

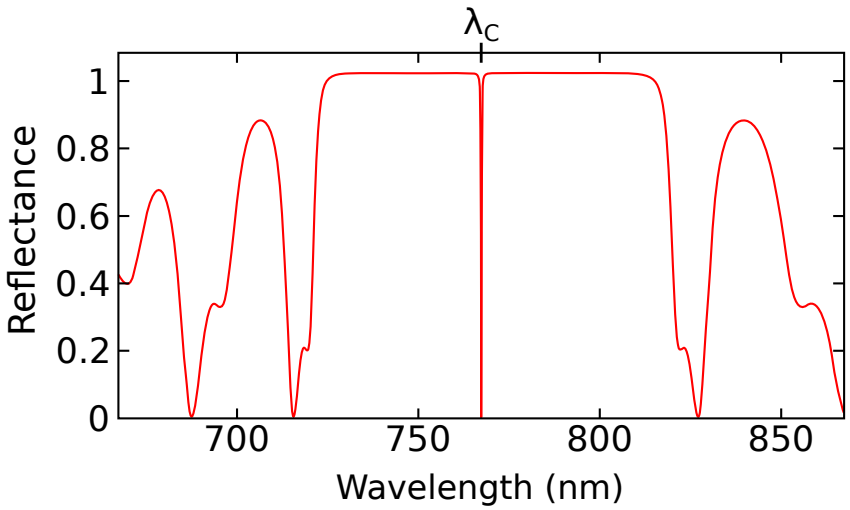

Figure 2.4: Typical reflectivity spectrum of a microcavity. A stop band with nearly 100% reflectance is formed due to the DBRs. Light may be coupled into the microcavity either at the resonant wavelength λ_C or near the Bragg minima outside the stop band. Adapted from Ref. [10].

with the reflectivities R_1 and R_2 of the top and bottom DBR and ϕ as the phase shift of the light wave after one round trip in the cavity. The Q-factor of a resonator equals the average number of round trips of a wave packet inside the resonator, before the wave packet decays and leaves it. The Q-factor of an optical microcavity is given by the full width half maximum $\Delta\lambda_C$ of the resonance at λ_C in the reflectance spectrum and can be estimated as follows:

$$Q \equiv \frac{\lambda_C}{\Delta\lambda_C} \simeq \frac{\pi(R_1R_2)^{1/4}}{1-(R_1R_2)^{1/2}} \ . \tag{2.9}$$

The related average lifetime of this exponential decay process amounts to

$$\tau_{\mathrm{Cav}} = Q/(2\pi f_C) \ , \tag{2.10}$$

with the frequency f_C of the light field [23]. High quality microcavity samples enable cavity photon lifetimes up to several 100 ps [32]. The cavity photons may interact with excitons in the quantum wells, which are placed in the central antinodes of the light field to maximize the coupling. This strong coupling yields a new type of quasiparticles called exciton polaritons, as we will discuss in section 2.1.3. To enable this coupling, one needs to transfer photons into the microcavity. This can be done either by resonant excitation at λ_C or by non-resonant excitation outside the stop band, preferably at the Bragg minima of the DBRs with almost zero reflectance. In case of resonant excitation the wavelength of the incident light beam needs to match the resonant wavelength λ_C.

When the propagation axis of a photon inside the planar cavity is not aligned exactly perpendicular to the layers, the photon moves in plane and the resonant wavelength changes to $\lambda_C/\cos\theta$. This implies an energy dispersion of the cavity photons, which reads as follows:

$$E_{\mathrm{Cav}} = \frac{\hbar c}{n_c}\sqrt{k_\perp^2 + k_{||}^2}\ , \tag{2.11}$$

with the reduced Planck's constant $\hbar$, speed of light c and the perpendicular wave vector $k_\perp = n_c(2\pi/\lambda_C)$. The in-plane wave vector $k_{||}$ results from the angle θ as

$$k_{||} = n_c\frac{2\pi}{\lambda_C}\tan\left[\sin^{-1}\left(\frac{\sin\theta}{n_c}\right)\right] \approx \frac{2\pi}{\lambda_{\mathrm{K}}}\theta, \ \text{ if } k_{||} \ll k_\perp\ . \tag{2.12}$$

Assuming $k_{||} \ll k_\perp$ we obtain a quadratic energy dispersion:

$$E_{\mathrm{Cav}} \approx \frac{\hbar c}{n_c}k_\perp \quad 1 + \frac{k_{||}^2}{2k_\perp^2}\Bigg) = E_{\mathrm{Cav}}(k_{||}=0) + \frac{\hbar^2 k_{||}^2}{2m_{\mathrm{Cav}}}\ , \tag{2.13}$$

with an effective cavity photon mass

$$m_{\mathrm{Cav}} = \frac{E_{\mathrm{Cav}}(k_{||}=0)}{c^2/n_c^2}\ , \tag{2.14}$$

which is typically on the order of $10^{-5}\,m_{\mathrm{e}}$. The cavity photon mass may be different for transversal electric (TE) and transversal magnetic (TM) polarization, leading to the so called TE-TM splitting of the energy dispersion into two parabolic branches with different curvature but same energy at $k_{||} = 0$ [33].
In the case of non-resonant excitation the wavelength of the excitation laser is per definition very different from the resonant wavelength and lies outside the stop band. Hence, the photons are not cached in the resonator and would leave the cavity instantly, unless they are absorbed. Indeed a process exists in which the non-resonant photons are absorbed and create a hot electron-hole plasma. After some relaxation processes, excitons form with energies nearby the cavity photon energies in the stop band. We regularly utilize this process for the creation of exciton polaritons, which we introduce in the next section. The non-resonant excitation process of exciton polaritons is highly relevant and will be discussed in section 2.1.4.

2.1.3 Derivation of the exciton polariton dispersion

Exciton polaritons are quasiparticles that arise when photons and excitons are coupled with each other and exchange energy on a time scale shorter than their decay and decoherence times. Thus, it is not possible to distinguish the constituting photons and excitons anymore. The amplification of the light field density in a microcavity renders it possible to reach this so called strong coupling regime more easily. In the following theoretical derivation, we consider a system of coupled quantum well excitons and

cavity photons without including their finite lifetimes. We will see that strong coupling leads to the formation of upper and lower exciton polaritons as new eigenmodes of the system with distinct in-plane energy dispersions.
We start with the Hamiltonian in second quantization using the rotating wave approximation:

$$\begin{aligned}\hat{H}_{\mathrm{Pol}} =& \hat{H}_{\mathrm{Cav}} + \hat{H}_{\mathrm{Exc}} + \hat{H}_{\mathrm{Int}} \\ =& \sum E_{\mathrm{Cav}}(k_{||},k_c)\hat{a}^{\dagger}_{k_{||}}\hat{a}_{k_{||}} + \sum E_{\mathrm{Exc}}(k_{||})\hat{b}^{\dagger}_{k_{||}}\hat{b}_{k_{||}} \\ &+ \sum \underbrace{\hbar\Omega(k_{||})}_{=:g_0}\left(\hat{a}^{\dagger}_{k_{||}}\hat{b}_{k_{||}} + \hat{a}_{k_{||}}\hat{b}^{\dagger}_{k_{||}}\right) \ .\end{aligned} \tag{2.15}$$

The operators $\hat{a}^{\dagger}_{k_{||}}$ and $\hat{a}_{k_{||}}$ are the photon creation and annihilation operators with the in-plane wave vector $k_{||}$ and the longitudinal wave vector $k_c = k \cdot \hat{z}$ given by the cavity resonance. The operators $\hat{b}^{\dagger}_{k_{||}}$ and $\hat{b}_{k_{||}}$ are the exciton creation and annihilation operators. $\Omega(k_{||})$ equals the frequency of energy exchange between excitons and photons, which gives a measure for their coupling strength. We define $g_0 = \hbar\Omega(k_{||})$ as a measure for the coupling strength in the units of energy. The Hamiltonian in Eq. 2.15 can be diagonalized using the transformation

$$\hat{P}_{k_{||}} = X_{k_{||}}\hat{b}_{k_{||}} + C_{k_{||}}\hat{a}_{k_{||}} \ , \tag{2.16}$$

$$\hat{Q}_{k_{||}} = -C_{k_{||}}\hat{b}_{k_{||}} + X_{k_{||}}\hat{a}_{k_{||}} \ , \tag{2.17}$$

with the Hopfield coefficients $X_{k_{||}}$ and $C_{k_{||}}$, which satisfy

$$\left|X_{k_{||}}\right|^2 + \left|C_{k_{||}}\right|^2 = 1 \ . \tag{2.18}$$

The diagonalized Hamiltonian reads as

$$\hat{H}_{\mathrm{Pol}} = \sum E_{\mathrm{LP}}(k_{||})\hat{P}^{\dagger}_{k_{||}}\hat{P}_{k_{||}} + \sum E_{\mathrm{UP}}(k_{||})\hat{Q}^{\dagger}_{k_{||}}\hat{Q}_{k_{||}} \ , \tag{2.19}$$

whereby the operators $(\hat{P}^{\dagger}_{k_{||}},\hat{P}_{k_{||}})$ and $(\hat{Q}^{\dagger}_{k_{||}},\hat{Q}_{k_{||}})$ are the creation and annihilation operators of the new eigenmodes of the system. These new eigenmodes may be considered as quasiparticles, which we call exciton polaritons. The exciton polariton modes are separated into two energy dispersion branches, one with a high energetic ground state (upper polaritons, UP) and another one with a low energetic ground state (lower polaritons, LP), whereas the energies are derived as

$$E_{LP,UP}(k_{||}) = \frac{1}{2}\left(E_{\mathrm{Exc}}(k_{||}) + E_{\mathrm{Cav}}(k_{||}) \pm \sqrt{4g_0^2 + (E_{\mathrm{Exc}}(k_{||}) - E_{\mathrm{Cav}}(k_{||}))^2}\right) \ . \tag{2.20}$$

According to Eqs. 2.16 and 2.17, exciton polaritons are a linear superposition of photons and excitons with identical in-plane wave vector $k_{||}$. Since the photons are bosons and the excitons also may be considered as bosons, the exciton polaritons are bosons, too. This yields the intriguing possibility of Bose Einstein condensation of exciton polaritons,

as we will discuss in chapter 2.1.4. The photonic and excitonic fractions of exciton polaritons are given by the Hopfield coefficients, as can be seen from Eqs. 2.16 and 2.17. For lower polaritons $|C_{k_{||}}|^2$ is the fraction of photons and $|X_{k_{||}}|^2$ is the fraction of excitons. For upper polaritons this assignment is flipped. With the abbreviation $\Delta E(k_{||}) = E_{\mathrm{Cav}}(k_{||},k_c) - E_{\mathrm{Exc}}(k_{||})$, their values may be calculated as follows:

$$|X_{k_{||}}|^2 = \frac{1}{2}\left(1 + \frac{\Delta E(k_{||})}{\sqrt{\Delta E(k_{||})^2 + 4g_0^2}}\right) , \tag{2.21}$$

$$|C_{k_{||}}|^2 = \frac{1}{2}\left(1 - \frac{\Delta E(k_{||})}{\sqrt{\Delta E(k_{||})^2 + 4g_0^2}}\right) . \tag{2.22}$$

As we see from Eqs. 2.21 and 2.22, the fractions of photons and excitons are given only be the energy difference $\Delta E(k_{||})$ and the constant g_0. For example in the case of $\Delta E = 0$, we obtain $|X|^2{=}|C|^2{=}\frac{1}{2}$ and the polaritons consist of photons and excitons in equal proportion. Hence, this energy difference $\Delta E(k_{||})$ is a very important parameter. In order to establish a quantitative measure we define

$$\delta \equiv E_{\mathrm{Cav}}(k_{||} = 0) - E_{\mathrm{Exc}}(k_{||} = 0) \tag{2.23}$$

as the detuning between the uncoupled exciton and cavity modes. The energy dispersions of upper and lower polaritons change for different detunings, as can be seen from Eq. 2.20. Fig. 2.5 exemplary shows the ground state energies $E_{LP,UP}(k_{||} = 0)$ and Hopfield coefficients for different values of the detuning.

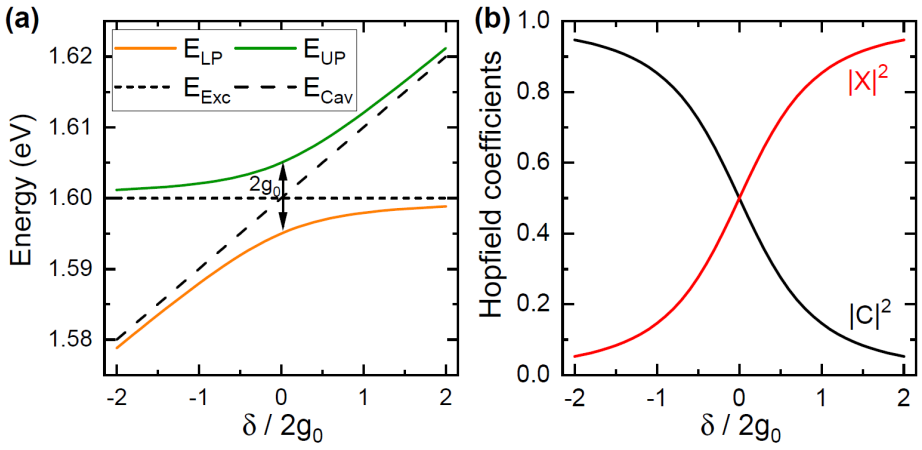

Figure 2.5: (a) Illustration of lower polariton (LP) and upper polariton (UP) ground states at $k_{||} = 0$ shifting with exciton cavity detuning. At $\delta = 0$ the UP and LP dispersions show an anti-crossing with a Rabi splitting of $2g_0$, whereas the uncoupled exciton and cavity photon modes cross. (b) Corresponding Hopfield coefficients on the same axis of detuning, which is normalized to the Rabi splitting.

The characteristic feature of strong coupling is that the dispersions of upper and lower polaritons exhibit an energy anti-crossing at $\delta = 0$. The observation of such an energy splitting indicating the strong coupling regime of polaritons in a planar semiconductor microcavity was first achieved by Weisbuch et al. in 1992 [34]. In analogy to Rabi oscillations of light interacting with atomic energy levels, this energy splitting of $2g_0$ is called the Rabi splitting of the microcavity. In contrast to the strong coupling regime, in the weak coupling regime there are only weakly coupled exciton and cavity photon modes, which show no Rabi splitting and naturally cross each other at $\delta = 0$. We discuss the quantitative criterion for distinguishing between weak and strong coupling further below, as we need to take the finite lifetimes of excitons and cavity photons into account in order to establish it. The Hopfield coefficients in the strong coupling regime are shown in Fig. 2.5(b). $|X_{k_{||}}|^2$ increases monotonously with ascending values of detuning while $|C_{k_{||}}|^2$ shows a complementary drop. This means that lower (upper) polaritons are more photonic at negative (positive) detuning and more excitonic at positive (negative) detuning. This trend also is present in the full polariton dispersion branches, which are plotted in Fig. 2.6 for exemplary data. Hereby we include the aforementioned assumptions of a constant exciton energy and a parabolic cavity photon dispersion. When $k_{||} \gg 0$, the upper polariton dispersion converges to the cavity photon dispersion and the lower polariton dispersion converges to the exciton dispersion. In the range near $k_{||} = 0$, the detuning strongly influences the shape of the dispersions. For negative detuning the lower polariton dispersion reproduces the shape of the cavity photon dispersion and the upper polariton dispersion converges to the exciton energy. With increasingly positive detuning the upper polariton dispersion converges to the cavity photon dispersion while the lower polariton dispersion flattens and converges to the exciton dispersion.

As already discussed in section 2.1.1 regarding electrons and holes, the curvature of a particle dispersion relation gives a measure for the effective mass of this particle. The masses of exciton polaritons may be extracted in a similar approach. Near $k_{||} = 0$ the dispersion may be approximated by a parabola

$$E_{\mathrm{LP,UP}}(k_{||}) \simeq E_{\mathrm{LP,UP}}(0) + \frac{\hbar^2 k_{||}^2}{2m_{\mathrm{LP,UP}}} \ , \tag{2.24}$$

with the effective polariton masses

$$\frac{1}{m_{\mathrm{LP}}} = \frac{|X|^2}{m_{\mathrm{Exc}}} + \frac{|C|^2}{m_{\mathrm{Cav}}} \ , \tag{2.25}$$

$$\frac{1}{m_{\mathrm{UP}}} = \frac{|C|^2}{m_{\mathrm{Exc}}} + \frac{|X|^2}{m_{\mathrm{Cav}}} \ . \tag{2.26}$$

Since $m_{\mathrm{Cav}} \ll m_{\mathrm{Exc}}$, we obtain

$$\begin{aligned} m_{\mathrm{LP}}(k_{||} \sim 0) &\simeq m_{\mathrm{Cav}}/|C|^2 \ , \\ m_{\mathrm{UP}}(k_{||} \sim 0) &\simeq m_{\mathrm{Cav}}/|X|^2 \ . \end{aligned} \tag{2.27}$$

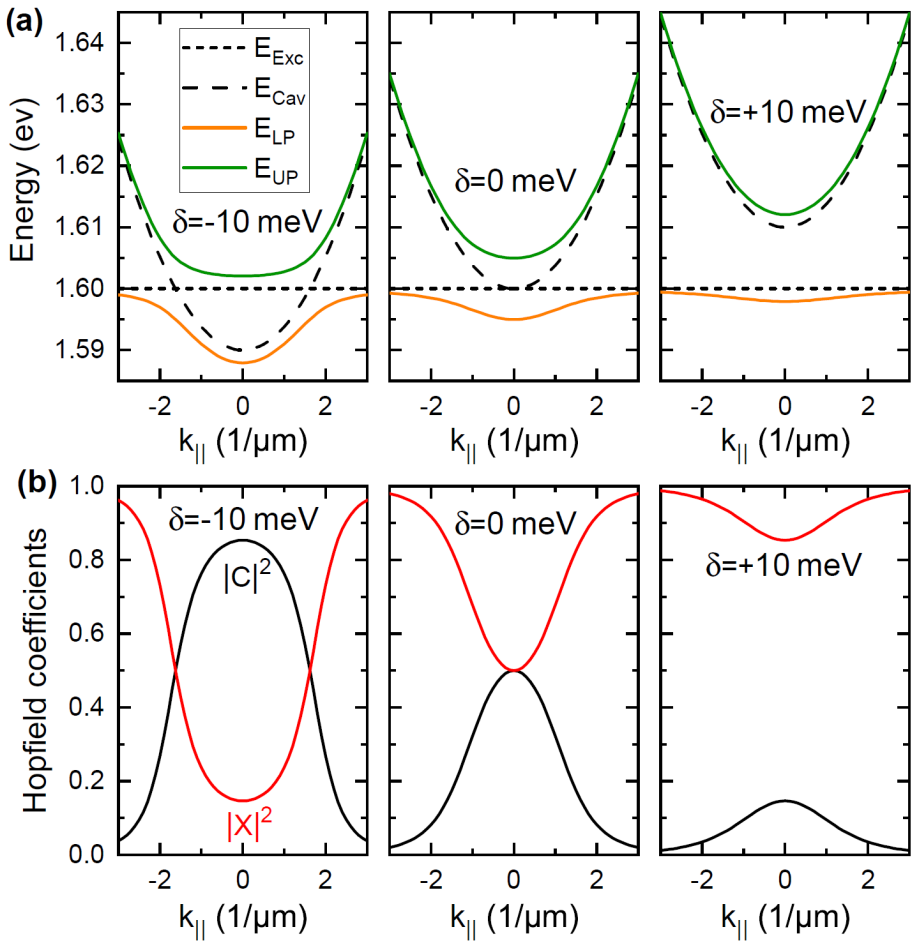

Figure 2.6: (a) Exemplary exciton polariton dispersions at different values of the detuning δ. (b) Relating Hopfield coefficients, which determine the fractions of photons and excitons.

The resulting lower polariton effective mass near $k_{||} = 0$ is on the order of $10^{-4} m_{\mathrm{Exc}}$. However, for $k_{||} \gg 0$ the lower polariton dispersion converges to the exciton mode and thereby the effective mass of lower polaritons increases by four orders of magnitude. This strongly influences the relaxation dynamics of polaritons, as we will see in section 2.1.4. The upper polaritons are practically irrelevant in the scope of this thesis, since the energetic ground state of the complete system is on the lower polariton branch. The excitons generated in the non-resonant excitation process we use, may relax into the lower polariton branch under emission of acoustic phonons. The upper polariton band is not populated strongly by this exciton relaxation process. For this reason speaking of exciton polaritons in this thesis always implies that these are polaritons in the lower polariton branch.

The theoretical derivation above does not include the fact that excitons and cavity photons have finite lifetimes τ_{Exc} and τ_{Cav}. To reach the strong coupling regime, the time scale of energy exchange between excitons and cavity photons needs to be faster than the decay processes of excitons and cavity photons. So far Eq. 2.20 does not include the case of weak coupling, as an anti-crossing is always present for arbitrarily small values of g_0. Taking into account the finite lifetimes of excitons and cavity photons modifies Eq. 2.20 as follows:

$$\begin{aligned} E_{\mathrm{LP,UP}}(k_{||}) =& \frac{1}{2}\Big(E_{\mathrm{Exc}} + E_{\mathrm{Cav}} + i(\gamma_{\mathrm{Cav}} + \gamma_{\mathrm{Exc}}) \\ & \pm \sqrt{4g_0^2 + \left[E_{\mathrm{Exc}} - E_{\mathrm{Cav}} + i(\gamma_{\mathrm{Cav}} - \gamma_{\mathrm{Exc}})\right]^2}\Big) \ , \end{aligned} \tag{2.28}$$

with the decay rates γ_{Exc} and γ_{Cav} of the exciton and cavity modes. From Eq. 2.28 we see that the real energy anti-crossing may disappear if the square root becomes zero or imaginary for small values of g_0. In this case we consider the system to be in the weak coupling regime and the excitons and photons are eigenmodes of the system. However, if the condition

$$g_0 \gg \frac{1}{2}\left(\gamma_{\mathrm{Cav}} - \gamma_{\mathrm{Exc}}\right) \tag{2.29}$$

is fulfilled, the square root is real and an anti-crossing of the modes is present. In this case we consider the system to be in the strong coupling regime and the lower and upper polaritons are the eigenmodes of the system. Such a strong coupling may be achieved in microcavities with high quality factors. Eq. 2.20 is already a sufficiently good approximation of Eq. 2.28, if $\gamma_{\mathrm{Exc}} \ll \gamma_{\mathrm{Cav}} \ll g_0$. A rough estimation of the involved decay rates shows that this is the case for polaritons in a microcavity with a high Q factor. Using $\gamma \approx \hbar/\tau$ and the values $\tau_{\mathrm{Exc}} \sim 1\,\mathrm{ns}$, $\tau_{\mathrm{Cav}} \sim 10\,\mathrm{ps}$ and $g_0 \sim 10\,\mathrm{meV}$ we obtain an estimate of $\gamma_{\mathrm{Exc}} = 10^{-7}\,\mathrm{eV} \ll \gamma_{\mathrm{Cav}} = 10^{-5}\,\mathrm{eV} \ll g_0 = 10^{-2}\,\mathrm{eV}$. Strong coupling is present and Eq. 2.20 describes the energy dispersion well.
The lifetimes of the exciton polariton modes result from the lifetimes of the excitons and cavity photons according to

$$\tau_{\mathrm{LP}} = \left(\frac{|X|^2}{\tau_{\mathrm{Exc}}} + \frac{|C|^2}{\tau_{\mathrm{Cav}}}\right)^{-1} \quad \text{and} \tag{2.30}$$

$$\tau_{\mathrm{UP}} = \left(\frac{|C|^2}{\tau_{\mathrm{Exc}}} + \frac{|X|^2}{\tau_{\mathrm{Cav}}}\right)^{-1} \ . \tag{2.31}$$

When a polariton decays from the microcavity, a photon with the same energy and in-plane wave vector $k_{||}$ is emitted. Thereby the detection of exciton polaritons is fairly easy, as the real space image of the emission gives a quantitative measure of the polariton density inside the planar microcavity. However, the excitation of polaritons in the microcavity is a bit more complicated. A straightforward way is to resonantly excite polaritons with a laser beam that matches the energy and in-plane wave vector of the polariton dispersion. Thus, exciton polaritons are formed with the same energy

and polarization. While this is an efficient approach to create exciton polaritons, it is in practice difficult to single out the signal from the polaritons, which have the same wavelength and polarization as the pump laser beam. Hence, we use a different approach to excite exciton polaritons, which is based on non-resonant excitation at a different wavelength. This approach utilizes another phenomenon known as Bose Einstein condensation of exciton polaritons, which we discuss in the next chapter.

2.1.4 Condensation of exciton polaritons under non-resonant excitation

The experimental observation of Bose-Einstein condensation (BEC) in an exciton polariton microcavity has been reported by Kasprzak et al. in 2006 [4] . Its characteristic feature in analogy to the BEC of cold atom gases is that above a certain pump power threshold an intense coherent condensate of exciton polaritons spontaneously forms at the ground state of the lower polariton branch. However, in contrast to the BEC of cold atom gases, the polariton condensate does not reach thermal equilibrium due to the finite lifetimes of exciton polaritons. Despite this, an intriguing feature of polariton condensation lies in the high critical temperature of the phase transition into the condensed phase. The criterion for the occurrence of the phase transition of a Bose gas towards a Bose-Einstein condensate is given by

$$\frac{\lambda_T^3}{v} = \zeta(3/2) \ , \tag{2.32}$$

$$\lambda_T = \frac{2\pi\hbar}{\sqrt{2\pi m k_b T}} \ , \tag{2.33}$$

with $\zeta(3/2) = 2.6124$, the particle volume v and the thermal de Broglie wavelength λ_T of a particle with mass m at the temperature T [35]. According to Eq. 2.32, BEC occurs when the thermal de Broglie wavelength becomes comparable to the distance between the particles ($\sim v^{1/3}$). Solving this formula for T yields the critical temperature of BEC

$$T_K = \frac{2\pi\hbar^2}{m k_b} \left(\frac{1}{v \cdot \zeta(3/2)} \right)^{2/3} \ , \tag{2.34}$$

which is inversely proportional to the mass of the bosonic particles. In atom gases the resulting critical temperature for BEC is very low, for instance $\sim 2\,\mu$K for a gas of sodium atoms [36]. However, with $m \approx 10^{-5} m_e$ the exciton polaritons are very light compared to atoms so that even critical temperatures approaching room temperature are possible. This is a special peculiarity of exciton polariton condensates. Nevertheless, the fact that in most semiconductor materials excitons thermally break up far below room temperature remains a big practical obstacle for polariton condensation at room temperature. A significantly higher exciton binding energy would be necessary to have stable exciton formation and reach polariton condensation even at room temperature.

Now we consider polariton condensation in more detail. As already mentioned before, a non-resonant laser is used to couple light into the microcavity outside of the stop band. This excitation locally creates an electron-hole plasma. Fig. 2.7 illustrates the whole condensation process originating from this electron-hole plasma towards the formation of a polariton condensate at the ground state of the lower polariton dispersion.

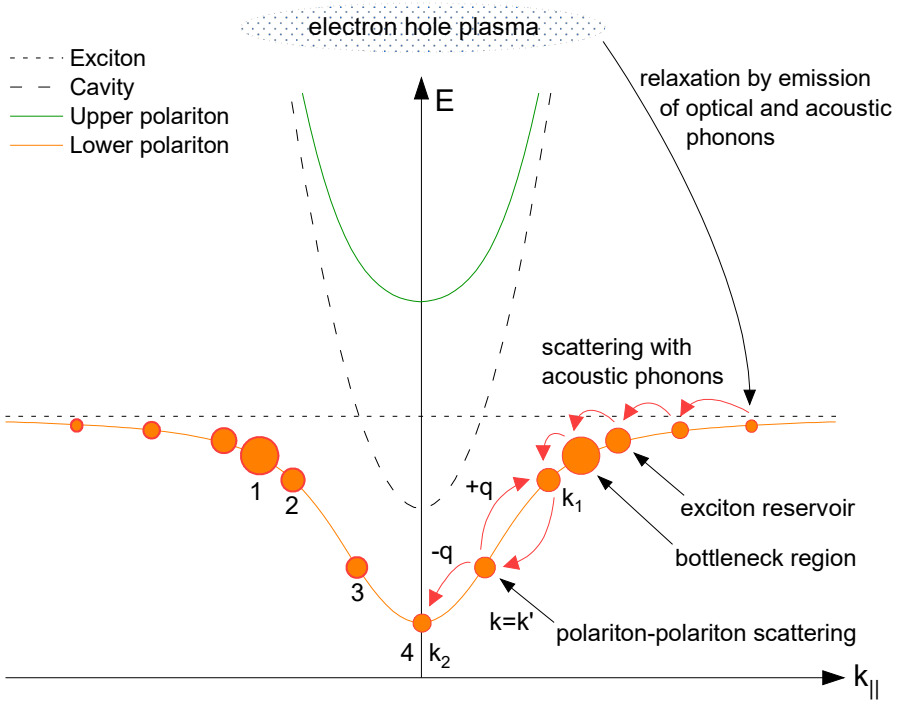

Figure 2.7: Illustration of the excitation and relaxation of exciton polaritons created by non-resonant pumping below the condensation threshold. Exciton polaritons populate different regions of the lower polariton branch with varying densities. The sizes of the circles roughly indicate the population densities in the corresponding regions below condensation threshold. Above condensation threshold, a polariton condensate with high population density forms in the ground state (region 4) due to non-linear polariton-polariton scattering. A detailed explanation of the condensation process is given in the text. Adapted from Ref. [10, 37].

The hot electrons and holes from the excited electron-hole plasma relax by emission of optical and acoustic phonons and form excitons due to Coulomb attraction [38]. The excitons relax further along the lower polariton branch by scattering with acoustic phonons [39] and form a reservoir at energies slightly below the bare exciton mode (region 1). As the curvature of the dispersion rises when approaching $k_{||} = 0$, the polaritons at small $k_{||}$ become more photonic. Hence, the mass of the polaritons decreases while their decay rate increases. Simultaneously the density of states on the polariton dispersion (which is inversely proportional to the curvature) drops, which results in a bottleneck region where the majority of polaritons decays before relaxing further down

the dispersion (region 2). When the polariton density is high, this bottleneck can be overcome by intermediate polariton-polariton scattering (region 3) towards the ground state (region 4). In that case, polariton-polariton scattering is stimulated by the polariton population in the ground state [37, 40]. Once the excitation pump power exceeds a certain threshold at which the stimulated scattering of polaritons into the ground state becomes more efficient than the polariton decay process, a high density polariton condensate in the ground state forms. This behavior is similar to a laser, in which photons stimulate the emission of even more photons and thereby non-linearly increase the photon number in a certain mode. Once the gain of the light field mode exceeds the losses of the resonator, lasing sets in and a coherent light wave is emitted. However, the gain medium in a laser requires a population inversion of two energy levels to show lasing, whereas this is not the case in the polariton system. The polaritons continuously relax along the polariton dispersion and finally scatter into the ground state. Thereby, the critical particle density per quantum well at the condensation threshold is several orders of magnitude smaller compared to a classical laser [10].
A more quantitative description of the polariton dynamics is possible using semi classical Boltzmann rate equations. Considering the polariton populations $n_0(t)$ of the ground state at $k = 0$ and $n_{\vec{k}}(t)$ of the excited states, the rate equations describing their occupation read as follows:

$$\frac{\partial}{\partial t} n_{\vec{k}} = P_{\vec{k}}(t) - \frac{n_{\vec{k}}}{\tau_{\vec{k}}} + \frac{\partial}{\partial t} n_{\vec{k}}\Big|_{\text{LP-LP}} + \frac{\partial}{\partial t} n_{\vec{k}}\Big|_{\text{LP-ph}} \ , \tag{2.35}$$

$$\frac{\partial}{\partial t} n_0 = -\frac{n_0}{\tau_0} + \frac{\partial}{\partial t} n_0\Big|_{\text{LP-LP}} + \frac{\partial}{\partial t} n_0\Big|_{\text{LP-ph}} \ . \tag{2.36}$$

Hereby, $P_{\vec{k}}(t)$ is the time dependent pump rate, τ_0 is the polariton lifetime in the ground state and $\tau_{\vec{k}}$ denotes the lifetime of polaritons at the respective wave vector $\vec{k}$. The rate of polariton-phonon scattering is given by

$$\frac{\partial}{\partial t} n_{\vec{k}}\Big|_{\text{LP-ph}} = -\sum_{\vec{k}'} \left[W^{\text{LP-ph}}_{\vec{k}\to\vec{k}'}\, n_{\vec{k}}(1 + n_{\vec{k}'}) - W^{\text{LP-ph}}_{\vec{k}'\to\vec{k}}\,(1 + n_{\vec{k}}) n_{\vec{k}'} \right] \ , \tag{2.37}$$

with the transition rates $W^{\text{LP-ph}}_{\vec{k}\to\vec{k}'}$ and $W^{\text{LP-ph}}_{\vec{k}'\to\vec{k}}$. This polariton-phonon scattering process is a dissipative cooling mechanism of the polaritons.
The rate of polariton-polariton scattering is given by

$$\begin{aligned} \frac{\partial}{\partial t} n_{\vec{k}}\Big|_{\text{LP-LP}} = -\sum_{\vec{k}',\vec{k}_1,\vec{k}_2} W^{\text{LP-LP}}_{\vec{k},\vec{k}',\vec{k}_1,\vec{k}_2} \Big[& n_{\vec{k}} n_{\vec{k}'} (1 + n_{\vec{k}_1})(1 + n_{\vec{k}_2}) \\ & - n_{\vec{k}_1} n_{\vec{k}_2} (1 + n_{\vec{k}})(1 + n_{\vec{k}'}) \Big] \ , \end{aligned} \tag{2.38}$$

with $\vec{k}_1 = \vec{k} + \vec{q}$, $\vec{k}_2 = \vec{k}' - \vec{q}$ and the transition rate $W^{\text{LP-LP}}_{\vec{k},\vec{k}',\vec{k}_1,\vec{k}_2}$. The polaritons with wave vector $\vec{k} = \vec{k}'$ interact with each other and are scattered to the wave vectors $\vec{k}_1$ and $\vec{k}_2$.

The total energy of the polaritons is not reduced in this process, which typically takes place withing with few picoseconds.
The buildup of a polariton population n_0 in the ground state requires $\frac{\partial}{\partial t} n_0 \geq 0$. According to Eq. 2.36, the contribution of the radiative decay $-\frac{n_0}{\tau}$ is negative. Also the polariton phonon scattering term $\frac{\partial}{\partial t} n_0\Big|_{\text{LP-ph}}$ is negative in most cases, since the scattering of polaritons away from the ground state is more likely than in reverse direction back to the ground state. The remaining polariton-polariton scattering term $\frac{\partial}{\partial t} n_0\Big|_{\text{LP-LP}}$ needs to compensate these negative terms. This is possible due to its dependence on the polariton population n_0, which stimulates further scattering into the ground state. Hence, a coherent polariton condensate forms.
In general, the dynamics of a condensate in the ground state of a quantum mechanical many body system may be described by the Gross-Pitaevskii equation (GPE)

$$i\hbar \frac{\partial}{\partial t} \Psi(\mathbf{r},t) = \left(-\frac{\hbar^2 \nabla^2}{2m} + V_{\text{ext}}(\mathbf{r},t) + g \left|\Psi_0(\mathbf{r},t)\right|^2 \right) \Psi(\mathbf{r},t) \ , \tag{2.39}$$

whereby $\Psi(\mathbf{r},t)$ is the condensate wave function, V_{ext} is an external potential, m is the mass of the Boson particles and g is the coupling constant [41]. The sign of g indicates if the interaction between the particles forming the condensate is attractive ($g < 0$) or repulsive ($g > 0$). In addition to mutual interaction, the particles in the condensate phase may also interact with other particles in the system. In particular, when considering exciton polariton condensates, the polaritons in the condensate may interact with other carriers excited in the system such as electrons, holes and excitons. The effect of these carriers on the polariton condensate then may be included by a non-trivial external potential $V_{\text{ext}}(\mathbf{r},t)$ in Eq. 2.39. Since the electron-hole plasma and exciton reservoir are generated by a non-resonant optical excitation process, we may all-optically imprint an external potential to shape the polariton condensate and control the flow of polaritons [42]. In detail, the potential is mostly given by repulsive coulomb interaction of the polariton condensate with reservoir excitons. When considering the typical time scale of the relaxation process of the electron-hole plasma, we see that a high population density of reservoir excitons builds up. The non-resonantly excited electron-hole plasma typically decays rapidly in less than 20 ps due to optical and acoustical phonon emission and forms excitons at high wave vectors with typical lifetimes of around 400 ps [38]. Despite their high wave vectors, excitons move slowly as they have high effective masses. This means that reservoir excitons remain localized during their lifetime close to the spot where they have been generated by relaxation from the non-resonantly excited electron-hole plasma. Consequently, a density pattern imprinted by a spatially shaped non-resonant laser beam is mostly conserved and may act as an effective potential for polaritons, since the interaction of polaritons with reservoir excitons is repulsive under most experimental conditions and attractive only in few rare cases [43]. Since the polaritons inherit their spatial density distribution from the reservoir excitons, the location of a forming polariton condensate often coincides or significantly overlaps with the external potential generated by the exciton reservoir. However, depending on the potential height (scaling with excitation power),

polaritons are repelled by this potential, which allows to control polariton flows and shape polariton condensates [44, 45]. It has been shown that the polariton condensate and optically imprinted excitation pattern in fact might be spatially separated from each other [46]. By tailoring the spatial shape of the non-resonant excitation laser, the flow of polaritons may be controlled and guided all optically [42]. Such a spatial structuring of the excitation laser beam can be achieved by using tailored diffractive optical elements, as we explain in the next section.

2.2 Shaping light beams with diffractive optical elements

Let us consider a monochromatic plane wave with the wavelength λ propagating in vacuum under a tilted angle α with respect to a fixed optical axis, as illustrated in Fig. 2.8. The wave vector $\mathbf{k}$ of the light wave with $|\mathbf{k}| = \frac{\lambda}{2\pi}$ may be separated into a perpendicular part $\mathbf{k}_\perp = \cos(\alpha)|\mathbf{k}|$ and a parallel part $\mathbf{k}_{||} = \sin(\alpha)|\mathbf{k}|$ with respect to the normal plane perpendicular to the optical axis. Following the wavefront of the

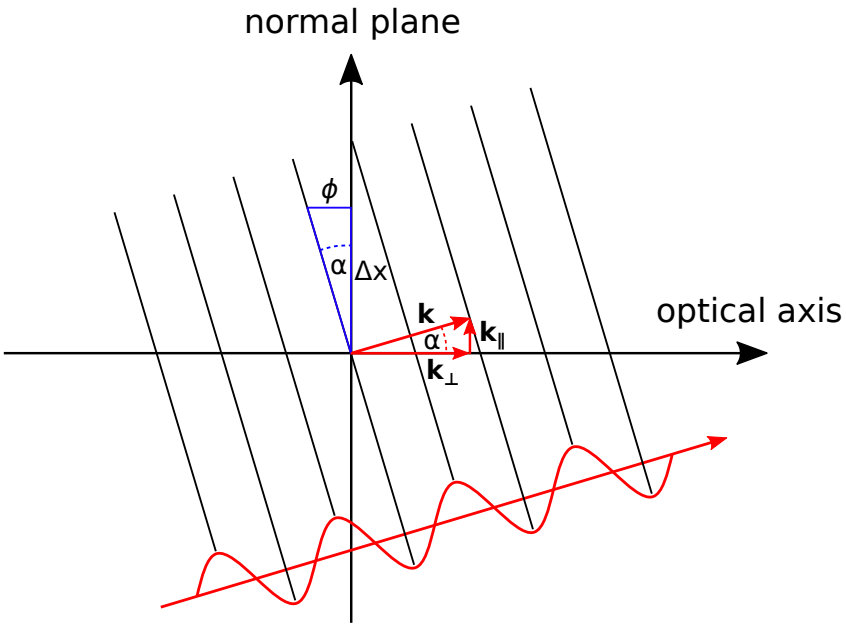

Figure 2.8: Illustration of plane wave propagating under a tilted angle α with respect to the optical axis.

plane wave shows that the phase is $\phi = \tan(\alpha)\Delta x$ with the gradient $\nabla\phi = \tan(\alpha)$ in the normal plane. In paraxial approximation the angle α is small and $\sin(\alpha) \approx \tan(\alpha)$

applies. In this case the perpendicular wave vector $k_{||}$ directly corresponds to the phase gradient $\nabla\phi$ of the light wave. Moreover, the phase gradient in the normal plane physically defines the angle and direction of the propagating light wave. This yields the possibility to spatially shape a light beam by introducing an optical element, which locally shifts the phase of an incident the light beam in the normal plane by a function $\phi(\mathbf{r},t)$.
In principle a light beam can be formed to any spatial shape (within the diffraction limit) by using an optical element with a suitable phase function. For example phase plates or high resolution spatial light modulators (SLMs) may be used as diffractive optical elements to locally shift the phase of an incident light beam. Thereby a phase shift in the range of $[0,2\pi]$ is sufficient to arbitrarily shape the light beam, because of the periodic nature of a light wave. For convenience usually a normally incident light beam with almost plane wavefront is used in such applications. However, one still needs know the correct phase pattern to form the light beam to the desired shape. This problem may be solved by computing the required phase pattern for example by using the Gerchberg-Saxton algorithm [47], which generates a suitable phase pattern for shaping the light beam to the desired intensity profile in the far field. Considering the fact that we may use a spatially shaped light beam to imprint optical potentials in a two-dimensional exciton polariton system gives an idea of the wide variety of possible experiments and applications involving exciton polaritons. However, when imaging the spatially modulated light beam using additional optical elements such as lenses, we need to take into account that these lenses perform optical Fourier transformations of the light beam (as we will discuss later on in section 2.5), which also need to be considered in order to shape the light beam to the desired intensity profile in the final imaging plane. In concrete terms, we need to take into account that the microscope objective used for focusing the excitation laser beam onto the sample performs an additional Fourier transformation, which is not included in the usual Gerchberg-Saxton algorithm. A practical approach to deal with this additional Fourier transformation is to compensate it by using one more lens that performs yet another optical Fourier transformation. Such an optical setup consisting of a lens and microscope objective is suitable to image the real space of the spatially modulated laser beam onto the sample, as shown in Ref. [11].
Within the scope of this thesis, the phase elements used for shaping the excitation laser beam do not need to be specifically computed, as we follow the suggestion of Ref. [18] to use an annular trapping potential, which we may create easily by imprinting an axicon phase pattern and focusing the thereby conical shaped laser beam onto the microcavity sample. This approach is similar to Refs. [46, 48], where actual glass axicons were used to create annular polariton traps. Fig. 2.9 gives a rough impression of how a light beam is shaped by phase elements exhibiting axicon phase patterns or linear phase gradients, which we both use later on in our experiments. Furthermore, the phase element with linear phase gradient acts like a diffraction grating due to its periodicity and in practice generates many diffractive orders.

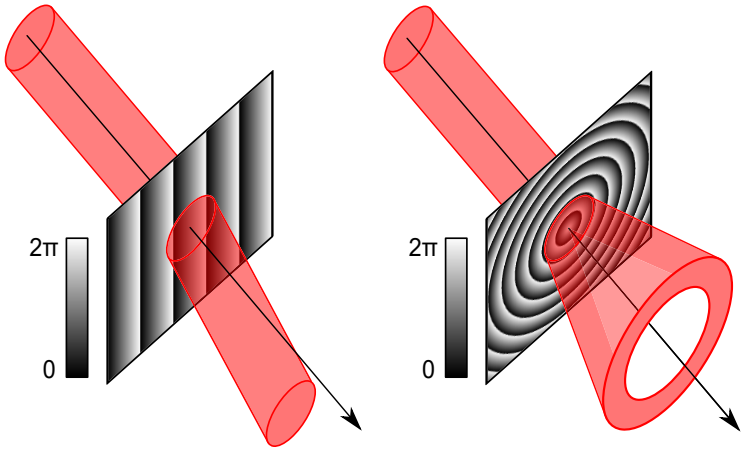

Figure 2.9: Two exemplary phase elements, which may be used to shape a laser beam with a phase modulating SLM. The linear phase gradient pattern deflects the light beam along the direction of the gradient, while the axcion phase pattern creates a ringlike beam profile.

Finally, it should be noted that the intensity profile of a light beam may also be shaped by passing it through an optical element with spatially varying absorption coefficient. However, doing so does not directly change the wave vector, which limits the possible ways of shaping the beam. For example one may not create optical vortices, in which the wavefront has a helical shape, as we discuss in the next section.

2.3 Vortex formation in exciton polariton condensates

Quantized vortices are topological states in quantum fluids such as superfluids or 2D BECs. Historically considered, quantized vortices first have been observed as vortex lines in rotating superfluid helium [49]. Since then vortices in quantum fluids have been investigated and found to exist even in exciton polariton condensates [9], which strictly speaking are not true BECs since thermal equilibrium is not reached due to the non-persistent nature of exciton polaritons. Vortices of excitons polaritons in a microcavity are two-dimensional excitations, whereat the in-plane movement of the polaritons is associated with the phase gradient of the polariton wave function. Hence, the characteristic feature of exciton polariton vortices is a central core with almost zero intensity and a local phase winding of the shape $\Psi \propto \exp(-im\phi)$, whereby m is called the topological charge of the vortex. In one revolution around the center, the phase runs through a value range from zero to $2\pi m$. In radial direction the phase is constant for each angle. Fig. 2.10 illustrates the spatial phase structure of a vortex with topological charge $m = 1$. In general the topological charge of a vortex in a field

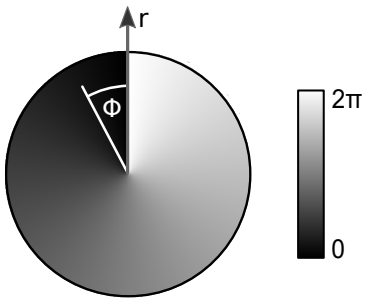

Figure 2.10: Phase of a vortex with topological charge $m = 1$.

may be extracted by integrating the phase along a closed contour C surrounding the vortex:

$$m = \frac{1}{2\pi} \oint_C \vec{\nabla} S \cdot \vec{dl} \tag{2.40}$$

At this, S is the scalar phase of the field with $\Psi = |\Psi| \exp(iS)$. Higher order vortices in a light field show the tendency to split into vortices with unit charge $|m| = 1$ [50].

Several studies show that quantized vortices also may spontaneously form in exciton polariton systems [9, 14]. In these the vortices are pinned due to the static disorder of the sample. Other studies show that vortices also may be imprinted by resonant excitation [13, 16, 51] or form due to the dynamics of interacting polariton currents [17]. The in-plane polariton motion may be confined further by manufacturing cylindrical optical traps [12, 52], which enables the localized excitation of exciton polariton

vortices. However, this requires physically structuring the microcavity sample. A more flexible approach is the non-resonant excitation of carriers to form an external potential in addition to the always present static disorder potential, which also shapes the polariton condensate [45, 53]. Concurrently, the non-resonantly excited electron-hole plasma relaxes and may create exciton polariton condensates shaped by the all optically imprinted potential [46, 48, 54]. It has been demonstrated that also polariton condensates containing vortices may be formed by using a non-resonant pump laser with tailored beam profile [15]. In this thesis we follow the theoretical suggestion of our cooperation partners Ma et al. [18, 19], who propose the use of an annular pump beam to create a ringlike potential trap, in which localized polariton vortices with integer topological charges are expected to form spontaneously. Furthermore, a concept for switching the topological charge of such vortices is suggested. With increasing trap diameter, also vortices with higher topological charges $|m| > 1$ may arise [18]. Due to continuity of the field, only quantized vortices with integer topological charge form stationary solutions of the GPE [51]. However, in non-stationary processes we may not be allowed to assume just integer topological charges. Our all optical approach for trapping polaritons enables a versatile tuning of the trap parameters. The localization of the vortices inside the traps allows for advanced experiments to manipulate their topological charge, as we will see later on in chapter 4.3.
The physical size of the vortices is determined by the topological charge and the pump power dependent healing length, which is the typical length scale over which ψ can change significantly. In the polariton system, which is a non-equilibrium dissipative system, the effective healing length is given by

$$\xi(\mathbf{P}) = \frac{\hbar}{\sqrt{2mg_{\text{eff}}|\Psi_0(\mathbf{P})|^2}} \ , \tag{2.41}$$

with the pump power dependent field intensity $|\Psi_0(\mathbf{P})|^2$, the polariton mass m and an effective interaction constant g_{eff} [55]. As one can see from Eq. 2.41, the healing length drops with increasing field intensity $|\Psi_0(\mathbf{P})|^2$. Thereby the physical size of a vortex, which is on the order of the healing length, also drops with increasing excitation power.
In general, the investigation of vortices in a BEC is not trivial, as it experimentally requires access to the density and phase of the quantum fluid wave function. In 2D atomic BECs the density is typically probed by a time of flight method, in which the trapping potential is switched off and the BEC expands while falling. Then a resonant laser illuminates the BEC and the shadow of the transmitted light is recorded using a camera [56]. In contrast to this, exciton polaritons are fairly easy to probe since polaritons emit photons when decaying from the microcavity. Since the phase of the emitted photons corresponds to the phase of the polariton wave function, polariton vortices in the microcavity translate into optical vortices with equal topological charges in the emitted light beam. Still, probing optical vortices usually requires spatially resolved interferometry techniques. In case of observing dynamical vortex processes with time dependence, the experimental effort increases further to do time-resolved interferometry. Here, our novel approach to detect exciton polariton vortices comes into play. Since light beams with optical vortices carry OAM, we conceptually may

use OAM sorting to detect these vortices and perform OAM resolved spectroscopy of them. In the next chapter the fundamentals of the OAM of light are highlighted.

2.4 Orbital Angular Momentum of light

A transverse electromagnetic wave carries linear momentum and angular momentum with the cycle averaged momentum densities

$$\mathbf{p} = \epsilon_0 \langle \mathbf{E} \times \mathbf{B} \rangle \ , \tag{2.42}$$

$$\mathbf{j} = \mathbf{r} \times \mathbf{p} = \epsilon_0 \mathbf{r} \times \langle \mathbf{E} \times \mathbf{B} \rangle \ , \tag{2.43}$$

whereby ϵ_0 is the vacuum permittivity [57]. The total angular momentum of a light field then simply results from integrating the density given by Eq. 2.43:

$$\mathbf{J} = \epsilon_0 \int d\mathbf{r}\ \mathbf{r} \times \langle \mathbf{E} \times \mathbf{B} \rangle \tag{2.44}$$

The fact that light waves may carry angular momentum is already long known since the works of John Henry Poynting more than a century ago. In 1884 he quantified the momentum and energy flux of electromagnetic fields for the first time [58]. Based on an analogy with the wave motion associated with a line of dots marked on a rotating cylindrical shaft, he later reasoned that circularly polarized light must carry angular momentum [59]. This was experimentally confirmed by Beth in 1936 [60]. Since then light was known to have circular polarization with a spin angular momentum of $\pm\hbar$ per $\sigma^{\pm}$ polarized photon. However, for a long time it was not noticed that the polarization does not account for all angular momentum in Eq. 2.44. In 1992 Allen pointed out that there is an additional component, which arises from the spatial phase of the wavefront: The orbital angular momentum. It was shown that Laguerre-Gaussian modes (which are solutions of the paraxial wave equation) given by

$$u_{p,l}(r,\phi,z) = \frac{C}{(1+z^2/z_R^2)^{1/2}} \left(\frac{r\sqrt{2}}{w(z)}\right)^l L_p^l\left(\frac{2r^2}{w^2(z)}\right) \exp\left(\frac{-r^2}{w^2(z)}\right) \exp\left(\frac{-ikr^2 z}{2(z^2+z_R^2)}\right) \cdot \exp(-il\phi) \exp\left(i(2p+l+1)\tan^{-1}\frac{z}{z_R}\right) \tag{2.45}$$

carry OAM related to l. Here, z_R is the Rayleigh range, $w(z)$ is the radius of the beam, L_p^l is the associated Laguerre polynomial, C is a normalization constant and the beam waist is located at $z = 0$ [61]. Analogy between the Schrödinger wave equation and paraxial wave equation suggests that such Laguerre-Gaussian modes are eigenmodes of the angular momentum operator L_z and carry an OAM of $l\hbar$ per photon [61]. In the case of $p = 0$ the Laguerre-Gaussian modes take a shape $\propto exp(-il\phi)$, which equals the phase of an optical vortex. Because of this optical vortices with an integer topological charge m carry exactly this amount of OAM. Furthermore, the Laguerre-Gaussian

modes are orthonormal in both indices l and p under integration over the full r,ϕ plane [50]:

$$\int_0^{2\pi} d\phi \int_0^{\infty} r dr \; u_{p,n}(r,\phi,z) \left[u_{q,l}(r,\phi,z)\right]^* = \delta_{n,l}\delta_{p,q}. \tag{2.46}$$

Thus, even the subset of Laguerre-Gaussian modes with $p = 0$ and varying integer l still is an infinite set of orthogonal modes. These optical vortex modes may be easily generated using phase plates or spatial light modulators, which yields potential for applications in optical communication technology. An elegant method for detecting such optical vortex modes is OAM sorting, which we will discuss in the next section. This method potentially enables the detection of quantized vortices forming in exciton polariton condensates. As discussed before, the stable vortex solutions of the GPE show just integer topological charges due to continuity reasons. However, for time dependent non-stationary processes we may not in general assume the topological charge of vortex-like phase structures to be limited to integer values only. Thus, we also give some consideration to the special case of fractional vortices with non-integer topological charges. For benchmarking purposes, they may be experimentally generated by using phase plates or SLMs just in the same way as optical vortices with integer topological charges are created.
A light beam with an optical vortex of non-integer topological charge is not rotationally symmetric anymore. A phase discontinuity arises where the phase jumps by a non-multiple of 2π and the intensity is locally reduced. In this case the light beam carries non-zero transverse momentum

$$\mathbf{P}_{x,y} = \epsilon_0 \int d\mathbf{r} \; \langle \mathbf{E} \times \mathbf{B} \rangle_{x,y} \; , \tag{2.47}$$

which leads us to the distinction between intrinsic and extrinsic OAM. It can be shown that the total angular momentum of a light beam according to Eq. 2.44 is independent of the lateral position of the calculation axis $\mathbf{r_0} \equiv (r_{0x},r_{0y})$, if the transverse momentum $\mathbf{P}_{x,y}$ vanishes [62]. In this case we consider the OAM of the light beam to be intrinsic. However, in case of non-zero transverse momentum, the OAM of the light beam depends upon the choice of the lateral calculation axis. In this case we consider the OAM to be extrinsic. Such extrinsic OAM corresponding to non-zero transverse momentum may arise for example when a light beam with OAM passes through an off-axis aperture [63]. The OAM of light beams with optical vortices of integer topological charges is always intrinsic, as their rotational symmetry implies zero transverse momentum. However, the mean OAM $\bar{m}$ and topological charge m of a light beam with a fractional vortex may differ according to [64, 65]

$$\bar{m} = m - \frac{\sin(2\pi m)}{2\pi} \; . \tag{2.48}$$

Alperin et al. [66, 67] showed, that the total OAM (which is proportional to the mean OAM) of a light beam with a fractional vortex may be decomposed into intrinsic

and extrinsic OAM components. While even for vortices with non-integer topological charges the intrinsic OAM is always equal to m, the extrinsic components cause a sinusoidal oscillation of the mean OAM, as can be seen in Eq. 2.48. Furthermore, Alperin et al. [67] showed that using a cylindrical lens under different rotation angles renders it possible to selectively detect either the intrinsic OAM component or the total OAM of a light beam. In case of vortices with integer topological charges, the extrinsic components completely vanish and the mean OAM and intrinsic OAM are equal. Also it should be mentioned that light beams with fractional OAM are not stable upon propagation and typically decay into many stable vortices with $|m| = 1$ during propagation [65].

2.5 OAM Sorting

As we have seen in the last chapter, the appearance of optical vortices is closely linked to the OAM of light. While simple ways of generating OAM modes using holograms [68] and phase plates [69] have been demonstrated, the detection of optical vortices in a light beam usually is a non-trivial task. In most cases interferometric techniques are utilized to detect vortices in a light field. For example a typical approach for detecting vortices in exciton polariton condensates is using a Michelson interferometer to extract the real space phase map of the light emission [9]. However, when considering orthogonal OAM modes of a light beam as separate channels for information transfer, such an approach is by far not efficient as first of all the phase map needs to be reconstructed and then vortices may be identified afterwards. Also superpositions of spatially overlapping OAM modes with different l would be very hard to correctly identify and distinguish. The potential use of different OAM modes for information transfer has lead to several more sophisticated approaches from the optics community to measure OAM of a light beam. For example a free-space communicator based on OAM modes has been demonstrated [70]. Also the detection of OAM at the single-photon level has been demonstrated in quantum optics experiments [71]. In 2002, Leach et al. showed that an OAM mode sorter with in principle 100% efficiency may be realized by using a cascaded setup of Mach-Zehnder interferometers containing Dove prisms [72]. However, the experimental effort to build such a mode sorter vastly increases with the number of output ports, as detecting N possible states requires $N - 1$ interferometer stages. The concept of sorting a light beam of superposed OAM modes onto fractions of the composing OAM modes was later picked up by Berkhout et al. [21], who suggested and demonstrated an OAM sorting setup that allows the simultaneous detection of multiple OAM states by implementing an optical transformation with tailored phase elements. We focus on this OAM sorting method, as it maps a set of OAM states to a linear line of distinct spots, whereas the spot positions are proportional to l. In detail, this method unwraps the helical phase gradient of an OAM state to a linear phase gradient by using two tailored diffractive optical elements. The resulting linear phase gradient is proportional to l and directly corresponds to the in-plane wave vector, as discussed in chapter 2.2. By the subsequent imaging with a lens, which performs an optical Fourier transform of the

light beam (as we discuss further below), the OAM sorted light beams with wave vectors proportional to l are imaged onto distinct spots in the plane of detection. Hence, the mapping of OAM states with different l results in a line of distinct spots, which are easily detectable using a camera.
The basic OAM sorting setup including intensity and phase maps of all involved planes during an exemplary mapping of a $l = 3$ OAM state is shown Fig. 2.11. The exemplary intensity and phase maps are obtained by simulating the beam propagation through the OAM sorting setup. Details on this simulation, which we use to optimize the experimental implementation of OAM sorting, are given in subsection 2.5.1.
The core elements of the OAM sorting setup are the transformation phase pattern and the phase correction pattern. The transformation pattern performs a mapping $(x,y) \mapsto (u,v)$ with $v = a \arctan(y/x)$ and $u = -a \ln\left(\sqrt{x^2+y^2}/b\right)$. The corresponding phase element required to achieve such a mapping is given by

$$\phi_1(x,y) = \frac{2\pi a}{\lambda f_{\mathrm{OAM}}} \left[y \arctan\left(\frac{y}{x}\right) - x \ln\left(\frac{\sqrt{x^2+y^2}}{b}\right) + x \right]. \tag{2.49}$$

Following the beam path in Fig. 2.11, one can see how the intensity ring of the $l = 3$ OAM state is unwrapped by the transformation pattern. Subsequently, a lens transforms the light field into the Fourier plane, where the field has a linear stripe intensity profile. However, the optical transformation leads to a non-trivial phase structure due to the different pathways of all light bundles. Thus, a second phase pattern is applied in order to correct for these phase shifts. It is given by

$$\phi_2(u,v) = -\frac{2\pi ab}{\lambda f_{\mathrm{OAM}}} \exp\left(-\frac{u}{a}\right) \cos\left(\frac{v}{a}\right). \tag{2.50}$$

As one can see from the example in Fig. 2.11, application of the phase correction pattern results in a linear shift of $2\pi l$ at the location of the intensity stripe. Finally, a lens performs an optical Fourier transformation that images the light beam onto elongated spots in the detector plane, whereby the linear phase gradient leads to a deflection of the spot position with respect to the central symmetry axis of the phase elements. The optical Fourier transformation of a lens is illustrated in Fig. 2.12 using a simple ray optics picture. Light bundles with same in-plane momentum (or angle) in the front focal plane are imaged onto spots in the back focal plane at positions proportional to the initial in-plane momentum. Since in-plane momentum and phase gradient of a light beam equal each other in paraxial approximation, light beams with linear phase gradients resulting from the OAM sorting process are imaged onto spots in the plane of detection at positions proportional to the OAM of the initial light beam guided into the OAM sorting setup. In detail, the spot positions corresponding to each OAM state may be calculated according to

$$t_l = \frac{\lambda f_{\mathrm{Imag}}}{d} l \ , \tag{2.51}$$

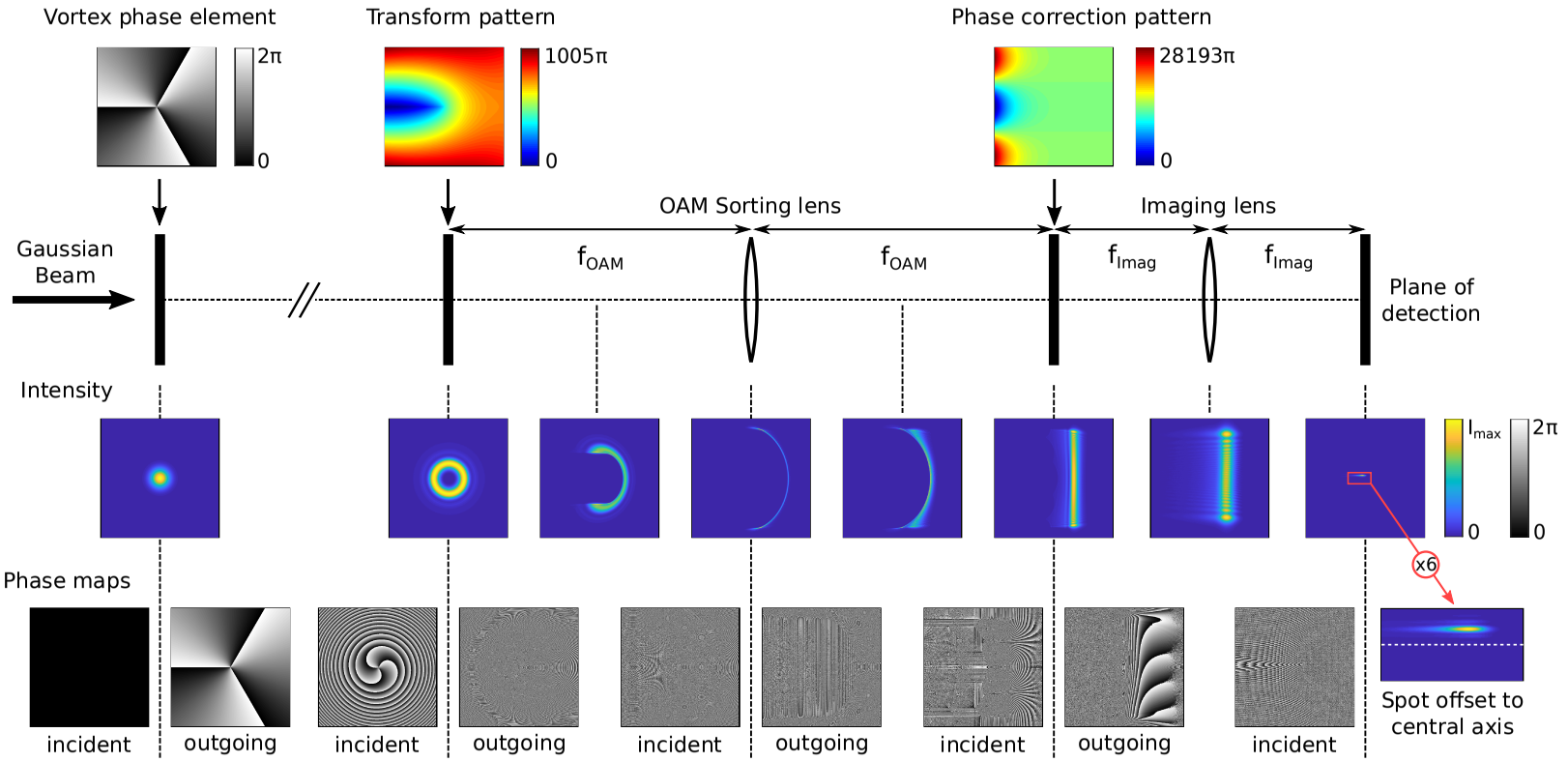

Figure 2.11: Sketch of the optical OAM sorting setup including the simulated transformation of an OAM beam with $l = 3$. The OAM sorting setup consists of two tailored phase pattern for transformation and phase correction of the beam. The simulated intensity images and phase maps show how a beam with a $l = 3$ vortex phase is unwrapped by the transformation pattern to a linear stripe. After application of the phase correction pattern, a $2\pi l$ linear phase gradient arises. Finally, an imaging lens focuses the beam onto a well defined spot in the detector plane. This spot is offset from the optical axis, whereby the position scales linearly with l. Thus, the simultaneous detection of multiple superposed OAM states with different l is possible.

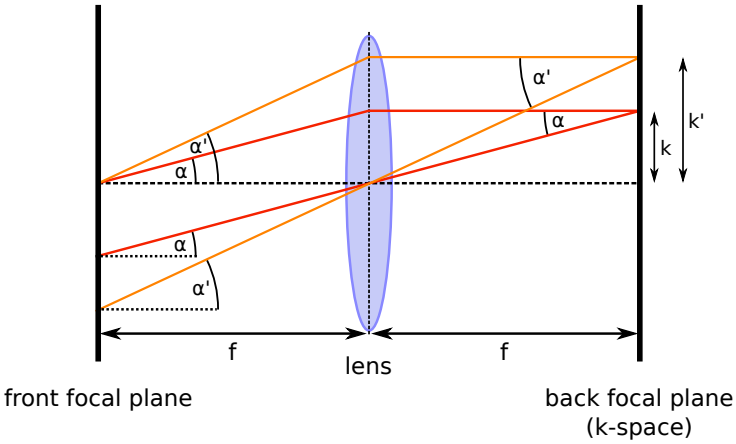

Figure 2.12: Optical Fourier transformation of thin lens with focal length f. Light beams with angles α and α' in the front focal plane are imaged onto spots at k and k' in the back focal plane, which is the k-space of the input light field. Adapted from Ref. [73].

whereby t_l is determined by l, the wavelength of the light beam λ, the focal length of the imaging lens f_{Imag} and the parameter $d = 2\pi a$, which equals the length of the unwrapped intensity stripe in the plane of the phase correction element. This linear shift can also be seen from the OAM sorted intensity profiles of different OAM states. Fig. 2.13 exemplarily compares the spatial profiles obtained by integrating the OAM sorted intensity images of different OAM states perpendicular to the axis of the deflection. The OAM sorting peaks of OAM states with different l are clearly distinguishable. This opens up the unique possibility to simultaneously detect multiple superposed OAM states. However, adjacent peaks of OAM states with $\Delta l = 1$ still overlap with each other significantly. This overlap is inevitable when using this OAM sorting transformation and may not be removed by only adjusting the parameters of the transform and correction phase pattern. Improved versions of such optical transformations have been demonstrated, which sharpen the OAM sorting peaks by interfering multiple copies of the OAM sorting beam [74, 75]. This is primarily useful to minimize the cross-talk in communication applications. However, in our case the basic OAM sorting setup is sufficient for detecting optical vortices. The additional phase elements for optimizing the cross talk would just increase the experimental effort without providing any benefit for our intended purpose.

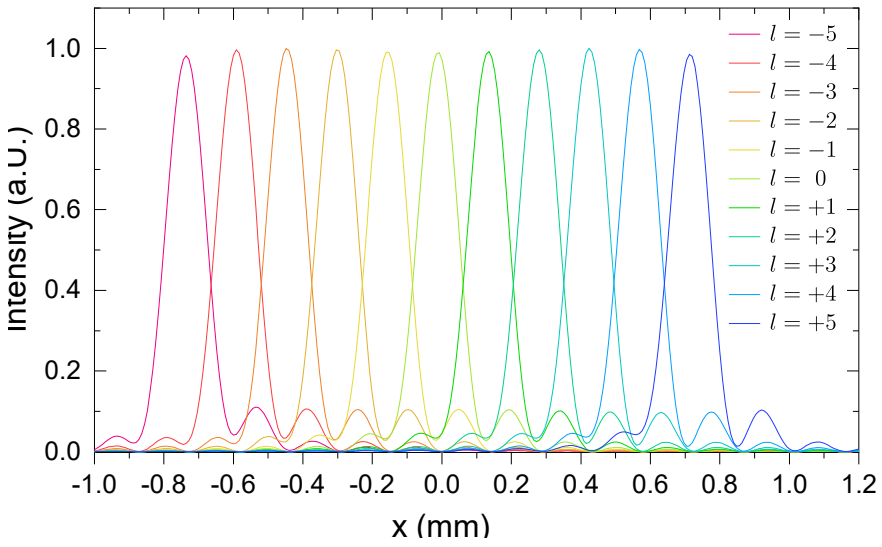

Figure 2.13: Spatially integrated profiles of simulated OAM output intensity images for OAM values $l = -5$ to $l = 5$. The peaks corresponding to the individual OAM states shift linearly with l and are clearly distinguishable, although adjacent peaks significantly overlap each other. The parameters for this simulation are $\lambda = 773\,\text{nm}$, $a = 0.004/2\pi$, $b = 0.00677$, $f_{\text{OAM}} = 0.1\,\text{m}$ and $f_{\text{Imag}} = 0.75\,\text{m}$. This set of parameters will also be used later on in chapter 4.2.1 when confirming the OAM axis of the experimental measurements.

2.5.1 Simulating the beam propagation of OAM Sorting

To understand and optimize the experimental implementation of the OAM sorting process, we use a simple beam propagation simulation of the OAM sorting setup including the phase elements given by Eqs. 2.49 and 2.50. The simulation model stores the light field as a two-dimensional complex matrix M. The intensity then is given by $I = |M|^2$ and the phase of the light field is given by the angle $\phi = arg(M)$ of the complex field in pointer representation. We implement a light field propagator which moves the light field in Fourier space and thereby simulates the beam propagation. The optical elements are modeled by real Matrices P_n, which reproduce the phase shift caused by the corresponding optical element. The light field is initialized with a real Gaussian beam profile, to which a vortex phase pattern is applied by multiplication of the complex field matrix with $\exp(iP)$. In the same way, all other optical elements such as the OAM sorting phase elements and lenses (modeled by a quadratic phase shift) are applied. By subsequent application of the optical element phases and propagation of the beam between the corresponding planes, we simulate the complete mapping of vortex modes with different OAM to spots in the output plane of a CCD camera. The sample code we use for this simulation is given in the appendix A.

Chapter 3

Measurements

This chapter presents the sequential measurements and steps towards controlling vortices in exciton polariton condensates. Hereby, we gradually develop the experimental setup, covering the steps of implementing the OAM sorting process, investigating exciton polariton vortices using the OAM sorting method and finally manipulating the polariton vortices by pulsed perturbation. First, section 3.1 presents the detailed implementation and benchmark of the OAM sorting method. In section 3.2 we apply this method to measure the OAM sorted signal of a microcavity sample. The details on the sample are given in this section. We perform time-resolved OAM measurements of the vortex modes forming inside a ringlike trap, which is created by ringlike non-resonant pump pulses. Hereby, we especially vary the ring diameter and excitation power. Finally, we extend the experimental setup and use a CW laser for creating the ringlike trap while the pulsed laser perturbs the vortex modes forming inside the trap.

3.1 Implementation of OAM sorting

The basic experimental setup is very similar for all measurements performed in this thesis and is mostly changed only regarding some details. We use the setup shown in Fig. 3.1 for benchmarking the OAM sorting process. First, an optical vortex with adjustable topological charge and rotation angle θ_d of the phase step is imprinted onto a CW laser beam. This beam then is guided through the OAM sorting setup and imaged onto a CCD camera. We vary the OAM states fed into the OAM sorting setup by specifically adjusting the OAM generation phase pattern on SLM 1 using a custom build Labview Vi. While doing so, we record the corresponding images of the OAM-sorted output intensity and extract the profiles by summation over all pixels along the y-axis. The results are presented in section 4.1. The OAM sorting setup as the core element of the experimental setup remains unchanged in all further measurements.

The CW laser is a tunable Ti:Sa based laser system, model SolsTiS 2000 PSX-XF manufactured by M Squared Lasers. It provides actively stabilized single-mode laser emission with up to 2 W optical output power and a very narrow linewidth of < 50 kHz.

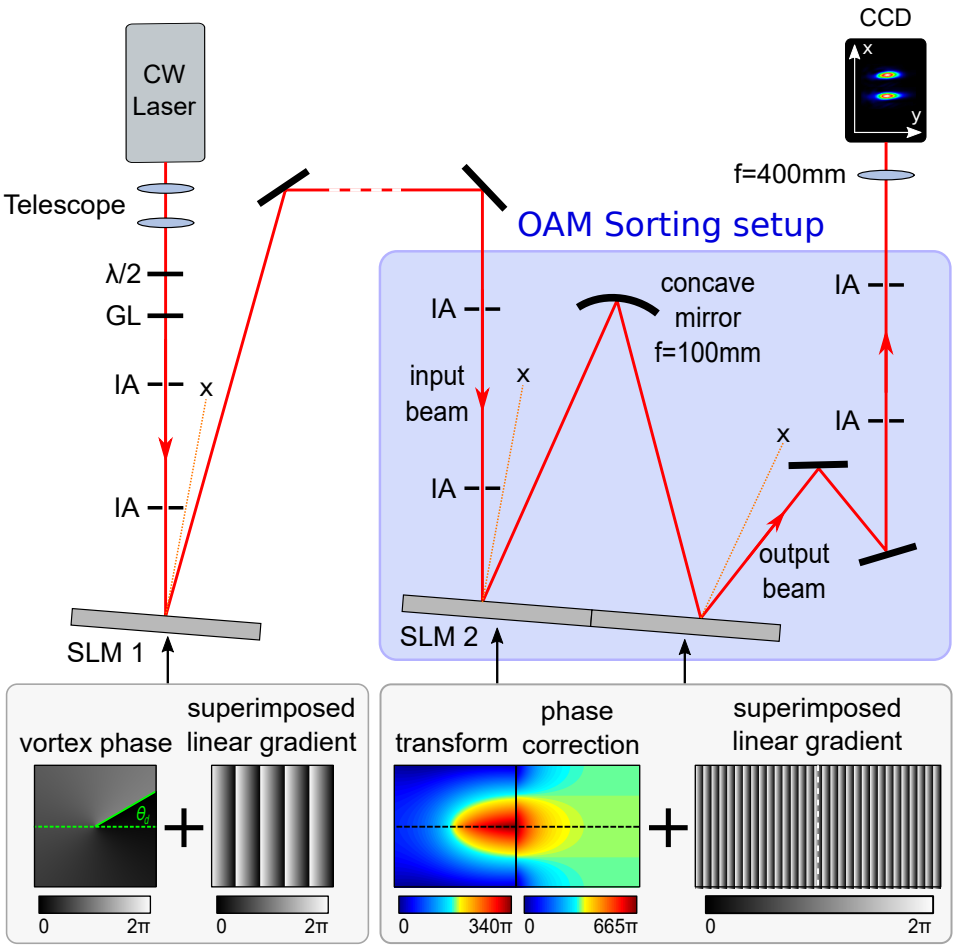

Figure 3.1: Sketch of the setup used for benchmarking the OAM sorting process including a detailed overview of the OAM sorting implementation and the phase pattern displayed by the SLMs. The divergent CW laser is collimated using a telescope, which consists of two $f = 100\,\mathrm{mm}$ lenses. The combination of a half wave plate ($\lambda/2$) and Glan-Thompson polarizer (GT) allows to reduce the CW laser power and set the polarization correctly for the SLMs. The beam is aligned using iris apertures (IA). Finally, a $f = 400\,\mathrm{mm}$ lens focuses the OAM-sorted beam onto a charge-coupled device camera (CCD), which is attached to a monochromator operated at 0th order (not depicted). SLM 1 displays an optical vortex, whereby the phase jump may be aligned at a rotation angle θ_d with respect to the symmetry axis of the OAM sorting phase elements displayed on SLM 2. All phase patterns are superposed with linear phase gradients to separate the first order of diffraction from the direct reflection on the SLM surface. The direct reflections (indicated by dashed orange lines) are blocked and thereby removed from the optical beam path.

The pump laser of this laser system is a 10 W Verdi CW laser by Coherent. The wavelength of the SolsTiS laser is tuned to $\lambda = 845\,\mathrm{nm}$ for the benchmark measurements.
The laser beam is shaped using SLMs of the model type PLUTO-2 from HOLOEYE. Each of them provides HD resolution of $1080\,\mathrm{x}\,1920$ pixels with $8.0\,\mu\mathrm{m}\,\mathrm{x}\,8{,}0\,\mu\mathrm{m}$ pixel size and a filling factor of 93 % [76]. The pixels are addressed with 8-bit resolution in the same manner as a computer monitor. Using the horizontal polarization axis of the SLM, every pixel locally shifts the phase of the incident light field from 0 to 2π according to its displayed pixel value. This renders it possible to imprint arbitrary phase patterns onto the incident light beam, such as an optical vortex or the OAM sorting phase pattern. The desired phase maps are rendered and displayed on both SLMs by using custom made Labview Vis, which allow for rapid adjustment of the parameters used for calculating the phase pattern. To separate the direct reflection from the sample surface and the modulated light beam, we always superimpose a linear phase grating to the desired phase pattern. Only the resulting first order of diffraction is kept in the optical beam path of the setup.
The OAM sorting setup includes two phase elements. Deviating from the theory sketch in Fig. 2.11, the experimental implementation is built in reflection geometry. The two phase patterns for transformation and phase correction are displayed on one single SLM with the symmetry axis of the phase elements being aligned horizontally, which leads to a vertical deflection of light beams with non-zero OAM. The OAM sorting lens is replaced by a concave mirror, which effectively transforms the light field in the same way like a lens would do. The parameters of the OAM sorting phase elements in the benchmark measurements using a wavelength of $\lambda = 845\,\mathrm{nm}$ are $a = (0.008\,\mathrm{m})/(2\pi)$, $b = 0.00477$ m and $f = 0.095\,\mathrm{m}$.

The device for detecting the light beam resulting from OAM sorting is a liquid nitrogen cooled CCD camera attached to an Acton SP-2500i f=500 mm monochromator. The CCD camera provides $1340\,\mathrm{x}\,400$ pixels with a pixel size of $20\,\mu\mathrm{m}\,\mathrm{x}\,20\,\mu\mathrm{m}$. For these measurements we open the slit of the monochromator and set the diffraction grating to image the 0th order of diffraction onto the CCD. For further measurements with spectral resolution, blazed gratings with 300, 600 and 1200 blazes are available.

3.2 Time-resolved OAM spectroscopy

The experimental setup is heavily extended to generate exciton polariton vortices and detect them using the OAM sorting setup. We use a pulsed excitation laser to enable time-resolved studies of potentially forming exciton polariton vortices. The full setup including all alternative experimental techniques for different measurements of the sample emission is shown in Fig. 3.2. We discuss its versatile use starting from the excitation side, moving on towards the sample and closing with the different possible measurements. The results of the measurements are presented in section 4.2.1.

The excitation laser is a tunable pulsed Ti:Sa laser system by Coherent. It may generate either picosecond or femtosecond pulses at a repetition rate of 75.4 MHz. In the configuration used for experiments in this thesis, it generates pulses with roughly 120 fs duration. The spectral peak of the pulses is adjusted to match the first Bragg minimum of the microcavity sample we use at $\lambda = 735.5\,\mathrm{nm}$. The pulsed laser beam is reduced in intensity and rotated to the horizontal polarization axis, for which the SLM performs efficient phase only modulation. The slightly elliptical beam profile is reshaped to a Gaussian beam profile by filtering the beam with a pinhole inside a telescope lens arrangement. Since the spectrum of the pulses is very broad, two short pass filters ensure that no pump laser light is present at the wavelength of the sample emission. The SLM imprints an axicon phase profile onto the excitation laser beam and separates the modulated light beam from the direct reflection, as discussed before regarding Fig. 3.1. The phase of an axicon consists of a rotationally symmetric gradient, which linearly decreases with the radius, as can be seen from the inset in Fig. 3.2. The locally incident light bundles are deflected from the optical axis and form a conical shape. The opening angle of this cone increases with the slope of the phase gradient similar to the deflection of a light beam in which a plain linear phase gradient is imprinted. Thereby a ring with adjustable diameter is created, when the beam with axicon phase is focused onto the sample.

The sample is a planar GaAs-based microcavity, grown by molecular beam epitaxy (MBE) at the University of Würzburg[1]. The quality factor of the sample is about $Q \approx 20000$ and the Rabi splitting is 9.5 meV. In detail, the sample consists of a $\lambda/2$-cavity with four quantum wells embedded in the central antinodes of the resonant cavity light field mode, which is confined by the surrounding DBRs. The DBR structure around the cavity layer consists of 32 top and 36 bottom layer pairs made of $Al_{0,2}Ga_{0,8}As/AlAs$. Furthermore the microcavity is slightly wedged, so that the cavity mode intentionally varies along a defined axis of the sample. In the experimental setup the sample is mounted in a helium-flow cryostat and cooled down to temperatures of 16-20 K. The whole flow cryostat may be moved perpendicular to the optical axis to change the exciton-cavity detuning by moving the sample with respect to the excitation laser beam. As the substrate is not polished, measurements with this sample need to be conducted in reflection geometry. This sample is specifically selected for the measurements presented in this thesis, since previous studies of it successfully demonstrated

[1] The identification number of the sample is M3396-9.2.

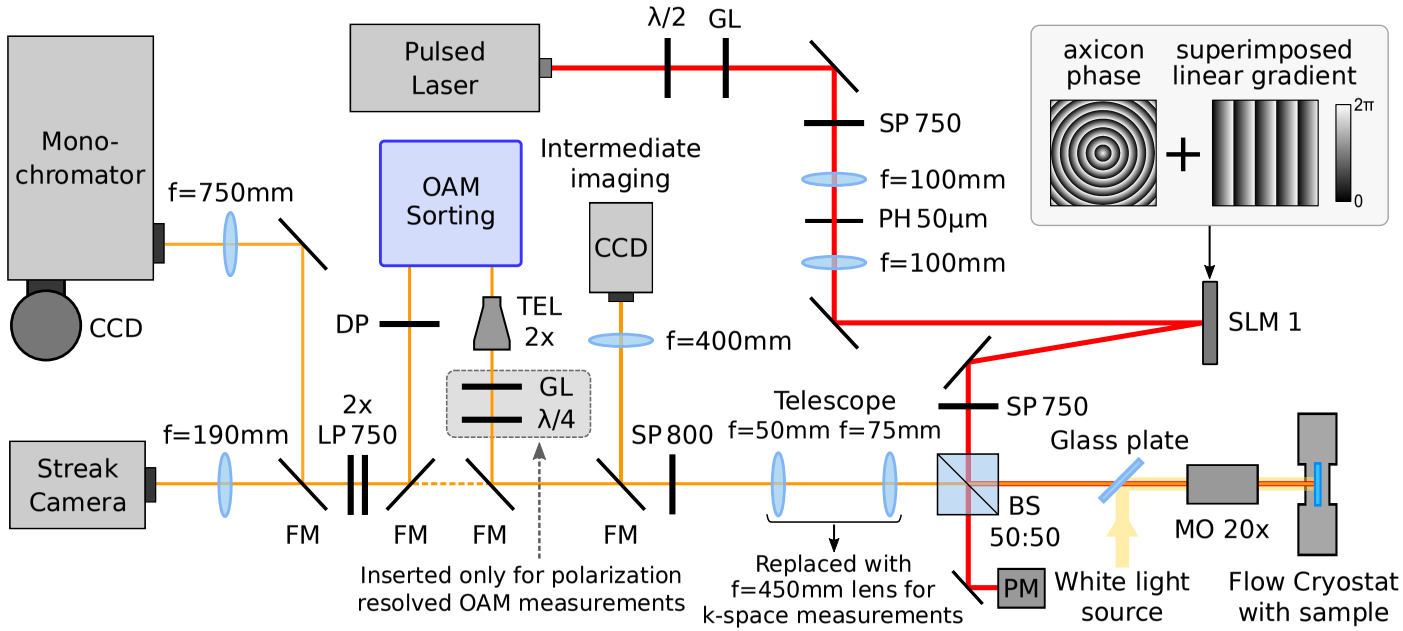

Figure 3.2: Detailed sketch of the experimental setup used for measurements of exciton polariton vortices. The pulsed laser is shaped to a ringlike beam profile and non-resonantly excites exciton polaritons. The sample emission may be detected with either the streak camera or the CCD camera attached to a monochromator, allowing different types of measurements, as described in the text. The OAM sorting part itself is identical to the setup shown in the blue box in Fig. 3.1. However, a telescope (TEL 2x) with a lens focus ratio of two is placed on the input beam axis to reduce the beam diameter of the sample emission. The other optical elements are halve and quarter wave plates ($\lambda/2$ and $\lambda/4$), Glan-Thompson polarizers (GT), flip mirrors (FM), an unpolarized beam splitter with an equal ratio of reflection and transmission (BS 50:50), a dove prism (DP) and short and long pass filters with the cutoff wavelengths of 750 nm and 800 nm (SP750,SP800,LP750). The excitation laser beam is focused onto the sample using a Mitutoyo near infrared microscope objective with 20x magnification and a numerical aperture of 0.4 (MO 20x). The sample focus may be adjusted by moving the cryostat while observing the white light reflection of the sample on the intermediate imaging CCD camera. The power of the excitation laser beam is measured with a power meter (PM).

exciton polariton condensation [42].
The emission of the sample might be imaged in various ways, as shown in Fig. 3.2. The OAM sorting setup is embedded in the total setup by using flip mirrors, which allow one to bypass it completely in case measurements without resolving the OAM are required. Also the sample signal may be guided either to the streak camera or to the monochromator. Moving the entrance slit of the monochromator aside and setting the spectrograph to 0th order allows one to acquire real space images of the sample emission and images of the OAM sorted sample signal spots. We do this for excitation with different ring diameters (determined by the slope of the axicon phase pattern) and pump powers. We also image the OAM sorted sample signal onto the streak camera and thereby obtain the time-resolved OAM sorted sample signal. In addition to this, a combination of a quarter wave plate and Glan-Thompson prism can be inserted into the input beam path of the OAM sorting setup to obtain time-resolved OAM measurements for both circular polarizations σ^- and σ^+. Furthermore, using the photon counting mode of the streak camera allows us to perform single shot measurements and extract correlations between different modes of the sample emission. The streak camera in our experimental setup is a custom-made camera by Hamamatsu. It features two microchannel plates and a fast synchroscan unit, which allows to detect signals with very weak intensities at a high temporal resolution of few picoseconds. The temporal resolution in the shortest time range of the streak camera is about 2-3 ps for the typical entrance slit aperture of 40 μm. Opening the entrance slit further or changing the operation mode to longer time ranges reduces the temporal resolution.
To realize time-resolved OAM measurements, the OAM sorted output signal needs to be rotated by 90 degree so that the horizontal slit of the streak camera records a cross-section of all OAM spots. We achieve this by a placing a fixed mounted dove prism in the output beam path of the OAM sorting setup. The slit of the streak camera is opened by 40 μm for time-resolved OAM measurements, which are acquired in the analog integration mode of the streak camera. In case of single photon counting measurements the slit is opened to 100 μm to increase the total signal power.
The excitation pump laser always creates a reflection on the sample surface, which spatially overlaps with the sample signal and exceeds the intensity of the emission by several orders of magnitude. We use this reflex for general adjustment of all optical elements in the detection beam path and specifically to adjust the telescopes and the OAM sorting setup. During measurements, the reflection of the pump laser is removed by two consecutive long pass filters with a cutoff wavelength of 750 nm, so that only the sample emission is detected. The diameter of the sample signal beam needs to be reduced so that no clipping at the phase elements displayed on the SLM occurs. A combination of a telescope on the main beam axis with a lens focus ratio of 1.5 and a second telescope close to the SLM with a lens focus ratio of two was found suitable for this task. When using only a telescope close to the SLM on the input beam axis of the OAM sorting setup, the diameter of the beam is already too large to reduce it with a compact telescope arrangement without clipping at the telescope itself or causing strong aberrations. When performing Fourier imaging of the sample signal, the telescope on the main beam axis is removed and replaced by a Fourier lens, which

centrally images the Fourier plane of the sample emission onto the entrance slit of the monochromator. Thereby we record the energy dispersion of the exciton polaritons.

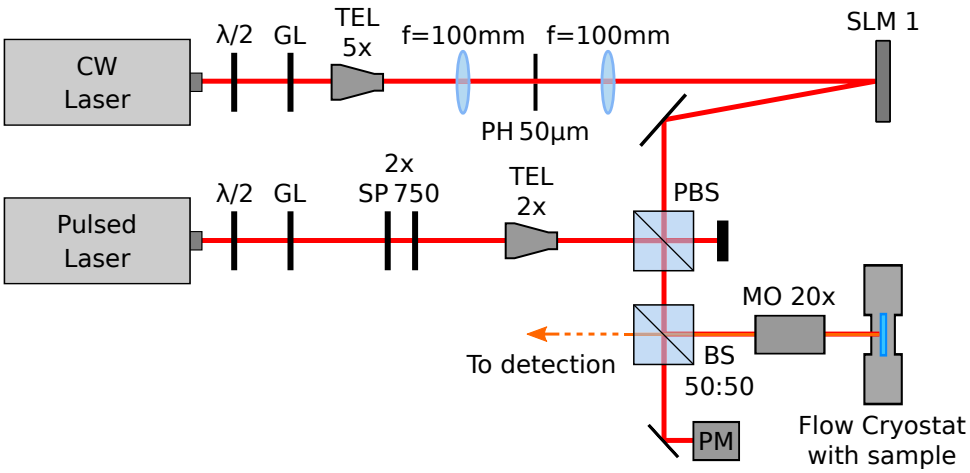

Figure 3.3: Extension of the experimental setup with two lasers to investigate the control of exciton polariton vortices. The CW laser is shaped to a ringlike beam profile and used for vortex creation. The pulsed laser has a Gaussian beam profile and is used to perturb the vortices forming inside the induced ringlike trap. Both beams are combined using a polarizing beam splitter (PBS). The detection part of the setup and notation of the optical components are identical to Fig. 3.2. The CW laser beam fans out strongly when propagating the distance of around three meters towards the SLM, due to its significant beam divergence. Thus, a telescope with a greater lens focus ratio of five (TEL 5x) is used to collimate the CW laser beam and reduce its beam diameter. The final diameter of the beam incident onto SLM is about 2 mm.

Given all these options, the experimental setup shown in Fig. 3.2 allows us to create and thoroughly investigate exciton polariton vortices forming by non-resonant ringlike excitation. The results of the measurements are shown and discussed in section 4.2.1. To go one step further and investigate the control of polariton vortices, the setup is extended even further to use two excitation lasers, as shown in Fig. 3.3. Now, the CW laser is shaped to a ringlike beam profile and tuned to the same peak wavelength as the non-resonant pulsed excitation laser. In this case, the pulsed laser with Gaussian beam profile is used to perturb the vortices which are forming inside the CW ring trap. We measure the time-resolved OAM profiles for different excitation powers. The results are discussed in section 4.3.

Chapter 4

Results

The results presented in each of the following sections represent subsequent steps of implementing OAM sorting and applying it to exciton polariton vortices. In the first step, we implement OAM sorting as the core element of the experimental setup and investigate its applicability with respect to the unambiguous identification of individual OAM modes in a semiconductor spectroscopy setting. In the second step, we use this OAM spectroscopy method to confirm the spontaneous formation of polariton vortices induced by non-resonant optical pumping and study the vortex formation process in more detail. In the last step, the focus of research moves from the pure observation of polariton vortices towards their controlled manipulation.

4.1 Benchmark of the OAM sorting process

With the goal set to measure the OAM states of vortices formed in exciton polariton condensates, the first step towards doing so is the verification of the experimental implementation of OAM sorting. We implement the practical OAM sorting setup in a customized reflection geometry using one single SLM as described in chapter 3.1. The OAM is imprinted onto the laser beam using another SLM. The laser beam is guided towards the aligned OAM sorting setup. We capture the OAM-sorted signal with a CCD camera and extract the intensity profiles along the axis of deflection. The resulting peaks are displaced linearly with OAM, as can be seen in Fig. 4.1(a). Based on the parameters of the experimental implementation, we use the beam propagation simulation described in section 2.5.1 to reproduce this OAM sorting process. The simulated intensity profiles are shown in Fig. 4.1(b). The measured and simulated profiles match each other closely and show good agreement of the spot positions. However, the peak intensity and width of each experimentally observed spot deviate slightly from those of the corresponding spot in the simulation. The non-uniform variation of the peak intensities can be attributed to a non-perfect alignment of the position and incidence angle of the spatially extended light beams on the surface of the SLM. Due to the limited size of the SLM, parts of the light field may be cut off. The higher width of the peaks in experiment compared to the simulation may be attributed to a cut-off

of components with high spatial frequency in Fourier space at the plane of the phase correction element. Still, the measurements show that the implementation of OAM sorting is working and enables us to perform further studies.

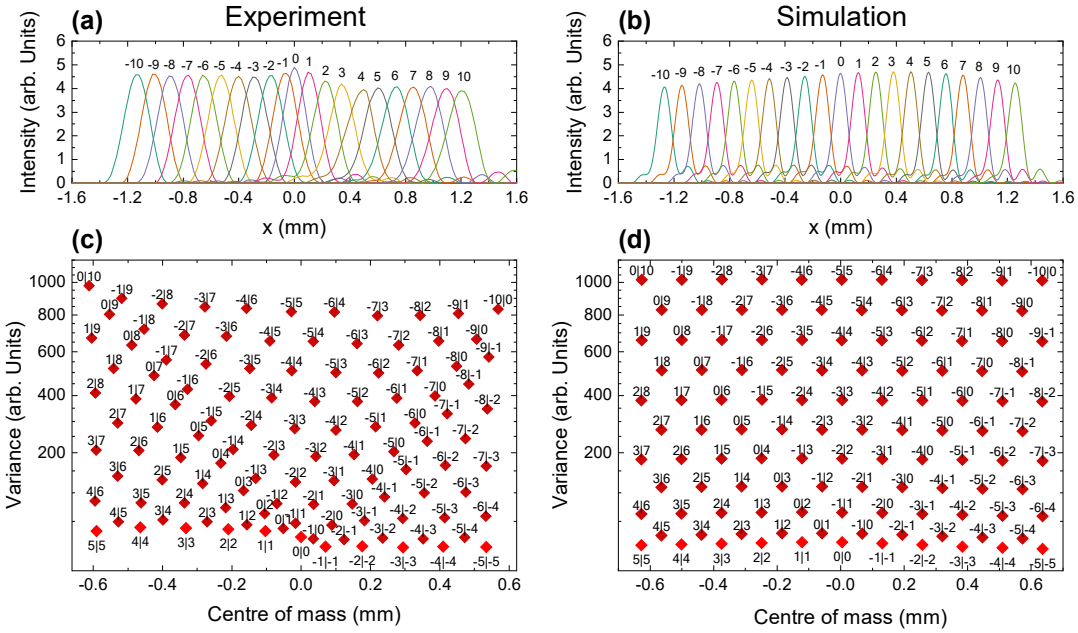

Figure 4.1: Experimentally measured (a) and simulated (b) spatial profiles of OAM sorted pure OAM states. Based on this, the center of mass and variance of incoherent superpositions of two integer OAM states with equal weight are calculated and plotted for experiment (c) and simulation (d). The resulting two dimensional pattern allows to clearly identify the integer OAM states composing a superposition. Red diamonds mark the data pairs of center of mass and variance, while the adjacent numbers indicate the constituent OAM states. Bright red diamonds are used to indicate superpositions of two OAM states with identical OAM.

The typical approach following Berkhout et al. [21] for evaluating the OAM sorted intensity as the output of the OAM sorting process consists of binning the profiles, whereby the separate bins correspond to the individual OAM states. Thereby a mapping of integer input states to integer output states is performed. However, in the context of obtaining the continuous spectrum of OAM states of an a priori unknown sample signal, the strict binning into integer values is not necessarily a useful approach anymore. Therefore a different approach for analyzing the continuous spectra needs to be applied. Here, we evaluate the output intensity profiles using the moments of the intensity distribution, such as its center of mass x_{cms} and variance V, which are calculated according to

$$x_{cms} = \sum_i x_i \cdot I(x_i), \tag{4.1}$$

$$V = \sum_i (x_i - x_{cms})^2 \cdot I(x_i), \tag{4.2}$$

where i runs over all pixels, x_i denotes the vertical position of pixel i and $I(x_i)$ represents the intensity at pixel i.
The center of mass x_{cms} provides a measure for the average OAM of the output signal, while the variance gives a measure for the width of the sorted output intensity profiles on the OAM scale. Using these moments, a mapping of all pure integer OAM input states and incoherent superpositions of two pure integer OAM input states onto unique spots in a graph (shown in 4.1(c) and (d) for experiment and simulation) becomes possible and thereby allows the unambiguous identification of the input integer OAM states only from the values of x_{cms} and V. The moments x_{cms} and V generate a two dimensional space, which renders it possible to identify two superposed integer OAM states uniquely. This concept may also be extended using higher order moments (for example skewness and kurtosis), in case a definite identification of more possible inputs states is required. However, this is not required when applying OAM sorting as a spectroscopic method since the focus of interest is to provide a qualitative measure of the overall output OAM signal of an unknown source without making any assumptions about the signal. Thereby, the two moments presented in 4.1 and 4.2 are sufficient in this context.
When considering completely unknown sample signals with arbitrary OAM states, even the restriction to OAM states with integer topological charges only constitutes an a priori assumption. Since we are not necessarily allowed to make this assumption, this raises the intriguing question how non-integer OAM states are mapped in the OAM sorting process. To investigate this question, we experimentally implement and also simulate the mapping of fractional OAM states with non-integer topological charges.
Fractional OAM states correspond to inserting a non-integer l in the term $2\pi l$, describing the phase winding of an optical vortex. This implies a phase discontinuity at a certain rotation angle θ_d (as depicted in Fig. 3.1), where the phase jump is not an integer multiple of 2π anymore. As a consequence, the rotational symmetry is broken. Taking into account that the OAM sorting phase patterns are not rotationally symmetric and have a specific mirror symmetry axis, the result of the OAM sorting process may vary depending on the rotation angle with respect to this axis. In Fig. 4.2, the output intensity pattern for fractional OAM states with different rotation angles are shown both for experimental and simulated data. For $\theta_d = 0°$ the fractional OAM states are imaged onto single spots, moving linearly with topological charge between the two nearest integer OAM states. For $\theta_d \neq 0°$, the OAM sorted peaks split into double peaks with different intensities, offset from the peak positions of the integer OAM states. At $\theta_d = 180°$, the splitting becomes symmetric with respect to the half-integer values at the central positions between the neighboring integer OAM states. This behavior can be understood considering how the phase gradient is unwrapped by the OAM sorting

setup, as already shown in Fig. 2.11. For $\theta_d = 0°$, the OAM sorting setup unwraps the phase gradient of fractional OAM states exactly along the phase discontinuity and transforms the phase of the light field into a continuous linear phase gradient just like in the case of an integer OAM state. On the contrary, for $\theta_d \neq 0°$ the phase gradient is unwrapped along a different axis. The phase gradient of the unwrapped light field then splits into two linear parts, separated by the phase discontinuity maintained in the OAM sorting transformation process. The result is a splitting of the OAM-sorted signal into two peaks.

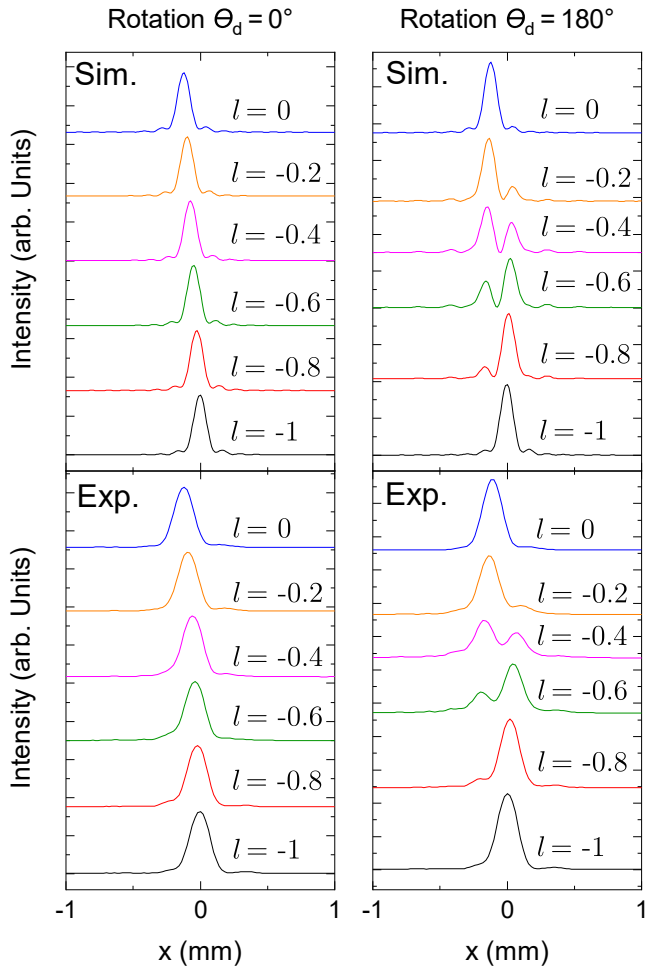

Figure 4.2: OAM sorted intensity profiles of fractional OAM states from $l = -1$ to $l = 0$ for experiment and simulations with rotation angles of $\theta_d = 0°$ and $\theta_d = 180°$. The profiles contain a single peak at $\theta_d = 0°$, whereas a splitting of this peak is observed at $\theta_d = 180°$.

For a more detailed picture, we calculate the center of mass and sorted variance of the OAM sorted intensity profiles for a broader range of fractional OAM and at different rotation angles θ_d. We compare our results to the results presented by Alperin et al. [67] with a focus on the relation between the intrinsic, extrinsic and total OAM. The intrinsic OAM component is invariant under rotations around the axis of propagation, hence any rotation angle θ_d will result in the same OAM sorted intensity distribution. It directly corresponds to the topological charge of the phase function used to generate the light beam with OAM and amounts exactly to l. Still, the total OAM may differ from this value, since it also includes the extrinsic OAM component, which is equivalent to a net linear transverse momentum of the light beam. The extrinsic OAM component is usually associated with a shift of the center of gravity of the light beam, caused by an asymmetrical obstruction of the light beam [63]. For light beams with non-zero extrinsic OAM components, the output intensity distribution of the OAM sorting process depends strongly on the relative rotation of the beam with respect to the phase elements of the OAM sorting setup. In contrast to this, the extrinsic OAM components vanish for OAM states with integer OAM and the total OAM then equals the rotation invariant intrinsic OAM. In general fractional OAM states with non-integer l provide non-zero extrinsic OAM components and thereby the total OAM differs from the intrinsic one. In this context, the discontinuous phase step of fractional OAM states can be understood as the origin of non-propagating evanescent waves, which are effectively equivalent to a partial obstruction of the light beam [67].
The results for the center of mass and sorted variance of fractional OAM states in a wide range of l and for two particular rotation angles θ_d are shown in Fig. 4.3. Hereby, the simulated center of mass positions perfectly match the expected linear dependence for intrinsic OAM and modified dependence with a sine function for the mean or total OAM, as predicted by Eq. 2.48 in chapter 2.4. Also the movement of the center of mass corresponding to average OAM is in good agreement with the fractional OAM measurements from Alperin et al. [67], where a cylindrical lens is used for transforming the light beam and the average OAM is extracted from the output light field. At the rotation angle $\theta_d = 0°$, the shift of the center of mass with topological charge closely resembles a straight line. Hence, the extrinsic OAM components are zero and only intrinsic OAM is measured at this rotation angle. For all other rotation angles, oscillations of the center of mass appear. Exactly at the rotation angle $\theta_d = 180°$, the nodes of the oscillation are located at the integer and half-integer values of the topological charge l, resembling the measurement of total OAM by Alperin et al. [67]. So in this case, the total OAM is measured. The agreement between the simulated center of mass positions and Eq. 2.48 also confirms this.
In practical applications, it might be of interest to distinguish between integer and non-integer OAM states. As seen in Fig. 4.3, this may be achieved easily by measuring the average OAM corresponding to the center of mass for the two rotation angles $\theta_d = 0°$ and $\theta_d = 180°$. However, this is not valid for half-integer fractional OAM states, as the internal OAM and total OAM are equal for these states. In this case, also the sorted variance needs to be taken into account, whose values differ significantly for half-integer fractional OAM states. The strong oscillations of the sorted variance of the fractional

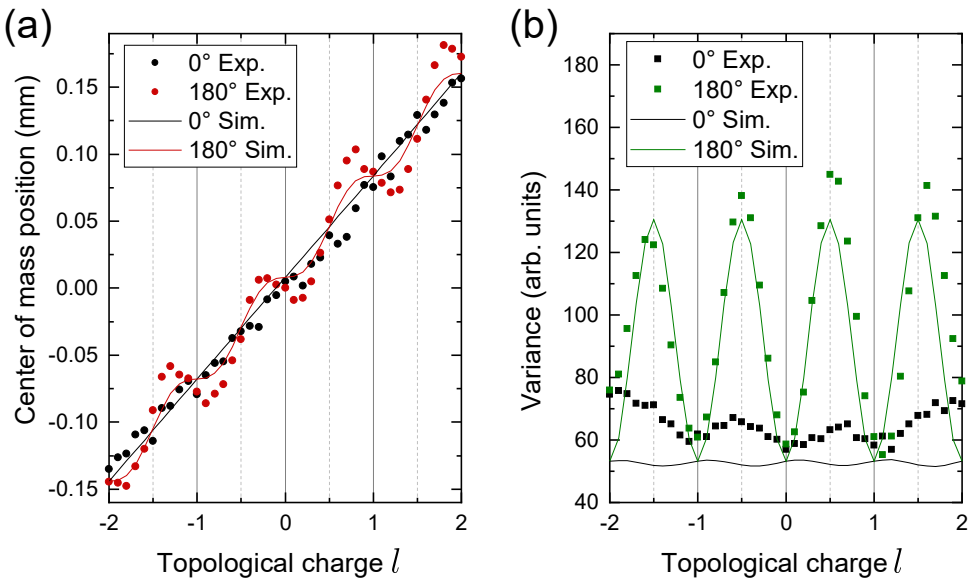

Figure 4.3: The center of mass (a) and sorted variance (b) are extracted from the OAM sorted intensity profiles of fractional OAM states with $l \in [-2,2]$ for the rotation angles $\theta_d = 0°$ and $\theta_d = 180°$, which correspond to the measurement of intrinsic and total angular momentum. Both in experiment and simulation at $\theta_d = 180°$ oscillations of the center of mass occur. Also the variance of fractional OAM states strongly differs between the $\theta_d = 180°$ and $\theta_d = 180°$ rotations.

OAM states result from the peak splitting already seen in Fig. 4.2. It should be noted, that the experimentally observed oscillations in Fig. 4.3 are more pronounced than predicted by the simulation, which is quite surprising. This observation may also be explained by the clipping of spatial high frequency components in the Fourier plane at the phase correction pattern, as discussed before concerning the broadening of the experimentally observed OAM sorted peaks.

As a side note it should be mentioned, that light beams with fractional OAM are not stable and decay into many (stable) vortices with $|m| = 1$ upon propagation. Especially near the phase discontinuity a vortex chain with lowered intensity forms [65]. The number of vortices along this chain rises with propagation distance and is expected to be quite high for the long propagation distance of about 3 m in our experiment. Despite this, the OAM sorting method still detects the correct OAM value according to the topological charge set by the vortex generation phase pattern. The vortex chain does not seem to have a significant impact onto the OAM sorted intensity peaks. We explain this with the fact that the intensity of the light field along the vortex chain is low. Thus, this beam part gives only an insignificant contribution to the total intensity of the light beam.

While imprinting a fractional vortex results in non-integer OAM, the other way around

a non-integer OAM value does not necessarily imply the presence of a fractional vortex. In general a light field may have non-integer average OAM, which is not necessarily the result of imprinting a fractional vortex. For example an incoherent superposition of different integer OAM states may have the same average non-integer OAM as a fractional OAM state. In this example we compare the detection of fractional OAM states and incoherent superpositions of integer OAM states with equal average non-integer OAM. We calculate the sorted variance of incoherent superpositions, comprising the $l = -1$ and $l = 0$ OAM states with weights chosen to generate a set of states with average OAM values between -1 and 0 in equidistant steps. The resulting sorted variance for these incoherent superpositions is plotted alongside with the sorted variance of the fractional OAM states with equal average OAM in Fig. 4.4. While the sorted variances of the fractional OAM states strongly differ for different relative orientations between the light beam and the phase elements of the OAM sorting setup, this is not the case for incoherent superpositions. The reason for this is the different rotational symmetry of the input states. A superposition of integer OAM states maintains the rotational symmetry of the comprising states, whereas fractional OAM states show a broken rotational symmetry due to the phase discontinuity. Thus, changing the relative orientation between the OAM sorting phase element and the input light beam yields the opportunity to experimentally distinguish true fractional OAM states and mixed OAM states formed by superpositions of integer OAM states.

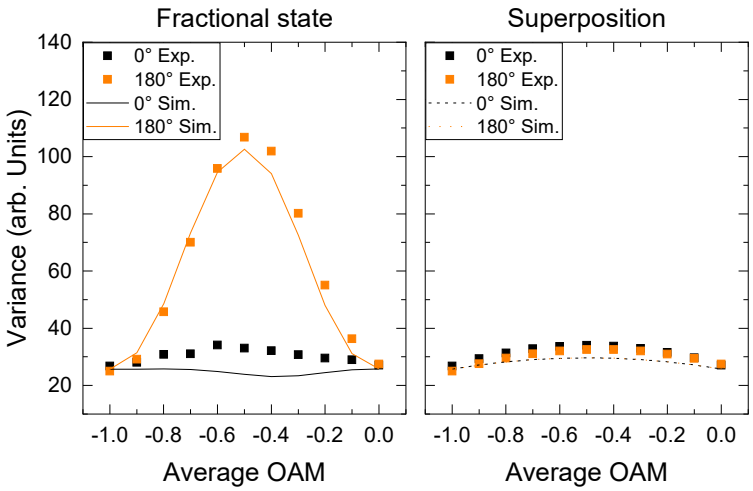

Figure 4.4: The sorted variance of fractional OAM states and incoherent superpositions of the integer OAM states -1 and $l = 0$ are juxtaposed. The weights of the integer OAM states in the incoherent superposition are chosen such that the average OAM matches the fractional OAM values. Only the sorted variance of fractional OAM states shows a dependence on the relative beam rotation angle θ_d.

To conclude this section, when imaging fractional OAM states using the OAM sorting setup, we can choose whether to measure the internal OAM or the total OAM by specif-

ically setting the relative orientation between the phase discontinuity of the fractional OAM states and the symmetry axis of the OAM sorting phase elements. By performing measurements with both rotation angles $\theta_d = 0°$ and $\theta_d = 180°$, fractional OAM states and pure integer OAM states, including superpositions may be distinguished by evaluating the center of mass and sorted variance of the OAM sorted intensity distribution. Thus, the OAM sorting method may be applied to perform spectroscopy of the OAM states, emitted by an arbitrary source. In the next section, we present the results of its practical application to exciton polariton vortices.

4.2 Investigation of spontaneously created exciton polariton vortices

After having verified the implementation of the OAM sorting process in the experimental setup, the following section demonstrates the generation of exciton polariton vortices and investigates their formation process. All measurements in this section have been performed using the same basic setup using a pulsed non-resonant pumping laser shaped to ringlike spatial beam profiles. First, we confirm the occurrence of spontaneously formed vortices using the OAM spectroscopy method. Second, we investigate the temporal dynamics of the formation process and model this process theoretically. Finally, we experimentally investigate the different polariton spin components corresponding to left and right circular polarization.

4.2.1 Generation and detection of polariton vortices

Exciton polariton vortices may be created in various ways, as already discussed in chapter 2.3. Here, we utilize an annular non-resonant pump beam to create a ringlike potential trap, in which vortices may form spontaneously [18]. First, we confirm the formation of vortices inside the ringlike trap. Then we study further properties of the arising modes.
The results shown in Fig. 4.5 provide evidence for the creation of vortices. Fig. 4.5(a) shows the real space emission of the sample when using Gaussian and ringlike excitation beams below and above the condensation threshold. The evaluation of OAM sorted profiles including simulation results is shown in 4.5(c). In Fig. 4.5(b) the exciton polariton dispersion captured with a Gaussian excitation beam below threshold is shown for reference. The exciton-cavity detuning is $-4\,\mathrm{meV}$ in all measurements.
The procedure for this measurement is as follows: The excitation beam is not shaped at first, leading to a Gaussian excitation beam being focused onto the sample. Above the condensation threshold a spatially narrow polariton condensate forms at the excitation spot. The emission is collected, transformed using the OAM sorting setup and imaged onto the CCD camera of the monochromator. The resulting spot represents the reference for a centered state with zero OAM. Then, the excitation beam is changed to a ringlike beam by altering the phase pattern displayed on the SLM to an axicon phase pattern. The ring diameter and excitation power are increased until the real space emission inside the trap shows the typical ringlike pattern of a vortex with a central core, where the intensity is almost zero. This real space pattern already gives a hint that vortices may be formed. To prove this, we use the OAM sorting setup to image the sample emission. Cross sections of the OAM sorted output images are shown in the upper half of Fig. 4.5(c). The profiles indicate that two vortices with opposite non-zero OAM form. To confirm the absolute values of OAM carried by these states, we simulate the complete OAM sorting process using the exact same OAM sorting parameters and focal lengths of the lenses, as used in the experimental setup. The profiles of the thereby simulated OAM sorting peaks of $l = -1$, $l = 0$ and $l = 1$ OAM states are plotted alongside the measured profiles on the same physical axis, as shown

in the lower half of 4.5(c). The simulated peak positions match almost perfectly with the peaks in the measured OAM profiles, whereby we emphasize that the axis of the simulated data has not been rescaled to match with the experiment. The physical size of the axis is a pure result of the simulation including the exact parameters of the practical implementation of the OAM sorting setup. This conclusively proves that inside the annular trap indeed vortices form and that their topological charges are $m = -1$ and $m = +1$.

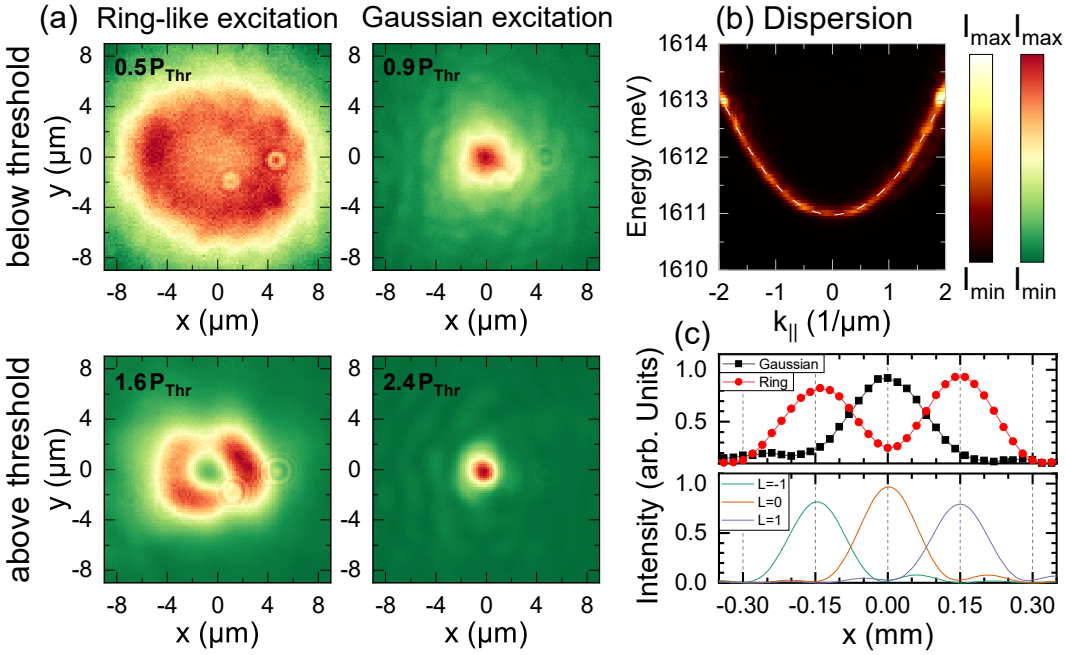

Figure 4.5: a) Experimental real space images recorded with either ring-like or Gaussian excitation, both below and above the condensation threshold. The excitation ring diameter is about 9 μm. (b) Exciton polariton dispersion at the chosen sample detuning of -4 meV recorded below the condensation threshold with a Gaussian excitation beam. The white dashed line represents a theory fit of the dispersion. (c) Cross-sections of the experimental OAM sorting output for both Gaussian and ringlike excitation (upper half) and simulated OAM sorting profiles of reference OAM states with $l = -1$, $l = 0$ and $l = 1$ (lower half). The intensities of the experimental profiles are normalized to match the scale of the simulation. The scaling of the x-axis is exactly the same for experiment and simulation.

This finding all by itself is not very surprising, since the spontaneous formation of vortices has been observed before, as already discussed in 2.3. However, the OAM spectroscopy approach followed here enables us to perform more advanced measurements to gain insights into the vortex formation process. Since the excitation laser is pulsed, the occurrence of the OAM modes can be easily traced in time by imaging the OAM sorted sample emission with a streak camera instead of just a CCD camera. Two exemplary results of such measurements for different excitation powers along with the

corresponding measurements of the dispersion are shown in Fig. 4.6.

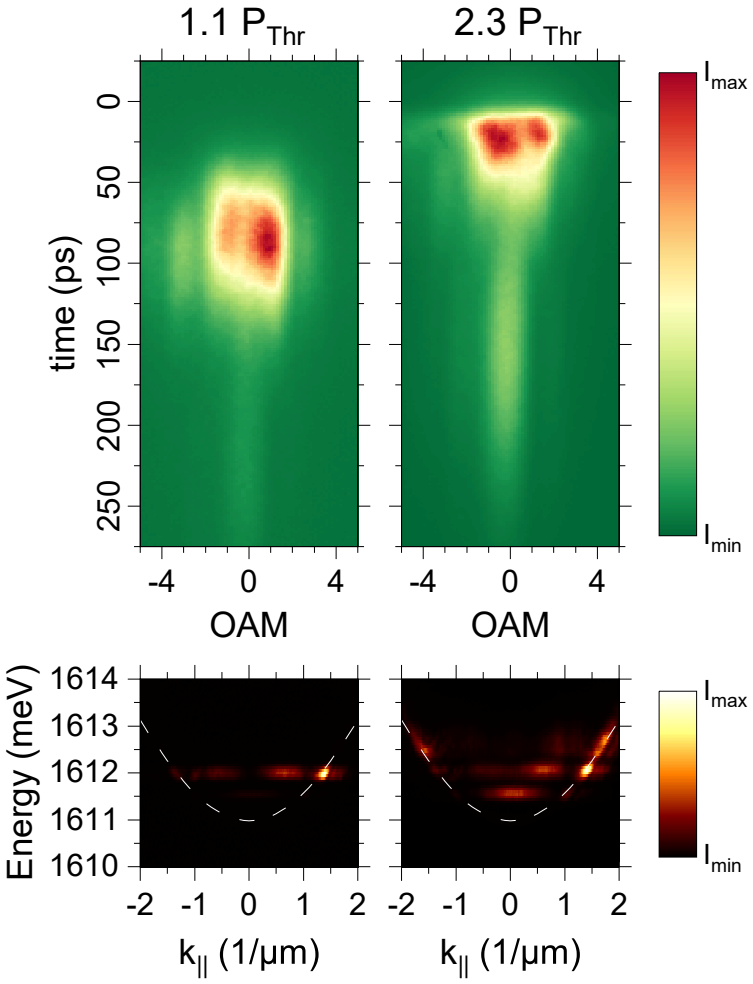

Figure 4.6: Time-resolved OAM measurements for different excitation powers together with the related k-space images below ($1.1\,P_{Thr}$ left, $2.3\,P_{Thr}$ right). At first non-zero OAM modes with $m = -1$ and $m = +1$ form at the same time, followed by a longer lasting zero OAM mode. The intensity of the zero OAM mode varies with excitation power, allowing the identification of the lower energy zero OAM mode and higher energy non-zero OAM modes in k-space. The white line is the same as in Fig. 4.5. It represents the polariton dispersion at low polariton densities below condensation threshold, with respect to which all arising OAM modes are blue-shifted. The excitation ring diameter is $9\,\mu$m.

We find the time dynamics of the arising modes to be dependent on the excitation power, as can be seen from the time-resolved OAM profiles. Two vortex modes with $m = \pm 1$ arise at the same time. In addition to this, also a third mode with zero OAM and longer lifetime exists. Due to its lower intensity, it does not show up as a distinct peak in the profile, shown in Fig. 4.5(c). However, in time resolved measurements it

emerges with an intensity depending on the excitation power. The relative intensity of the zero OAM mode compared to the non-zero OAM modes rises significantly with increasing excitation power. Taking this rise into account allows one to identify the zero and non-zero OAM modes in the energy-resolved k-space measurements. The zero OAM mode arises at $k = 0$ at an energy level, which is blue shifted compared to the polariton dispersion recorded below the condensation threshold. The non-zero OAM modes arise at finite positive and negative k at a higher energy level above the zero OAM mode.
The coincident appearance of the OAM peaks relating to the $m = +1$ and $m = -1$ vortices raises the question whether these vortices of opposite topological charges may coexist with each other or if only either of them can exist at the same time. Also the origin of the zero OAM mode is unknown. The results shown in Fig. 4.5 provide no insight regarding this question, since the images are integrated over more than 10^6 single pulse excitations. To gain access to the formation dynamics of the different OAM modes at the level of individual single pulse events, more advanced correlation measurements are performed. For this, we change the operation mode of the streak camera to single shot photon counting and tune the excitation ring diameter and excitation power to values, where the zero OAM mode is well visible and the peaks of the OAM states are more distinct. A typical real space image and time resolved OAM image for this excitation with a 7-μm pump ring at $3.2\,\mathrm{P_{Thr}}$ is shown in Fig. 4.7. We segment

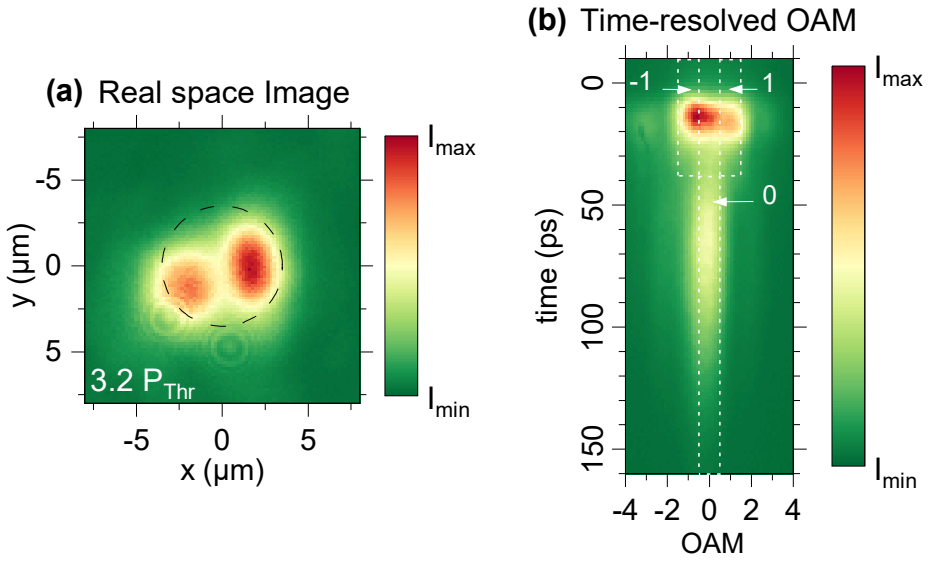

Figure 4.7: (a) Real space image of the sample emission well above condensation threshold for 7-μm diameter ringlike pump, indicated by the black dashed circle. (b) Example of a time-resolved OAM measurement signal recorded with an excitation ring diameter of 7 μm. The excitation power is also $3.2\,\mathrm{P_{Thr}}$ in this case. The white boxes indicate the areas used for counting the photons in the correlation measurements.

the OAM sorted signal into three areas corresponding to the arising OAM states and calculate the correlations between the photons detected in these areas as follows:

$$\mathrm{C}_{n,m} = \frac{\langle I_n I_m \rangle}{\langle I_n \rangle \langle I_m \rangle}, \tag{4.3}$$

$$\mathrm{A}_n = \frac{\langle I_n (I_n - 1) \rangle}{\langle I_n \rangle \langle I_n \rangle}. \tag{4.4}$$

Here, $\mathrm{C}_{n,m}$ is the cross-correlation, A_n is the autocorrelation, and n,$m \in \{-1,0,+1\}$ are indices for the OAM states. I_n and I_m are the respective photon counts recorded for the individual OAM modes. For a value $0 \leq \mathrm{C} < 1$ for a selected pair of modes, the modes show a tendency to suppress each other. In this case, they are not coexisting. However, for values $\mathrm{C} \approx 1$, the modes may coexist and for $\mathrm{C} > 1$ even show the tendency to appear in a correlated manner while coexisting. Besides, we also evaluate the autocorrelation of all detected photons related to the individual OAM states, which provides a measure for the photon number noise of each OAM mode.
The resulting cross-correlation of the -1 and $+1$ OAM modes is $\mathrm{C}_{-1,+1} = 1.08 \pm 0.09$, whereas the autocorrelation values of the individual modes are $\mathrm{A}_{-1} = 1.15 \pm 0.09$ and $\mathrm{A}_{+1} = 1.2 \pm 0.1$. The cross-correlation value fulfills $\mathrm{C} \approx 1$, which means that the arising -1 and $+1$ OAM modes are statistically independent of each other, i.e. they indeed may coexist with each other. Also the fact that the cross-correlation value and autocorrelation values do not differ significantly, suggests a common source of noise for both OAM modes. Further analysis of the other cross-correlations $\mathrm{C}_{-1,0} = 1.05 \pm 0.06$ and $\mathrm{C}_{+1,0} = 1.23 \pm 0.07$ shows that also the zero OAM mode is statistically independent of both non-zero OAM modes. In addition to the energy gap between the zero OAM mode and non-zero OAM modes, this result likewise suggests that the longer living zero OAM mode is formed in a different process, not directly related to the formation of the non-zero OAM modes.
To conclude this section: The spontaneous generation of vortices has been demonstrated. With ringlike excitation we find and investigate in total three different modes with -1,$+1$ and zero OAM. The non-zero OAM modes and zero OAM mode arise at different energies. A detailed analysis shows that the vortices with $m = -1$ and $m = +1$ and the zero OAM mode are statistically independent of each other and may coexist with each other. Furthermore, the time evolution of the signal changes with excitation power and ring diameter, as seen in Figs. 4.6 and 4.7. We investigate these temporal dynamics in more detail in the next section.

4.2.2 Temporal dynamics of polariton vortices

The temporal dynamics of the OAM modes forming inside a ringlike excitation potential shows a strong power dependence, as we have seen in the last chapter. The arising OAM modes and their time dynamics can be reproduced by the theory model according to Refs. [19, 20], which we present in the following. All simulated theory data of polariton condensates shown in this thesis result from the collaboration with our partners in the TRR142 project Xuekai Ma, Rodislav Driben and Stefan Schumacher from the university of Paderborn.
The dynamics of a condensate at the ground state of a quantum mechanical many body system may be described using the Gross-Pitaevskii-Equation, as we already discussed in section 2.1.4. However, unlike atomic gases, exciton polaritons are particles with finite lifetimes and are generated by an optical pumping process, which leads to the formation of a coherent quasi-equilibrium condensate in a non-trivial manner. Taking this process into account, the dynamics of an exciton polariton condensate may be modeled and simulated using the following mean-field open-dissipative Gross-Pitaevskii equation [77]:

$$\begin{aligned} i\hbar\frac{\partial\Psi(\mathbf{r},t)}{\partial t} = \Bigg[& -\frac{\hbar^2}{2m_{\text{eff}}}\nabla_\perp^2 - i\hbar\frac{\gamma_\text{c}}{2} + g_\text{c}|\Psi(\mathbf{r},t)|^2 \\ & + \left(g_\text{r} + i\hbar\frac{R}{2}\right) n_\text{A}(\mathbf{r},t) + g_\text{r} n_\text{I}(\mathbf{r},t)\Bigg]\Psi(\mathbf{r},t), \end{aligned} \tag{4.5}$$

Here, $\Psi(\mathbf{r},t)$ is the wave function of the polariton condensate, m_{eff} is the effective mass of the polaritons and γ_c is a loss rate which accounts for the finite polariton lifetime. The repulsive polariton-polariton interaction is included with a value $g_c > 0$. To model the relaxation and scattering dynamics, we introduce two reservoirs. An active reservoir (with density n_A), which directly fills the condensate and an inactive reservoir (with density n_I), which only feeds the active reservoir [14, 42]. The repulsive Coulomb interaction of condensate polaritons with both reservoirs is represented by the terms $g_\text{r} n_\text{A}$ and $g_\text{r} n_\text{I}$ in Eq. 4.5, whereby $g_\text{r} > 0$ is the interaction constant. The active reservoir models the population of exciton polaritons at energy values above the ground state, for example near the bottleneck region. Its density satisfies

$$\frac{\partial n_\text{A}(\mathbf{r},t)}{\partial t} = \tau n_\text{I}(\mathbf{r},t) - \gamma_\text{A} n_\text{A}(\mathbf{r},t) - R|\Psi(\mathbf{r},t)|^2 n_\text{A}(\mathbf{r},t). \tag{4.6}$$

The term $R|\Psi(\mathbf{r},t)|^2 n_\text{A}$ describes the stimulated scattering process, as it scales with the density of the condensate $|\Psi(\mathbf{r},t)|^2$. The coefficient R corresponds to the scattering rate of this non-linear process. γ_A is the loss rate of the active reservoir. The inactive reservoir models the electron-hole plasma excited by non-resonant pumping. Due to relaxation of the electron-hole plasma, polaritons in the active reservoir form. τ gives the rate at which the active reservoir is replenished by the inactive reservoir. The density of the inactive reservoir satisfies

$$\frac{\partial n_\text{I}(\mathbf{r},t)}{\partial t} = -\tau n_\text{I}(\mathbf{r},t) - \gamma_\text{I} n_\text{I}(\mathbf{r},t) + P(\mathbf{r},t). \tag{4.7}$$

Here, γ_I is the loss rate of the inactive reservoir and $P(\mathbf{r},t)$ is the non-resonant pump, which is energetically far above the exciton energy. For the theoretical simulations we use a ringlike excitation pump profile similar to the experiment. The exact excitation profiles and parameters of the theory simulations for this chapter can be found in Ref. [20].
The theory simulations are based on solving Eqs. 4.5-4.7 numerically using a split-step Fourier method. The nonlinear contributions are calculated by using the fourth order Runge–Kutta method on a discrete spatial grid with high resolution. The initial conditions include small uniform white noise in amplitude and phase of ψ at all grid points, while the reservoir densities are strictly zero. The initial white noise changes randomly with each run of the numerical simulation. At $t = 0$ the pump pulse is applied and leads to a buildup of particle densities in the whole system. At each point in time, the OAM of the polariton condensate may be calculated by evaluating

$$A_{\mathrm{OAM}}(m) = \int \Psi(\mathbf{r}) e^{-im\phi} d\mathbf{r}, \tag{4.8}$$

which gives the numerically sorted intensity distributions $|A_{\mathrm{OAM}}|^2$. Calculating these profiles for all time points gives a two-dimensional image that resolves the OAM of the polariton condensate in time, just like our experimental setup does.

In Fig. 4.8 we compare a measurement series of three exemplary excitation powers with the corresponding theory simulations. The excitation ring diameter is 7 μm in this case. We observe that all modes with -1, $+1$ and zero OAM shift to earlier times as excitation power increases. For low pump powers only slightly above the condensation threshold, the vortex modes with -1 and $+1$ OAM are absent while only the zero OAM mode is present. The occurrence of all modes and their temporal shift with pump power show good qualitative agreement in experiment and theory. We obtain the theoretical results by averaging over ten pulsed excitation cycles, while randomly changing the initial white noise in phase and amplitude of the wave function for each excitation cycle. The asymmetry of the -1 and $+1$ OAM states results from the small number of averaged excitation cycles and in this respect its similarity to the experimental result is a coincidence. When averaging over more excitation cycles, a symmetric distribution of -1 and $+1$ OAM states would be expected in theory. In contrast to this, the experimentally observed asymmetry of the -1 and $+1$ OAM states results from sample disorder, which is not included in the theory. Nevertheless, the theory reproduces the experimentally measured time dynamics and the power dependence of the arising modes very well.
We analyze the results shown in Fig. 4.8 for the modes forming inside a 7 μm trap in more detail. For low excitation power only slightly above the condensation threshold, solely the zero OAM mode forms, appearing delayed in comparison with higher excitation powers. The non-zero OAM modes are absent compared to the previous measurements shown in Fig. 4.6, where a larger 9 μm ring shaped excitation beam with a power also slightly above condensation threshold is used. This different occurrence of the vortex modes may be explained in the following way: The physical size of vortices is influenced by the excitation power density. As we discussed in chapter 2.3,

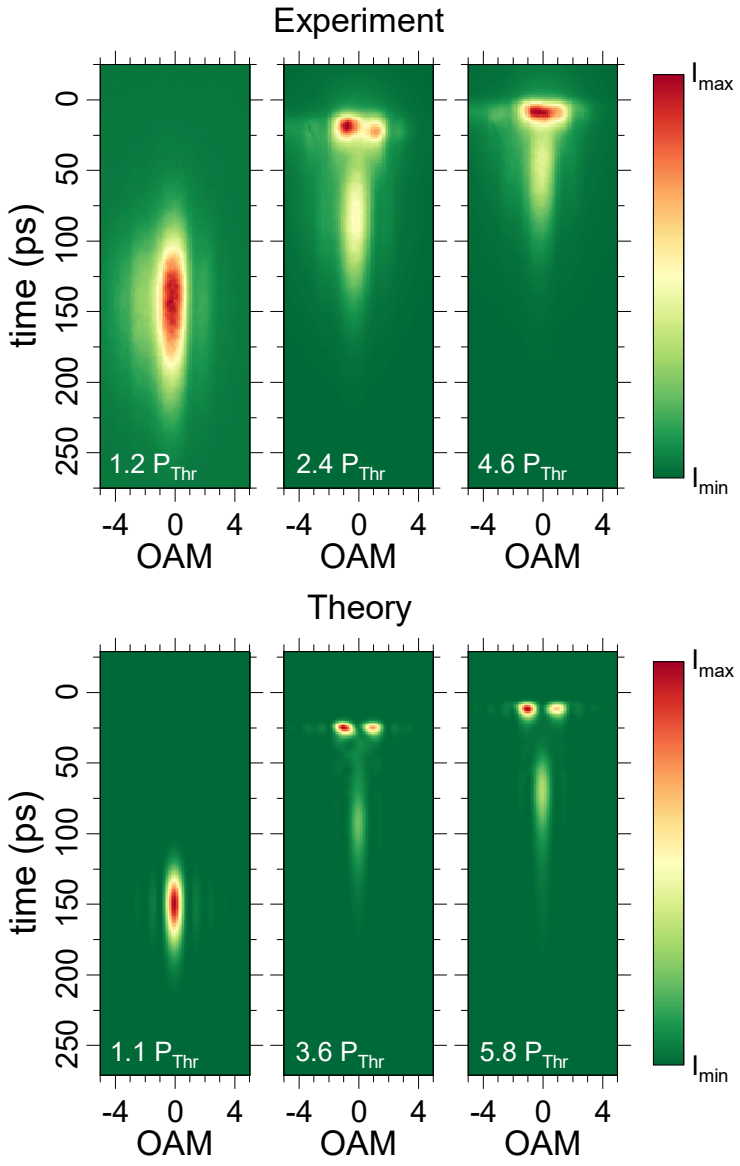

Figure 4.8: Experimental time-resolved OAM measurements for different excitation powers compared to the theoretical simulation results of this process. The color maps of the individual graphs have been scaled to the respective minimum and maximum values of each image.

the vortex size is proportional to the healing length, which is inversely proportional to the square root of the polariton field intensity. Therefore, the vortex size shrinks with increasing pump power. To enable the formation of vortices inside a trap, the physical vortex size needs to be smaller than the trap, otherwise the vortex modes can not form.

Considering both measurements with different trap diameters of 9 μm and 7 μm but similar excitation powers slightly above the condensation threshold, the spatial size of the vortices is roughly the same. While the trap with 9 μm diameter is large enough to support vortex formation, the trap with 7 μm diameter is too small, so that no vortex modes may form at the given excitation power. However, with increasing excitation power, the physical vortex size decreases and thereby vortices may also form inside the 7 μm trap.
The overall temporal dynamics of all modes also shows some power dependence. The vortex modes formed early with non-zero OAM and the zero OAM mode formed later both shift towards earlier times with increasing excitation power, whereby the zero OAM modes shows a stronger shift. The timescale of the decay of the condensate with zero OAM, however, is not modified. A significant change of this decay time is observed neither in experiment nor theory. To quantify the decay times of the modes, we extract the OAM-integrated time profiles, which are shown in Fig. 4.9. In experiment, the decay time of the peak related to the zero OAM mode initially rises with increasing power and then stabilizes at 24 ps for excitation powers well above twice the condensation threshold. This matches quite well with the lifetime of about 22 ps of the condensate predicted by the simulation. The decay time of the early peak related to the vortex modes amounts to about 12.5 ps and varies less than 1 ps in the power range above condensation threshold covered in Fig. 4.9. Contrary to this, only a lifetime around 4 ps is expected in theory, which corresponds to a deviation by more than a factor of three. We trace back this deviation to the beam shaping of the excitation laser beam. The SLM used for this process inevitably induces intensity fluctuations. Since the time dynamics of the entire process is sensitive to the excitation power, this leads to an effective broadening of all peaks in the time domain due to averaging over several excitation cycles with different pump powers. In case of the short-lived early peak related to the vortex modes, this leads to a rather big deviation of the lifetime. In case of the late peak related to the zero OAM mode, this broadening is not noticeable, since the lifetime of this mode is much longer anyway. Also it should be noted, that an unavoidable time jitter of about 1 ps is induced by the streak camera system itself. This additively broadens the peaks in experiment, though it certainly is not the main contribution.
To gain further insight into the condensation process of the different OAM modes, we analyze the theoretical model in more detail. As already discussed before, the model consists of an inactive reservoir, an active reservoir and the condensate. The condensation process is modeled by rate equations transferring the particle densities from the inactive reservoir to the active reservoir, which interacts with the condensate. The condensate forms due to nonlinear scattering from the active reservoir. The spatial shape of the inactive reservoir does not change, since there is no feedback to it from either the active reservoir or condensate. However, the spatial particle density distributions of the active reservoir and condensate may change dynamically during the whole excitation process. To understand how this happens in the specific case of pulsed ringlike excitation, we single out the simulation results for an excitation power of $4.7\,P_{Thr}$ in Fig. 4.9 and plot the real space images of the involved inactive reservoir, active reservoir

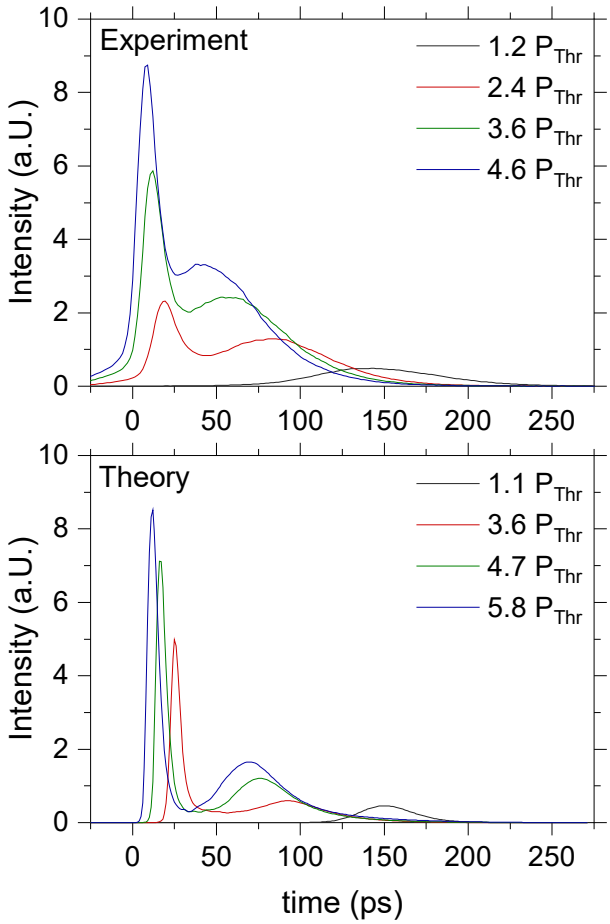

Figure 4.9: OAM-integrated time profiles of the time-resolved OAM images of experiment and theory simulations, explicitly including the images shown in Fig. 4.8.

and resulting condensate at the peak times t_1 and t_2. The resulting images obtained in a new run of the theory simulation for this excitation power are arranged in Fig. 4.10. At the peak time t_1 where the -1 and $+1$ OAM modes arise, the condensate forms a dipole mode consisting of two localized spots in real space with a π-phase jump with respect to each other. This can be understood as the result of a coherent superposition of the two counter-rotating vortex modes forming a standing wave. At this time, the active reservoir resembles the ring-shaped inactive reservoir overlapped with an intensity inverted image of the condensate. In the active reservoir, local minima matching with the high density spots of the condensate manifest due to the fact that the polariton condensation non-linearly depletes the active reservoir with a rate that rises with the condensate density.

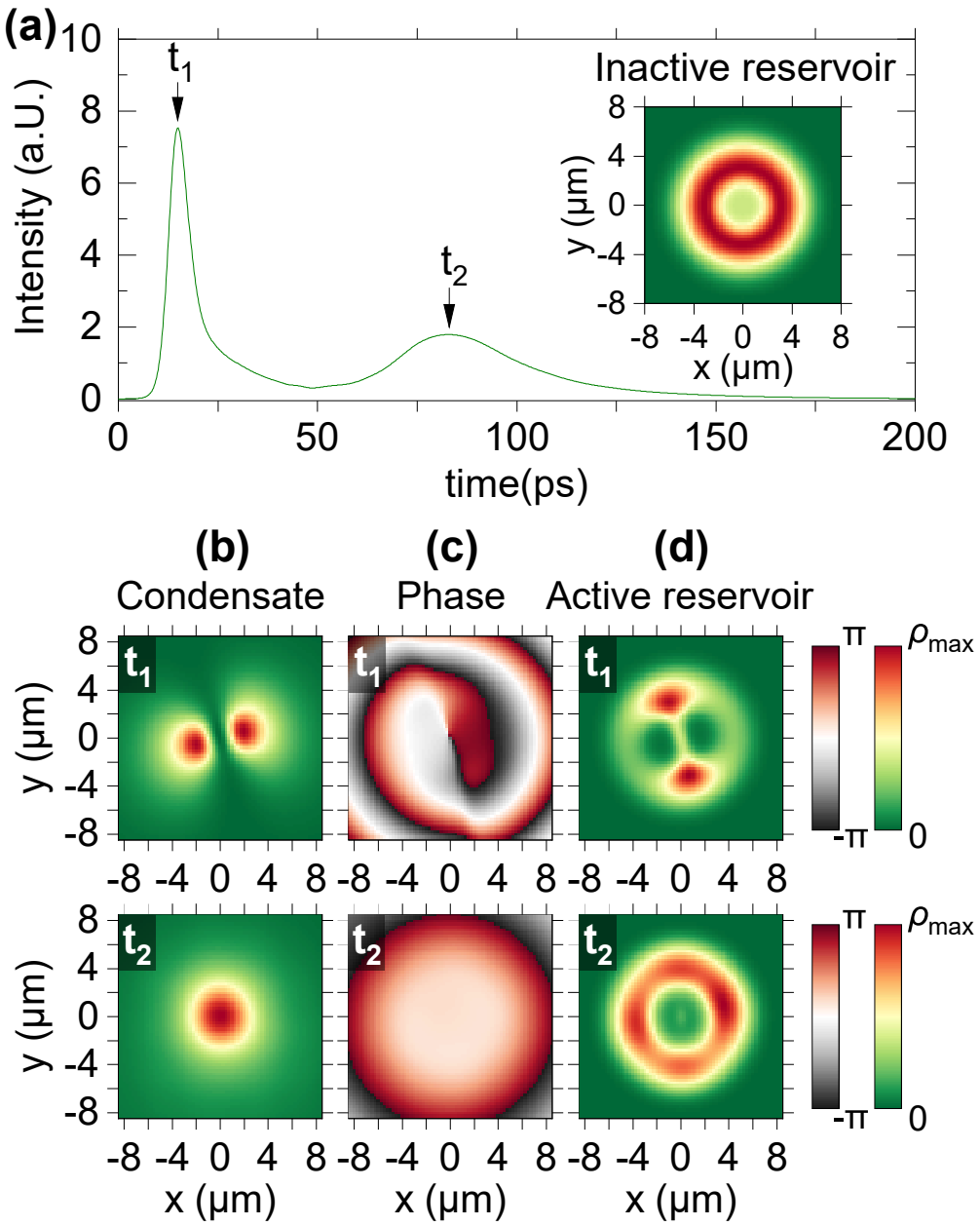

Figure 4.10: (a) The simulated OAM-integrated time profile for the excitation power of $4.7\,P_{Thr}$. The peak times are $t_1 = 15\,ps$ and $t_2 = 83\,ps$. The inset shows the persistent shape of the inactive reservoir. (b)-(d) Real space images and phase maps of the condensate and real space images of the active reservoir at the peak times t_1 and t_2. The particle density ρ_{max} at $t_1(t_2)$ is $52\,\mu m^{-2}(6.9\,\mu m^{-2})$ for the condensate and $77\,\mu m^{-2}(17\,\mu m^{-2})$ for the active reservoir.

At the peak time t_2, when the vortex modes disappeared and the zero OAM mode arises, the condensate just forms a single spot with flat phase in the center of the ringlike excitation potential. For this mode, the active reservoir is also ringlike as it inherits the shape of the inactive reservoir and the polariton population on the ring itself is not directly drained by the condensate. In this case the spatial overlap of active reservoir and condensate is very small due do the low density of hot excitons in the center of the ring-shaped inactive reservoir, which feeds the active reservoir. This results in relevant implications for the lifetime of the zero OAM mode. From Eq. 2.39, one can see that the decay rate of the condensate is given by the polariton lifetime and the feeding rate of the active reservoir, i.e. $-i\hbar\frac{\gamma_c}{2} + i\hbar\frac{R}{2}n_A(\mathbf{r},t)$. Due to the negligible overlap of condensate and active reservoir for times around t_2, we obtain $n_A\Psi \simeq 0$ and the lifetime of the OAM mode thereby becomes independent of condensate density, active reservoir density and the pumping power. Then, the condensate lifetime is just determined by the polariton lifetime: $2/\gamma_c \simeq 22\,\mathrm{ps}$. This theoretical explanation fits the experimental finding that the lifetime of the zero OAM mode is mostly independent of the excitation power, well, as already discussed regarding Fig. 4.9.

Finally, we investigate the influence of the excitation ring diameter on the formation dynamics of the polariton condensate. Fig. 4.11 shows time-resolved OAM measurements with different ring diameters at approximately the same excitation power density. At the selected excitation powers, only for ring diameters above $6\,\mu$m vortex modes with -1 and $+1$ OAM form. Considering the discussion of the results shown in Fig. 4.8, a possible explanation for this behavior is that the diameter of $6\,\mu$m is smaller than the vortex size at the given excitation power and thereby only the zero OAM mode may form. With increasing ring diameter the zero OAM mode broadens in time significantly and its onset shifts to a later time. For a ring diameter of $7\,\mu$m, the spontaneously formed vortex modes decay rapidly, while for a ring diameter of $9\,\mu$m a slower decay is observed. At the larger ring diameter also a slight movement of both non-zero OAM sorting spots by about one third of a topological charge towards more positive OAM values is observed. However, the zero OAM mode does not move along the OAM axis. The significant broadening and shift of the zero OAM mode in time with increasing ring diameter may be explained by a change of the small spatial overlap between the zero OAM mode and the reservoir. For small ring diameters the spatial overlap is comparatively large, which means the zero OAM mode is populated fast but also decays rapidly. With increasing ring size the spatial overlap shrinks and the whole process of building up the mode and following decay is slowed down. As a result, the peak shifts to a later time and the broadening in time accrues.

The spots of the $m = -1$ and $m = +1$ vortex modes for ring diameters of $7\,\mu$m and $9\,\mu$m shown in Fig. 4.11 are very different. For the $7\,\mu$m ring excitation the OAM spots are shorter-lived and well defined, whereas for the $9\,\mu$m ring excitation longer living tilted spots with changing OAM appear. Since the excitation power density is similar in both cases, also the physical vortex diameter is about the same. A highly probable explanation for the tilt of the OAM spots is that both vortices are actually moving alongside inside the large trap, for example due to an asymmetric intensity distribution of the excitation pump ring or the disorder potential of the sample. The movement

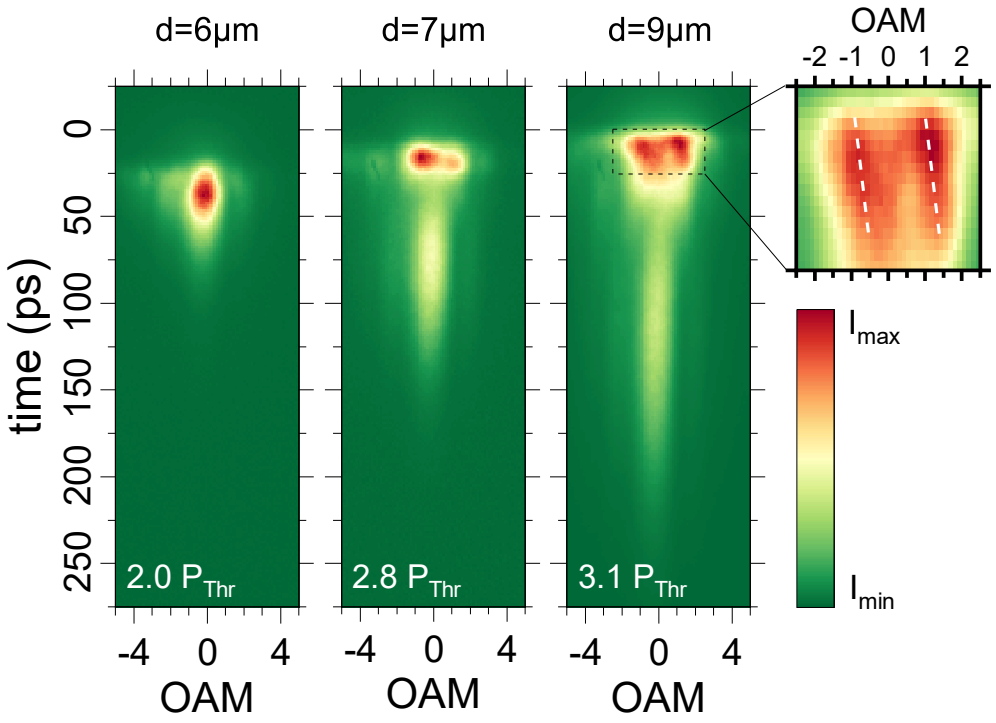

Figure 4.11: Time-resolved OAM measurements for excitation with different ring diameters d and approximately the same excitation power density. For $d = 6\,\mu$m only a zero OAM mode forms. For the bigger ring diameters, two modes with -1 and $+1$ OAM form. At $d = 9\,\mu$m the OAM peaks of these modes are simultaneously moving with advancing time, which corresponds to a movement of the vortices inside the trap. The color maps of the individual graphs have been scaled to the respective minimum and maximum values of each image and the pump power relates to the condensation threshold of ringlike excitation with the corresponding diameter.

of a vortex away from the initially centered position on the optical axis results in a transverse momentum of the signal beam when the microscope objective performs an optical Fourier transformation of the off-centered polariton emission. Since this transverse momentum corresponds to extrinsic OAM components, the OAM physically changes with respect to the aligned reference axis of the OAM sorting setup and thereby causes a shift of the OAM peaks. This movement is only possible if the ring diameter is somewhat larger than the actual vortex size. In the case of the $7\,\mu$m ring we conclude the vortices to be well confined in the potential and not moving at all. Furthermore, a movement of the vortices inside the trap might also explain the enhanced lifetime of the vortices excited using a $9\,\mu$m ring. When a vortex moves from the central position towards the border of the ring trap, the spatial overlap with the feeding reservoir changes and becomes inhomogeneous. The feeding rate of the condensate rises for some areas of the trap while it decreases for some other areas of the trap. Thereby an

asymmetric time profile with a long living tail is generated. Overall, the timescale of all formed OAM modes is strongly influenced by the excitation ring diameter.
The discussion of the results in Fig. 4.11 also sheds new light on the previously presented results for excitation with a 9 μm ring shown in Fig. 4.6. For the higher excitation power the OAM sorted spots are slightly tilted and display an asymmetric time evolution, which may be explained by a movement of the formed vortices to the border of the trap. However, this is not the case for the lower excitation power just slightly above the condensation threshold. For the lower excitation power, the physical vortex size is larger, hence also well confined within the 9 μm ring trap.
To conclude this section, we have investigated the exciton polariton condensation process for ringlike excitation with different excitation powers and ring diameters. We observed the spontaneous formation of -1, $+1$ and zero OAM modes and studied the influence of the excitation power and ring diameter on these modes experimentally and theoretically.

4.2.3 Spin-orbit coupling

In addition to the temporal dynamics of the spontaneously created vortices, we also examine the spin of the exciton polariton vortices and extend the experimental setup by suitable polarization optics to detect both spin related circular polarization components. For most experimental conditions both spin components equal each other. However, in some cases an asymmetry of the OAM modes that is correlated with the spin components appears, depending on the sample disorder. An example for this effect is shown in Fig. 4.12. In the σ^+ spin component, the -2 OAM state is dominant, while in the σ^- spin component, the $+2$ OAM state is dominant. This related appearance of OAM modes and spin components corresponds to spin-orbit coupling of exciton polaritons. We trace the appearance of $m = \pm 2$ OAM modes back to the slightly higher ring diameter compared to the results shown in Fig. 4.8 combined with excitation powers well above twice the condensation threshold and a local sample disorder supporting the $m = \pm 2$ OAM modes. Considering the cross-sections of the appearing OAM modes, the effect seems to be intensity dependent. To quantify this dependence, we extract the degree of circular polarization (DCP) of the modes using the profiles shown in Fig. 4.8. The intensities of the -2 and $+2$ OAM modes are calculated by integrating the profiles in intervals $[-3, -1]$ and [1,3] centered around the peaks of both arising OAM modes. The DCP then is calculated as:

$$\rho_{\mathrm{m}} = \frac{I_{\sigma^+} - I_{\sigma^-}}{I_{\sigma^+} + I_{\sigma^-}}, \tag{4.9}$$

$$\tag{4.10}$$

with the integrated intensities I_{σ^+} and I_{σ^-} of the corresponding OAM mode with topological charge m. The resulting DCP values for the lower pumping power of $2.5\,P_{\mathrm{Thr}}$ are $\rho_{-2} = 0.148$ and $\rho_2 = -0.247$, while the DCP values for the higher pumping power of $3.6\,P_{\mathrm{Thr}}$ are $\rho_{-2} = 0.019$ and $\rho_2 = -0.099$. The experimental observation shows that the intensities of both appearing non-zero OAM modes converge to each

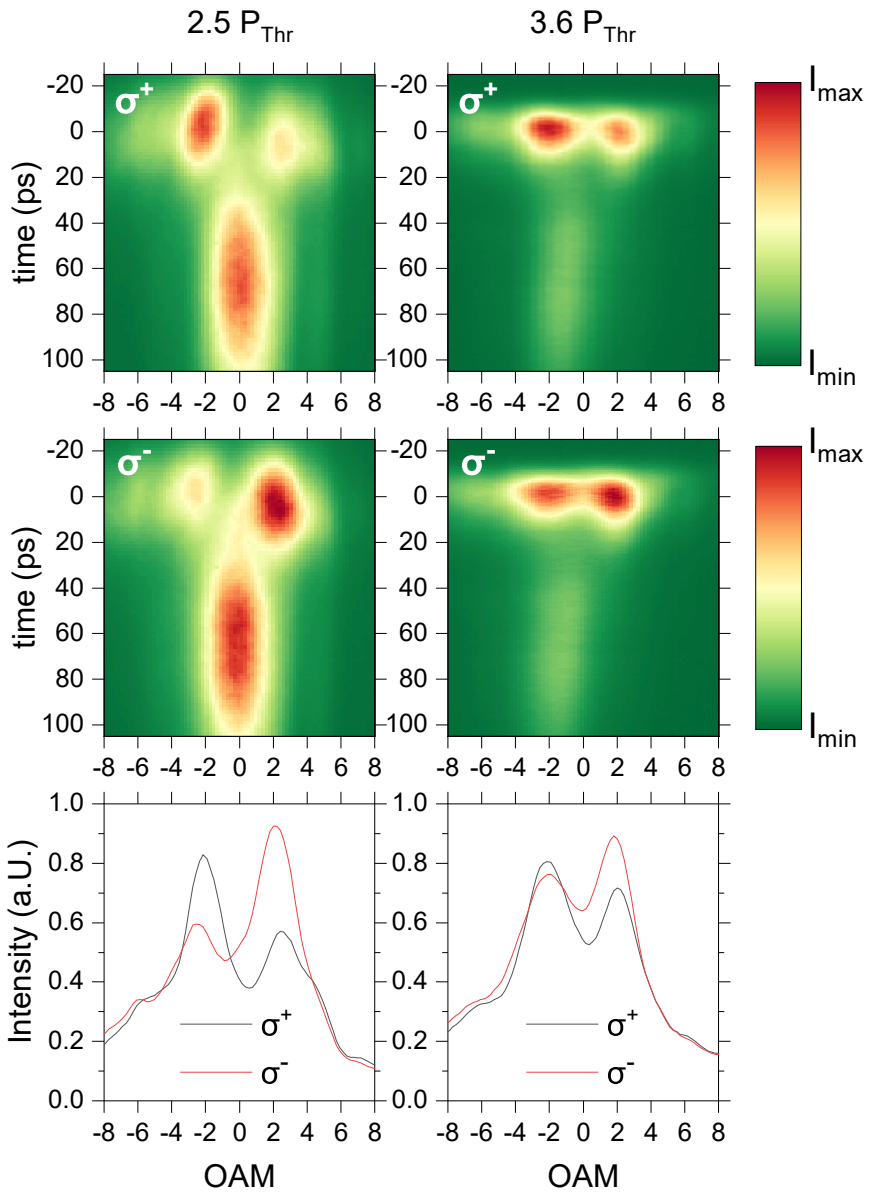

Figure 4.12: Time-resolved OAM measurements for different excitation powers (left and right column) and circular polarization states σ^+ and σ^-. The plots on the bottom row show the time profiles of the images above, integrated in a time frame of -20 ps to +20 ps. Two OAM modes with $m = -2$ and $m = +2$ are formed, appearing with clearly distinct intensities levels in both detected circular polarizations. The intensities of the OAM peaks detected at different circular polarizations converge to each other at the higher excitation power. The time $t = 0$ ps in this graph marks the peak of the detected intensity, not the time of excitation. The ring diameter is 7.5 μm.

other with increasing excitation power and the degree of circular polarization drops. Similar to our experimental results, spin-orbit coupling of exciton polaritons has been observed before in an etched structure of coupled micropillars arranged in the form of a hexagonal photonic molecule [78]. There, the spin-orbit coupling arises from the polarization-dependent confinement and tunneling of photons between adjacent micropillars. However, the origin of spin-orbit coupling inside the all optically excited annular trapping potential in our planar microcavity is still unknown. In future work, finding a conclusive theoretical explanation for this spin-orbit coupling might be beneficial for understanding the underlying physics and exploiting it in manufactured tailored exciton polariton systems. In any case, the presence of spin-orbit coupling in a polariton system with rotationally symmetric trapping potentials is expected to affect the modes that arise [79].

4.3 Realization of vortex switching

After having studied the spontaneous creation of vortices, we now focus on controlling the topological charge of the created vortices. The concept and key elements enabling vortex switching following Ma, et al. [19] are briefly presented in the following. The basic theory model for simulating the time evolution of the polariton condensate is identical to the one presented in chapter 4.2.2. The exact excitation profiles and parameters of the theory simulations for this chapter can be found in Ref. [19]. A sketch of the excitation geometry is shown in Fig. 4.13.

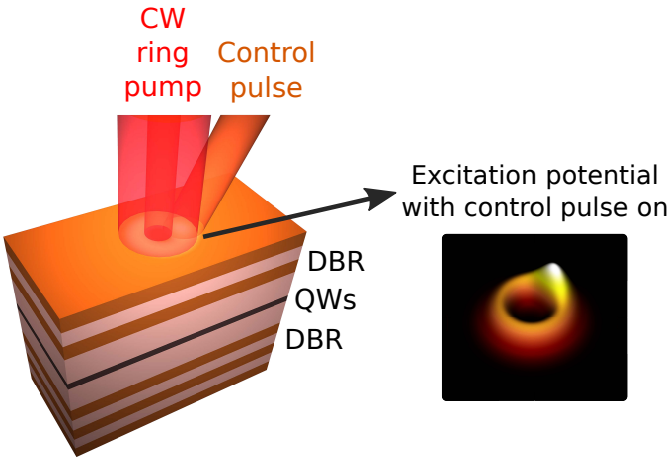

Figure 4.13: Sketch of the tailored excitation setup with two lasers used for vortex switching. The ring shaped CW pump creates a rotationally symmetric trapping potential, inside which polariton vortices may form spontaneously. While the additional Gaussian control pulse is switched on, it creates a temporary potential barrier, intentionally breaking the rotational symmetry and thereby enabling the switching of vortices inside the ring trap.

We use two excitation lasers for this experiment. An annular shaped CW laser creates the ringlike trap, while a pulsed laser with Gaussian beam shape acts as the control beam to manipulate the vortices forming inside the CW ring trap. The control pulse forms an additional potential barrier, which breaks the rotational symmetry of the system and may influence the topological charge of already existing vortices inside the annular trap. In Fig. 4.14 a theoretical simulation of this process is illustrated.

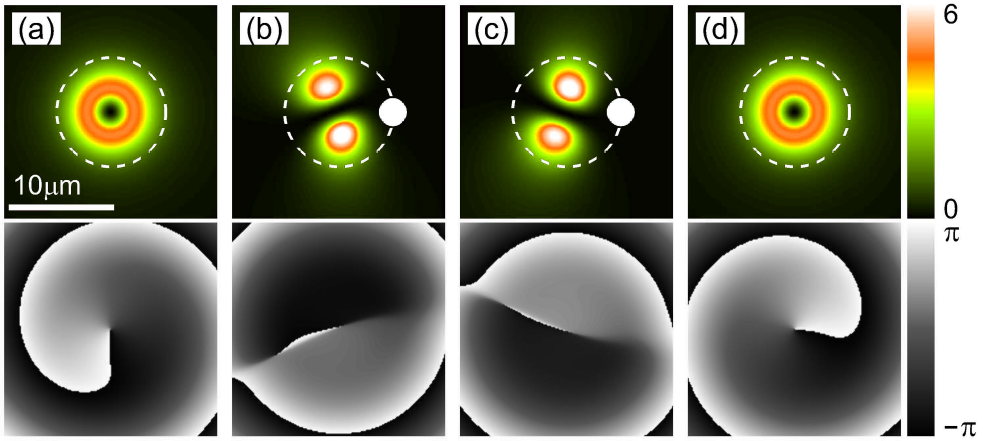

Figure 4.14: Principle of vortex switching. Panels (a)-(d) show the real space images of the polariton density (given in μm^{-2}) with the corresponding real space phase maps below at selected points in time, following each other from left to right. In (a) a $m = +1$ vortex forms inside the CW excited ringlike potential, which is indicated by the white dashed circle. When the additional Gaussian control pulse is switched on (indicated by the solid white circle), an oscillating dipole mode of two spots with π-shifted phase to each other forms as shown in (b) and (c) for different points in time. After the control pulse is switched off, the system returns to a vortex mode depending on the oscillation state of the dipole at the time when the control pulse is switched off. Panel (d) shows an example of successful vortex switching, where finally the topological charge amounts to $m = -1$, therefore opposite to the initial vortex state in (a).

The images from left to right in Fig. 4.14 show the simulated real space of the polariton density and corresponding phase maps of the polariton wave function during the switching process with advancing time. In Fig. 4.14(a), a spontaneously formed $m = +1$ vortex exists. When the control pulse is switched on, the rotational symmetry of the optically imprinted trapping potential is intentionally broken and a dipole mode forms, as seen in Fig. 4.14(b) and (c). While the Gaussian control pulse is switched on and perturbs the vortex by forming a local potential barrier, this dipole mode oscillates back and forth between the two states shown in Fig. 4.14(b) and (c). Once the control pulse is switched off and the potential barrier fades, the dipole mode turns back into a vortex mode, which may have a topological charge opposite to the initial state, as shown in Fig. 4.14(d). The topological charge of the final vortex state depends on the rotation direction of the oscillating dipole at the time, when the potential barrier is sufficiently reduced to allow stable formation of vortices again. Thus, a control pulse

with the right duration relative to the oscillation period of the dipole may switch the topological charge of an already formed vortex inside an annular trap. Fig. 4.15(a) shows an example of switching a vortex to the same or opposite topological charge using pulses with different durations. Also, the height of the potential barrier (given by the control pulse intensity) influences the oscillation frequency of the dipole. Thereby, the final state of the switching process results from a combination of both pulse intensity a and duration w_t, as shown in 4.15(b). For the practical realization of vortex switching, this information is crucial, although the actual implementation is a bit more sophisticated than this model.

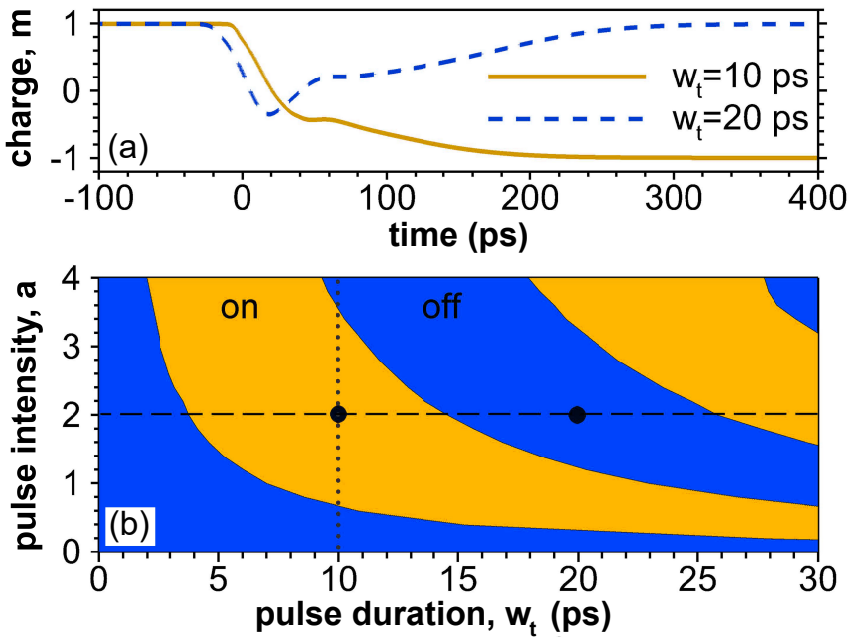

Figure 4.15: Detailed analysis of the conditions for successful vortex switching. Panel (a) compares the time evolution of the average topological charge of the total polariton condensate for different parameters sets with varying control pulse duration w_t and fixed intensity $a = 2$. For $w_t = 10\,\text{ps}$ the topological charge is switched whereas for $w_t = 20\,\text{ps}$ the charge returns to its initial $m = +1$ vortex state. Panel (b) shows a computed parameter map of the pulse intensity a and pulse duration w_t, which identifies parameter spaces for successful switching, marked in orange color. The blue areas indicate parameter sets leading back the the initial states, showing no vortex switching. The black dots mark the parameter sets used in panel (a).

In the experimental realization, the pulse duration cannot be adjusted easily to predefined values with few picoseconds precision. Besides the technical expense to temporally shape the excitation laser in the limits of the physically fundamental energy-time uncertainty relation, also the polariton relaxation and condensation process strongly influence the lifetime of the ultimately formed potential barrier, which perturbs the already formed vortex. For this reason we vary the easily adjustable pulse intensity

instead. According to Fig. 4.15(b), varying the pulse intensity also offers settings allowing vortex switching. Hereby, short pulse durations of only few picoseconds are a priori not reachable in experiment, due to the polariton relaxation and condensation process. The fastest decay channel of the reservoir excitons, which yield the largest contribution to the potential barrier, is given by relaxation and stimulated scattering into the ground state followed by a radiative decay from the polariton condensate. However, the cavity lifetime of around 8 ps sets a strict lower bound for the lifetime of the condensate polaritons. As a consequence, the pulse duration effectively exceeds the duration of the 120 fs pump pulses generated by the pulsed laser.
As already seen in the results for pulsed annular excitation in section 4.2.1, both vortex modes with $m = -1$ and $m = +1$ form simultaneously. During the time $t < 0$ ps before the additional non-resonant control pulse arrives, both OAM modes exist, whereby the +1 OAM mode is dominant. At $t = 0$ ps the additional control pulse is applied, which creates a temporary potential barrier, perturbing the formed vortices. Its impact depends on the control pulse power. For a low pulse power of 1 mW, at t$\sim$ 100 ps the $m = +1$ vortex mode is suppressed and the $m = -1$ vortex mode dominates for a short period of time. After that, the $m = +1$ vortex mode prevails again and the system gradually returns to the initial state as seen for $t < 0$ ps. For a slightly higher control pulse power of 4 mW, the intensity of both vortex modes oscillates with the $m = -1$ vortex mode being dominant after application of the control pulse. At around $t \sim 300$ ps, the signal stabilizes in a setting with a dominant $m = -1$ vortex mode, which means that the initially dominant vortex mode $m = +1$ is switched to the opposite topological charge $m = -1$. The system remains in this switched state for more than 1.5 ns until it gradually reverts back to the initial state with a dominant $m = +1$ vortex mode. When the control pulse power is increased further to 20 mW, the system also performs an intermediate oscillation until it reverts back to the initial setting with a dominant $m = +1$ vortex mode at around t$\sim$ 600 ps. In this case no switching happens, like for the lowest excitation power. For the intermediate excitation power, we indeed observe vortex switching. This behavior agrees well with the theoretical prediction, shown in Fig. 4.15. As a side note, the oscillating behavior lasting more than 100 ps after application of the control pulse also implies that the effective lifetime of the potential barrier is vastly increased compared to the short duration of the 120 fs control pulses. This is a consequence of the rather complex polariton relaxation and condensation process.
The results shown in Fig. 4.16 demonstrate that the vortex switching scheme works and imply that it also may be applied in different material systems. However, the detection of the vortex switching using the presented experimental setup is not a trivial task and requires the vortex modes to fulfill some requirements, which we explain a bit further at this point. At first glance, the simultaneous formation of two vortex modes seems to be a disadvantage for observation of the vortex switching since the signal looks more complex and the relative change of the OAM peak intensities is more difficult to observe. However, the isolated occurrence of only one vortex mode would mean that the sample disorder strongly suppresses the formation of the other vortex mode with opposite topological charge. Thereby also no switching to this mode

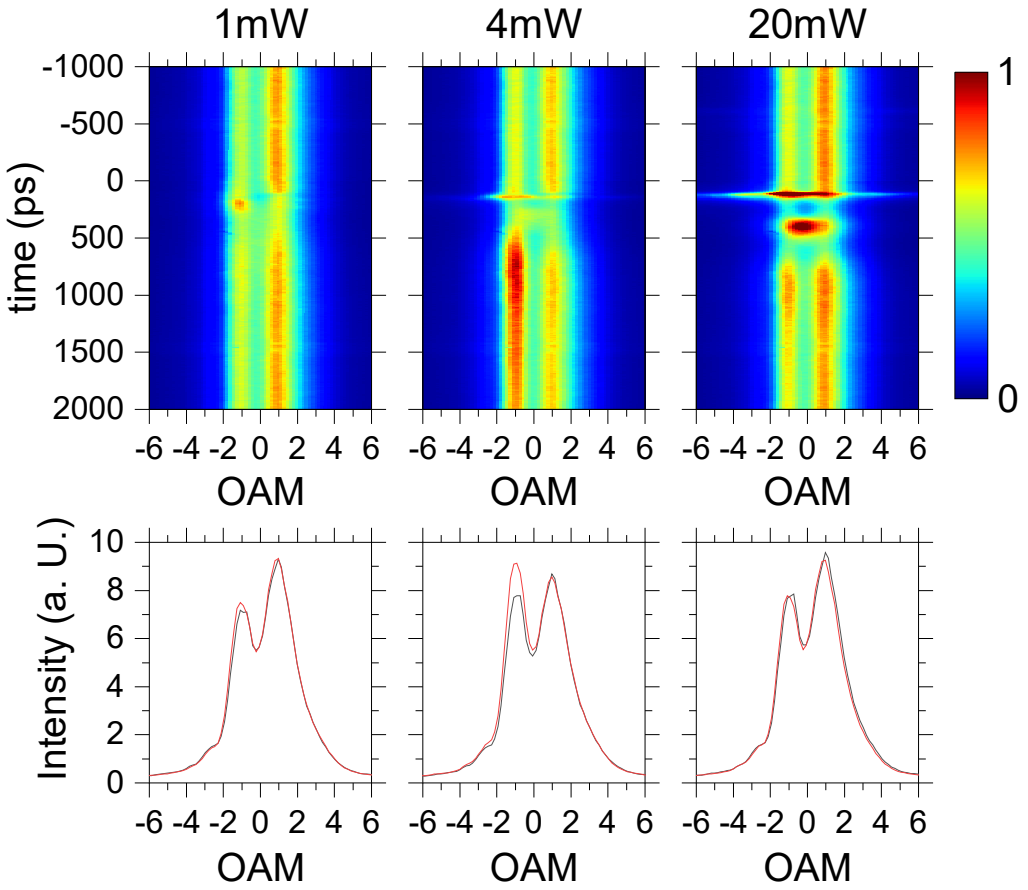

Figure 4.16: Experimental time-resolved OAM measurements of the sample emission for different control pulse powers and the relating cross-sections at $t = -1\,\mathrm{ns}$ (black) and $t = 1\,\mathrm{ns}$ (red) plotted below. The images for different powers are normalized individually. At $t < 0\,\mathrm{ps}$ only the annular CW excitation beam is on and two vortex modes with $m = -1$ and $m = +1$ form, whereby the $m = +1$ modes is dominant. At $t = 0\,\mathrm{ps}$ the control pulse perturbs the previously formed vortices. After perturbation with a 1 mW control pulse the condensate returns to the initially dominant $m = +1$ vortex state. For a slightly increased power of 4 mW, the $m = -1$ vortex state is clearly dominant after the perturbation. Thus a switching of the topological charge is evidenced. When increasing the power further to 20 mW, the condensate again returns to the initially dominant $m = +1$ state after the perturbation and no vortex switching appears.

would be possible, since the switched vortex mode may not form at all. So in fact, when switching vortices which are spontaneously formed inside a trapping potential, the initial appearance of both OAM modes is necessary to perform vortex switching. Additionally there obviously needs to be a dominant mode with higher intensity so that the vortex switching may be noticed. With two OAM peaks of same intensity the

switching could not be identified, if it occurs. Another relevant aspect is that after some time the switched vortex state automatically reverts back to the initial state. Due to this, the system is reset between two control pulses and thereby allows the vortex switching to be detected even when the streak camera integrates over more than 10^6 pulses in each measurement. Otherwise the continuous switching forth and back between both vortex modes would result in an averaged image with two peaks of identical intensity. If the system did not automatically reset itself, it still could be reset between two control pulses using a more complicated excitation scheme, for example by blocking the CW laser between the arrival of consecutive control pulses using an electro-optical modulator.
In conclusion, the controlled manipulation of vortices implementing the switching of the topological charges of vortices has been successfully demonstrated experimentally and theoretically. This specific case of detecting two spontaneously formed vortex modes with opposite topological charges especially highlights the advantage of the applied OAM spectroscopy method over interferometry techniques.

Chapter 5

Conclusion and Outlook

To conclude, we successfully implemented and applied the OAM sorting method for spectroscopy of OAM states. At this we have shown that similar to a cylindrical lens [66, 67] the OAM sorting method may also be used to selectively measure the intrinsic and total OAM of fractional OAM states with non-integer OAM values. Furthermore, we successfully demonstrated the application of the OAM sorting method for OAM spectroscopy by confirming and extensively investigating the formation of exciton polariton vortices inside ringlike traps. We find several independent modes with zero and non-zero OAM forming inside the annular traps. The temporal dynamics of all forming modes is strongly influenced by the ring diameter and excitation power. We examine how the formation and decay of the modes is influenced by the spatial overlap between the condensate and the active reservoir. At a trap diameter comparable to the vortex size, the vortices are well confined, whereas a larger trap diameter enables the movement of vortices inside the trap. We are also able to observe spin-orbit coupling of the microcavity exciton polaritons. However, a microscopic description of this effect requires more research as it is not always present. Investigating the exact circumstances for its occurrence might be beneficial for utilizing spin-orbit coupling in optical information processing.

Last but not least, we demonstrate the control of the rotational direction of exciton polariton vortices by flipping the sign of the topological charge of trapped vortices. Hereby, the vortices are maintained by a CW pump laser. This continuous pumping renders it possible to use these trapped vortices as a means for long lasting information storage in all optical information processing. Since the microcavity exciton polaritons naturally decay, controlling the topological charges of vortices permanently maintained by CW pumping might be a beneficial approach to store information all optically on time scales several orders of magnitude longer than the polariton lifetimes. In this concept, the traps could either be created all optically or manufactured by structuring the sample.

In general our time-resolved OAM spectroscopy technique with its versatile operation modes might be applied to any other material system or structures that emit light with OAM. The OAM spectroscopy technique itself potentially could be improved in

terms of reducing the overlap between adjacent OAM sorted modes with $\Delta l = 1$ by using a different optical transformation, which transforms the phase gradient of a light beam by mapping spirals to parallel lines [80]. There are also many possibilities for further research regarding the exciton polariton system. The theory predictions include several interesting phenomena such as multistability of different vortex modes in the same trapping potential [81], half vortices [82], vortex-vortex control in a system of multiple vortices [83] and spiraling motion of vortices inside a trap much bigger than the vortices [84]. Also, considering recent advances regarding optical processing of light beams with OAM, such as OAM multiplication and division by arbitrary rational factors [85], the investigation of non-linearly interacting exciton polariton vortices is an exciting field for future research.

Appendix A

Simulation of OAM Sorting

The OAM sorting process can be tracked by simulating the propagation of a light beam, which passes through the OAM sorting phase elements and all other optical components in the beam path. This simulation is implemented in Matlab. The source files of all classes are given below.

OAMSorting.m

```
% Simulates the OAM Sorting process by beam propagation
% The parameters should be set to values used in experiment

PixelNum=4001; % set an odd pixel number so that a central pixel
    representing the optical axis is available

BeamWidth=1000*10^(-6); % Gaussian beam with, unit: m

m=1; % define the topological charge
theta_d=0; % rotation angle in deg for vortices with non-integer m

d=0.004; % size of the beam in the corrector plane in m
a=d/(2*pi);
b=0.00677;% parameter for beam position in the corrector plane

dx=8*10^(-6);% grid resolution in m ; mostly the SLM resolution

PadgettTrafoLensFocus=0.1; % lens focus of OAM Sorting in m
CCDLensFocus=0.75; % lens focus for imaging the output light beam

Lambda=773*10^(-9); % unit: m
k0=2*pi/Lambda;

% Define X and Y mesh grids for phase element calculation:
```

```
n_points=(PixelNum-1)/2;
Vx=(dx*[-n_points:n_points]);
[XX,YY]=meshgrid(Vx,Vx);

% Calculate the phase elements of OAM sorting and used lenses:
PP=PadgettTransform(XX,YY,a,b,Lambda,PadgettTrafoLensFocus);
PC=PadgettCorrector(XX,YY,a,b,Lambda, PadgettTrafoLensFocus);
PL=CreateLensPhase(XX,YY,k0,PadgettTrafoLensFocus);
CCDLens=CreateLensPhase(XX,YY,k0,CCDLensFocus);

% Create the initial beam with vortex phase
PropField=sqrt(CreateGaussianIntensity( XX,YY,BeamWidth ));
PropField=PropField.*exp(1i.*CreateVortexPhase( XX,YY,m,theta_d ));

% optional: Initial propagation distance towards OAM Sorting
%PropField=PropagateLightField( PropField,dx,1.5,k0 );

% Subequently apply the phase elements including lens phases
% and propagate the light field from plane to plane:
PropField=PropField.*exp(1i.*PP);
PropField=PropagateLightField(PropField,dx,PadgettTrafoLensFocus,k0);
PropField=PropField.*exp(1i.*PL);
PropField=PropagateLightField(PropField,dx,PadgettTrafoLensFocus,k0);
PropField=PropField.*exp(1i.*PC);
PropField=PropagateLightField(PropField,dx,CCDLensFocus,k0);
PropField=PropField.*exp(1i.*CCDLens);
PropField=PropagateLightField(PropField,dx,CCDLensFocus,k0);

CCDImage=abs(PropField).^2; % Extract intensity image in CCD plane

figure(1)
imagesc(CCDImage); % plot OAM sorting spot
figure(2)
plot(sum(CCDImage,2)); % plot profile of OAM spot
hold on
```

CreatePadgettTransform.m

```
function [ PC ] = CreatePadgettTransform( XX, YY, a, b, Lambda, f )
% Create transform pattern according to Berkhout (2010) paper

PC=(2*pi*a/(Lambda*f))*(YY.*atan2(YY,XX)-XX.*log(((XX.^2+YY.^2)
    .^(0.5))/b)+XX);
PC(isnan(PC))=0; % just for catching nan

end
```

CreatePadgettCorrector.m

```
function [ PP ] = CreatePadgettCorrector( XX, YY, a, b, Lambda, f )
% Create phase correction pattern according to Berkhout (2010) paper

PP=-(2*pi*a*b/(Lambda*f))*(exp(-XX./a).*cos(YY./a));

end
```

CreateLensPhase.m

```
function [ LensPhase ] = CreateLensPhase( XX, YY, k0, f )
% Creates a parabolic lens function with a given focal length

LensPhase=-(k0/(2*f)).*(XX.^2 +YY.^2);
LensPhase=LensPhase-ones(size(XX))*min(min(LensPhase));

end
```

CreateGaussianIntensity.m

```
function [ GaussianInt ] = CreateGaussianIntensity( XX, YY, Width )
% Creates a centered Gaussian intensity map

GaussianInt=exp(-(sqrt(XX.^2 +YY.^2)).^2./(2*Width^2));

end
```

CreateVortexPhase.m

```
function [ VortexPhase ] = CreateVortexPhase( XX, YY, charge, ang )
%VortexPhase Create vortex phase pattern
% Topological charge and rotation angle can be adjusted.
% The rotation is counterclockwise with positive values.

ang=ang*pi/180; %Convert rotation angle to radian
VortexPhase=charge*angle((XX*cos(ang)-YY*sin(ang))-1i*(XX*sin(ang)+
    YY*cos(ang)));
VortexPhase=mod(VortexPhase,2*pi);

end
```

PropagateLightField.m

```
function [ OutputField ] = PropagateLightField( InputField, dx, dz,
    k0 )
% Propagate the input light field by a given distance dz
% Field matrix should be quadratic

n_points=(size(InputField,1)-1)/2;

kMax=pi/(2*dx);
dk = kMax*2 / n_points;

Vk = (dk*[-n_points:n_points]);
[Kx,Ky] = meshgrid(Vk,Vk);

Kz=((k0^2)-(Kx.^2 +Ky.^2)).^(0.5);

FTField=ifftshift(fft2(InputField)); % 2D Fourier trafo of real
    space

FTField=FTField.*exp(1i.*Kz.*dz); % propagate in Fourier space

OutputField=ifft2(fftshift(FTField)); % Transform back to real
    space


end
```

Bibliography

[1] P. A. Clayton and M. Price. *The seven wonders of the ancient world*. London ; New York : Routledge (1988).

[2] A. Baas, J. P. Karr, H. Eleuch and E. Giacobino. *Optical bistability in semiconductor microcavities*. Phys. Rev. A, **69**, 023809 (2004). doi:10.1103/PhysRevA.69.023809.

[3] A. Amo, J. Lefrere, S. Pigeon, C. Adrados, C. Ciuti, I. Carusotto, R. Houdré, E. Giacobino and A. Bramati. *Superfluidity of polaritons in semiconductor microcavities*. Nature Physics, **5**, 11, 805 (2009). doi:10.1038/nphys1364.

[4] J. Kasprzak, M. Richard, S. Kundermann, A. Baas, P. Jeambrun, J. M. J. Keeling, F. M. Marchetti, M. H. Szymanska, R. Andre, J. L. Staehli, V. Savona, P. B. Littlewood, B. Deveaud and L. S. Dang. *Bose-einstein condensation of exciton polaritons*. Nature, **443**, 7110, 409 (2006). doi:10.1038/nature05131.

[5] T. Gao, P. S. Eldridge, T. C. H. Liew, S. I. Tsintzos, G. Stavrinidis, G. Deligeorgis, Z. Hatzopoulos and P. G. Savvidis. *Polariton condensate transistor switch*. Phys. Rev. B, **85**, 235102 (2012). doi:10.1103/PhysRevB.85.235102.

[6] H. S. Nguyen, D. Vishnevsky, C. Sturm, D. Tanese, D. Solnyshkov, E. Galopin, A. Lemaître, I. Sagnes, A. Amo, G. Malpuech and J. Bloch. *Realization of a double-barrier resonant tunneling diode for cavity polaritons*. Phys. Rev. Lett., **110**, 236601 (2013). doi:10.1103/PhysRevLett.110.236601.

[7] D. Ballarini, M. De Giorgi, E. Cancellieri, R. Houdré, E. Giacobino, R. Cingolani, A. Bramati, G. Gigli and D. Sanvitto. *All-optical polariton transistor*. Nature Communications, **4**, 1778 (2013). doi:10.1038/ncomms2734.

[8] A. Amo, T. C. H. Liew, C. Adrados, R. Houdré, E. Giacobino, A. V. Kavokin and A. Bramati. *Exciton-polariton spin switches*. Nature Photonics, **4**, 6, 361 (2010). doi:10.1038/nphoton.2010.79.

[9] K. G. Lagoudakis, M. Wouters, M. Richard, A. Baas, I. Carusotto, R. Andre, L. S. Dang and B. Deveaud-Pledran. *Quantized vortices in an exciton-polariton condensate*. Nature Physics, **4**, 9, 706 (2008). doi:10.1038/nphys1051.

[10] H. Deng, H. Haug and Y. Yamamoto. *Exciton-polariton bose-einstein condensation.* Rev. Mod. Phys., **82**, 1489 (2010). doi:10.1103/RevModPhys.82.1489.

[11] B. Berger. *Hydrodynamik von Exziton-Polaritonen in GaAs basierten Mikrokavitäten.* Master's thesis, TU Dortmund (2016).

[12] G. Nardin, K. G. Lagoudakis, B. Pietka, F. Morier-Genoud, Y. Léger and B. Deveaud-Plédran. *Selective photoexcitation of confined exciton-polariton vortices.* Phys. Rev. B, **82**, 073303 (2010). doi:10.1103/PhysRevB.82.073303.

[13] D. Sanvitto, F. M. Marchetti, M. H. Szymańska, G. Tosi, M. Baudisch, F. P. Laussy, D. N. Krizhanovskii, M. S. Skolnick, L. Marrucci, A. Lemaître, J. Bloch, C. Tejedor and L. Viña. *Persistent currents and quantized vortices in a polariton superfluid.* Nature Physics, **6**, 527 (2010). doi:10.1038/nphys1668.

[14] K. G. Lagoudakis, F. Manni, B. Pietka, M. Wouters, T. C. H. Liew, V. Savona, A. V. Kavokin, R. André and B. Deveaud-Plédran. *Probing the dynamics of spontaneous quantum vortices in polariton superfluids.* Phys. Rev. Lett., **106**, 115301 (2011). doi:10.1103/PhysRevLett.106.115301.

[15] R. Dall, M. D. Fraser, A. S. Desyatnikov, G. Li, S. Brodbeck, M. Kamp, C. Schneider, S. Höfling and E. A. Ostrovskaya. *Creation of orbital angular momentum states with chiral polaritonic lenses.* Phys. Rev. Lett., **113**, 200404 (2014). doi:10.1103/PhysRevLett.113.200404.

[16] T. Boulier, H. Terças, D. D. Solnyshkov, Q. Glorieux, E. Giacobino, G. Malpuech and A. Bramati. *Vortex chain in a resonantly pumped polariton superfluid.* Scientific Reports, **5**, 9230 (2015). doi:10.1038/srep09230.

[17] T. Boulier, E. Cancellieri, N. D. Sangouard, Q. Glorieux, A. V. Kavokin, D. M. Whittaker, E. Giacobino and A. Bramati. *Injection of orbital angular momentum and storage of quantized vortices in polariton superfluids.* Phys. Rev. Lett., **116**, 116402 (2016). doi:10.1103/PhysRevLett.116.116402.

[18] X. Ma, U. Peschel and O. A. Egorov. *Incoherent control of topological charges in nonequilibrium polariton condensates.* Phys. Rev. B, **93**, 035315 (2016). doi:10.1103/PhysRevB.93.035315.

[19] X. Ma, B. Berger, M. Aßmann, R. Driben, T. Meier, C. Schneider, S. Höfling and S. Schumacher. *Realization of all-optical vortex switching in exciton-polariton condensates.* Nature Communications, **11**, 1, 897 (2020). doi:10.1038/s41467-020-14702-5.

[20] B. Berger, D. Schmidt, X. Ma, S. Schumacher, C. Schneider, S. Höfling and M. Aßmann. *Formation dynamics of exciton-polariton vortices created by nonresonant annular pumping.* Phys. Rev. B, **101**, 245309 (2020). doi:10.1103/PhysRevB.101.245309.

[21] G. C. G. Berkhout, M. P. J. Lavery, J. Courtial, M. W. Beijersbergen and M. J. Padgett. *Efficient sorting of orbital angular momentum states of light.* Phys. Rev. Lett., **105**, 153601 (2010). doi:10.1103/PhysRevLett.105.153601.

[22] M. Ueta, H. Kanzaki, K. Kobayashi, Y. Toyozawa and E. Hanamura. *Excitonic Processes in Solids.* Springer-Verlag, Berlin (1984).

[23] A. V. Kavokin, J. J. Baumberg, G. Malpuech and F. P. Laussy. *Microcavities.* Oxford Science Publications (2007).

[24] M. Grundmann. *The Physics of Semiconductors.* Springer (2016).

[25] G. H. Wannier. *The structure of electronic excitation levels in insulating crystals.* Phys. Rev., **52**, 191 (1937). doi:10.1103/PhysRev.52.191.

[26] C. J. Hwang. *Lifetimes of free and bound excitons in high-purity GaAs.* Phys. Rev. B, **8**, 646 (1973). doi:10.1103/PhysRevB.8.646.

[27] *The NIST Reference on Constants, Units, and Uncertainty,* `https://physics.nist.gov/cgi-bin/cuu/Value?rydhcev`, *accessed on 31.01.2021.*

[28] W. Nolting. *Grundkurs Theoretische Physik 6.* Springer-Lehrbuch (2014).

[29] *The NIST Reference on Constants, Units, and Uncertainty,* `http://physics.nist.gov/cgi-bin/cuu/Value?kev`, *accessed on 31.01.2021.*

[30] *The NIST Reference on Constants, Units, and Uncertainty,* `https://physics.nist.gov/cgi-bin/cuu/Value?eqbohrrada0`, *accessed on 31.01.2021.*

[31] *Ioffe Institute, Semiconductor Materials Database,* `http://www.ioffe.ru/SVA/NSM/Semicond/GaAs/basic.html`, *accessed on 31.01.2021.*

[32] B. Nelsen, G. Liu, M. Steger, D. W. Snoke, R. Balili, K. West and L. Pfeiffer. *Dissipationless flow and sharp threshold of a polariton condensate with long lifetime.* Phys. Rev. X, **3**, 041015 (2013). doi:10.1103/PhysRevX.3.041015.

[33] G. Panzarini, L. C. Andreani, A. Armitage, D. Baxter, M. S. Skolnick, V. N. Astratov, J. S. Roberts, A. V. Kavokin, M. R. Vladimirova and M. A. Kaliteevski. *Exciton-light coupling in single and coupled semiconductor microcavities: Polariton dispersion and polarization splitting.* Phys. Rev. B, **59**, 5082 (1999). doi:10.1103/PhysRevB.59.5082.

[34] C. Weisbuch, M. Nishioka, A. Ishikawa and Y. Arakawa. *Observation of the coupled exciton-photon mode splitting in a semiconductor quantum microcavity.* Phys. Rev. Lett., **69**, 3314 (1992). doi:10.1103/PhysRevLett.69.3314.

[35] T. Fließbach. *Statistische Physik: Lehrbuch zur theoretischen Physik IV.* Spektrum Akad. Verl. (2010).

[36] K. B. Davis, M. O. Mewes, M. R. Andrews, N. J. van Druten, D. S. Durfee, D. M. Kurn and W. Ketterle. *Bose-einstein condensation in a gas of sodium atoms.* Phys. Rev. Lett., **75**, 3969 (1995). doi:10.1103/PhysRevLett.75.3969.

[37] M. Skolnick, R. Stevenson, A. Tartakovskii, R. Butté, M. Emam-Ismail, D. Whittaker, P. Savvidis, J. Baumberg, A. Lemaître, V. Astratov and J. Roberts. *Polariton–polariton interactions and stimulated scattering in semiconductor microcavities.* Materials Science and Engineering: C, **19**, 1–2, 407 (2002). doi:10.1016/S0928-4931(01)00433-7.

[38] T. C. Damen, J. Shah, D. Y. Oberli, D. S. Chemla, J. E. Cunningham and J. M. Kuo. *Dynamics of exciton formation and relaxation in GaAs quantum wells.* Phys. Rev. B, **42**, 7434 (1990). doi:10.1103/PhysRevB.42.7434.

[39] M. Gulia, F. Rossi, E. Molinari, P. E. Selbmann and P. Lugli. *Phonon-assisted exciton formation and relaxation in GaAs/*$\mathrm{Al_xGa_{1-x}}$*As quantum wells.* Phys. Rev. B, **55**, R16049 (1997). doi:10.1103/PhysRevB.55.R16049.

[40] P. G. Savvidis, J. J. Baumberg, R. M. Stevenson, M. S. Skolnick, D. M. Whittaker and J. S. Roberts. *Angle-resonant stimulated polariton amplifier.* Phys. Rev. Lett., **84**, 1547 (2000). doi:10.1103/PhysRevLett.84.1547.

[41] L. Pitaevskii and S. Stringari. *Bose-Einstein Condensation.* Oxford Science Publications (2003).

[42] J. Schmutzler, P. Lewandowski, M. Aßmann, D. Niemietz, S. Schumacher, M. Kamp, C. Schneider, S. Höfling and M. Bayer. *All-optical flow control of a polariton condensate using nonresonant excitation.* Phys. Rev. B, **91**, 195308 (2015). doi:10.1103/PhysRevB.91.195308.

[43] M. Vladimirova, S. Cronenberger, D. Scalbert, K. V. Kavokin, A. Miard, A. Lemaître, J. Bloch, D. Solnyshkov, G. Malpuech and A. V. Kavokin. *Polariton-polariton interaction constants in microcavities.* Phys. Rev. B, **82**, 075301 (2010). doi:10.1103/PhysRevB.82.075301.

[44] M. Richard, J. Kasprzak, R. Romestain, R. André and L. S. Dang. *Spontaneous coherent phase transition of polaritons in CdTe microcavities.* Phys. Rev. Lett., **94**, 187401 (2005). doi:10.1103/PhysRevLett.94.187401.

[45] M. Wouters, I. Carusotto and C. Ciuti. *Spatial and spectral shape of inhomogeneous nonequilibrium exciton-polariton condensates.* Phys. Rev. B, **77**, 115340 (2008). doi:10.1103/PhysRevB.77.115340.

[46] A. Askitopoulos, H. Ohadi, A. V. Kavokin, Z. Hatzopoulos, P. G. Savvidis and P. G. Lagoudakis. *Polariton condensation in an optically induced two-dimensional potential.* Phys. Rev. B, **88**, 041308 (2013). doi:10.1103/PhysRevB.88.041308.

[47] R. W. Gerchberg and W. O. Saxton. *A practical algorithm for the determination of the phase from image and diffraction plane pictures.* Optik, **35**, 237–246 (1972).

[48] F. Manni, K. G. Lagoudakis, T. C. H. Liew, R. André and B. Deveaud-Plédran. *Spontaneous pattern formation in a polariton condensate.* Phys. Rev. Lett., **107**, 106401 (2011). doi:10.1103/PhysRevLett.107.106401.

[49] H. E. Hall and W. F. Vinen. *The rotation of liquid helium II II. The theory of mutual friction in uniformly rotating helium II.* Proc. R. Soc. Lond., **A**, 238, 215–234 (1956). doi:10.1098/rspa.1956.0215.

[50] M. Andrews, David L. & Babiker. *The Angular Momentum of Light.* Cambridge: Cambridge University Press (2012).

[51] L. Dominici, R. Carretero-González, A. Gianfrate, J. Cuevas-Maraver, A. S. Rodrigues, D. J. Frantzeskakis, G. Lerario, D. Ballarini, M. De Giorgi, G. Gigli, P. G. Kevrekidis and D. Sanvitto. *Interactions and scattering of quantum vortices in a polariton fluid.* Nature Communications, **9**, 1, 1467 (2018). doi:10.1038/s41467-018-03736-5.

[52] G. Nardin, T. K. Paraïso, R. Cerna, B. Pietka, Y. Léger, O. El Daif, F. Morier-Genoud and B. Deveaud-Plédran. *Probability density optical tomography of confined quasiparticles in a semiconductor microcavity.* Applied Physics Letters, **94**, 18, 181103 (2009). doi:10.1063/1.3126022.

[53] D. Sanvitto, A. Amo, L. Viña, R. André, D. Solnyshkov and G. Malpuech. *Exciton-polariton condensation in a natural two-dimensional trap.* Phys. Rev. B, **80**, 045301 (2009). doi:10.1103/PhysRevB.80.045301.

[54] P. Cristofolini, A. Dreismann, G. Christmann, G. Franchetti, N. G. Berloff, P. Tsotsis, Z. Hatzopoulos, P. G. Savvidis and J. J. Baumberg. *Optical superfluid phase transitions and trapping of polariton condensates.* Phys. Rev. Lett., **110**, 186403 (2013). doi:10.1103/PhysRevLett.110.186403.

[55] T. C. H. Liew, O. A. Egorov, M. Matuszewski, O. Kyriienko, X. Ma and E. A. Ostrovskaya. *Instability-induced formation and nonequilibrium dynamics of phase defects in polariton condensates.* Phys. Rev. B, **91**, 085413 (2015). doi:10.1103/PhysRevB.91.085413.

[56] K. W. Madison, F. Chevy, W. Wohlleben and J. Dalibard. *Vortex formation in a stirred bose-einstein condensate.* Phys. Rev. Lett., **84**, 806 (2000). doi:10.1103/PhysRevLett.84.806.

[57] J. Jackson. *Classical Electrodynamcis.* Wiley. New York (1962).

[58] J. H. Poynting. *On the transfer of energy in the electromagnetic field.* Phil. Trans. Roy. Soc. (London), **175**, 343–363 (1884).

[59] J. H. Poynting. *The wave motion of a revolving shaft, and a suggestion as to the angular momentum in a beam of circularly polarised light.* Proc. R. Soc. Lond., **A**, 82, 560–567 (1909). doi:10.1098/rspa.1909.0060.

[60] R. A. Beth. *Mechanical detection and measurement of the angular momentum of light.* Phys. Rev., **50**, 115 (1936). doi:10.1103/PhysRev.50.115.

[61] L. Allen, M. W. Beijersbergen, R. J. C. Spreeuw and J. P. Woerdman. *Orbital angular momentum of light and the transformation of laguerre-gaussian laser modes.* Phys. Rev. A, **45**, 8185 (1992). doi:10.1103/PhysRevA.45.8185.

[62] M. V. Berry. *Paraxial beams of spinning light.* In M. S. Soskin (editor), *International Conference on Singular Optics*, volume 3487, pp. 6 – 11. International Society for Optics and Photonics, SPIE (1998). doi:10.1117/12.317704.

[63] A. T. O'Neil, I. MacVicar, L. Allen and M. J. Padgett. *Intrinsic and extrinsic nature of the orbital angular momentum of a light beam.* Phys. Rev. Lett., **88**, 053601 (2002). doi:10.1103/PhysRevLett.88.053601.

[64] J. Leach, E. Yao and M. J. Padgett. *Observation of the vortex structure of a non-integer vortex beam.* New Journal of Physics, **6**, 71 (2004). doi:10.1088/1367-2630/6/1/071.

[65] J. B. Götte, S. Franke-Arnold, R. Zambrini and S. M. Barnett. *Quantum formulation of fractional orbital angular momentum.* Journal of Modern Optics, **54**, 12, 1723 (2007). doi:10.1080/09500340601156827.

[66] S. N. Alperin, R. D. Niederriter, J. T. Gopinath and M. E. Siemens. *Quantitative measurement of the orbital angular momentum of light with a single, stationary lens.* Opt. Lett., **41**, 21, 5019 (2016). doi:10.1364/OL.41.005019.

[67] S. N. Alperin and M. E. Siemens. *Angular momentum of topologically structured darkness.* Phys. Rev. Lett., **119**, 203902 (2017). doi:10.1103/PhysRevLett.119.203902.

[68] V. Bazhenov, M. Soskin and M. Vasnetsov. *Screw dislocations in light wavefronts.* Journal of Modern Optics, **39**, 5, 985 (1992). doi:10.1080/09500349214551011.

[69] M. Beijersbergen, L. Allen, H. van der Veen and J. Woerdman. *Astigmatic laser mode converters and transfer of orbital angular momentum.* Optics Communications, **96**, 1, 123 (1993). doi:10.1016/0030-4018(93)90535-D.

[70] G. Gibson, J. Courtial, M. J. Padgett, M. Vasnetsov, V. Pas'ko, S. M. Barnett and S. Franke-Arnold. *Free-space information transfer using light beams carrying orbital angular momentum.* Opt. Express, **12**, 22, 5448 (2004). doi:10.1364/OPEX.12.005448.

[71] A. Mair, A. Vaziri, G. Weihs and A. Zeilinger. *Entanglement of the orbital angular momentum states of photons.* Nature, **412**, 6844, 313 (2001). doi:10.1038/35085529.

[72] J. Leach, M. J. Padgett, S. M. Barnett, S. Franke-Arnold and J. Courtial. *Measuring the orbital angular momentum of a single photon.* Phys. Rev. Lett., **88**, 257901 (2002). doi:10.1103/PhysRevLett.88.257901.

[73] M. V. Klein and T. E. Furtak. *Optik.* Springer (1988).

[74] M. N. O'Sullivan, M. Mirhosseini, M. Malik and R. W. Boyd. *Near-perfect sorting of orbital angular momentum and angular position states of light.* Opt. Express, **20**, 22, 24444 (2012). doi:10.1364/OE.20.024444.

[75] C. Wan, J. Chen and Q. Zhan. *Compact and high-resolution optical orbital angular momentum sorter.* APL Photonics, **2**, 3, 031302 (2017). doi:10.1063/1.4974824.

[76] *Holoeye SLM product description,* `http://holoeye.com/wp-content/uploads/Spatial_Light_Modulators.pdf`, *accessed on 31.01.2021.*

[77] M. Wouters and I. Carusotto. *Excitations in a nonequilibrium bose-einstein condensate of exciton polaritons.* Phys. Rev. Lett., **99**, 14, 140402 (2007). doi:10.1103/PhysRevLett.99.140402.

[78] V. G. Sala, D. D. Solnyshkov, I. Carusotto, T. Jacqmin, A. Lemaître, H. Terças, A. Nalitov, M. Abbarchi, E. Galopin, I. Sagnes, J. Bloch, G. Malpuech and A. Amo. *Spin-orbit coupling for photons and polaritons in microstructures.* Phys. Rev. X, **5**, 011034 (2015). doi:10.1103/PhysRevX.5.011034.

[79] D. A. Zezyulin, Y. V. Kartashov, D. V. Skryabin and I. A. Shelykh. *Spin–orbit coupled polariton condensates in a radially periodic potential: Multiring vortices and rotating solitons.* ACS Photonics, **5**, 9, 3634 (2018). doi:10.1021/acsphotonics.8b00536.

[80] Y. Wen, I. Chremmos, Y. Chen, J. Zhu, Y. Zhang and S. Yu. *Spiral transformation for high-resolution and efficient sorting of optical vortex modes.* Phys. Rev. Lett., **120**, 193904 (2018). doi:10.1103/PhysRevLett.120.193904.

[81] X. Ma and S. Schumacher. *Vortex multistability and bessel vortices in polariton condensates.* Phys. Rev. Lett., **121**, 227404 (2018). doi:10.1103/PhysRevLett.121.227404.

[82] M. Pukrop, S. Schumacher and X. Ma. *Circular polarization reversal of half-vortex cores in polariton condensates.* Phys. Rev. B, **101**, 205301 (2020). doi:10.1103/PhysRevB.101.205301.

[83] X. Ma and S. Schumacher. *Vortex-vortex control in exciton-polariton condensates.* Phys. Rev. B, **95**, 235301 (2017). doi:10.1103/PhysRevB.95.235301.

[84] X. Ma, Y. V. Kartashov, T. Gao, L. Torner and S. Schumacher. *Spiraling vortices in exciton-polariton condensates.* Phys. Rev. B, **102**, 045309 (2020). doi:10.1103/PhysRevB.102.045309.

[85] Y. Wen, I. Chremmos, Y. Chen, Y. Zhang and S. Yu. *Arbitrary multiplication and division of the orbital angular momentum of light.* Phys. Rev. Lett., **124**, 213901 (2020). doi:10.1103/PhysRevLett.124.213901.

Acknowledgments

My thanks go to all the people who made this work possible and supported me in any way during the research, lab work, and writing process of this thesis.

My special thanks goes to Jun.-Prof. Dr. Marc Aßmann for making this great research project about exciton polariton vortices possible in first place and for the subsequent superb supervision with great engagement for all people under his supervision.

I also thank our collaborators Dr. Xuekai Ma and Prof. Dr. Stefan Schumacher from the University of Paderborn for proposing interesting experiments with polariton vortices and performing the theory simulations to model the exciton polariton dynamics.

Furthermore, I would like to thank my former colleagues Daniel Schmidt and Johannes Thewes for great discussions, general help in the lab and providing an awesome and supportive work environment. My thanks also go to my former master student Marius Kahlert for his help in setting up and developing the experimental setup for OAM measurements.

Finally, I would like to thank all E2-members for the great atmosphere at our chair.